National Library of Canada
Bibliothèque nationale du Canada

Canadian Theses Service
Service des thèses canadiennes

Ottawa, Canada
K1A 0N4

NOTICE

The quality of this microform is heavily dependent upon the quality of the original thesis submitted for microfilming. Every effort has been made to ensure the highest quality of reproduction possible.

If pages are missing, contact the university which granted the degree.

Some pages may have indistinct print especially if the original pages were typed with a poor typewriter ribbon or if the university sent us an inferior photocopy.

Reproduction in full or in part of this microform is governed by the Canadian Copyright Act, R.S.C. 1970, c. C-30, and subsequent amendments.

AVIS

La qualité de cette microforme dépend grandement de la qualité de la thèse soumise au microfilmage. Nous avons tout fait pour assurer une qualité supérieure de reproduction.

S'il manque des pages, veuillez communiquer avec l'université qui a conféré le grade.

La qualité d'impression de certaines pages peut laisser à désirer, surtout si les pages originales ont été dactylographiées à l'aide d'un ruban usé ou si l'université nous a fait parvenir une photocopie de qualité inférieure.

La reproduction, même partielle, de cette microforme est soumise à la Loi canadienne sur le droit d'auteur, SRC 1970, c. C-30, et ses amendements subséquents.

NL-339 (r. 88/04) c

Canada

UNIVERSITY OF ALBERTA

THE EFFECTS OF RADIATION ON NORMAL HUMAN BRAIN AS ASSESSED BY NUCLEAR MAGNETIC RESONANCE

BY

SUSAN KARIN ALBO

A THESIS

SUBMITTED TO THE FACULTY OF GRADUATE STUDIES AND RESEARCH

IN PARTIAL FULFILLMENT OF THE REQUIREMENTS FOR

THE DEGREE OF MASTER OF SCIENCE

DEPARTMENT OF APPLIED SCIENCES IN MEDICINE

EDMONTON, ALBERTA

FALL 1990

National Library of Canada
Bibliothèque nationale du Canada

Canadian Theses Service
Service des thèses canadiennes

Ottawa, Canada
K1A 0N4

The author has granted an irrevocable non-exclusive licence allowing the National Library of Canada to reproduce, loan, distribute or sell copies of his/her thesis by any means and in any form or format, making this thesis available to interested persons.

The author retains ownership of the copyright in his/her thesis. Neither the thesis nor substantial extracts from it may be printed or otherwise reproduced without his/her permission.

L'auteur a accordé une licence irrévocable et non exclusive permettant à la Bibliothèque nationale du Canada de reproduire, prêter, distribuer ou vendre des copies de sa thèse de quelque manière et sous quelque forme que ce soit pour mettre des exemplaires de cette thèse à la disposition des personnes intéressées.

L'auteur conserve la propriété du droit d'auteur qui protège sa thèse. Ni la thèse ni des extraits substantiels de celle-ci ne doivent être imprimés ou autrement reproduits sans son autorisation.

ISBN 0-315-65076-1

UNIVERSITY OF ALBERTA

RELEASE FORM

NAME OF AUTHOR	SUSAN KARIN ALBO
TITLE OF THESIS	THE EFFECTS OF RADIATION ON NORMAL HUMAN BRAIN AS ASSESSED BY NUCLEAR MAGNETIC RESONANCE
DEGREE FOR WHICH THESIS WAS PRESENTED	MASTER OF SCIENCE
YEAR THIS DEGREE GRANTED	FALL 1990

Permission is hereby granted to the UNIVERSITY OF ALBERTA LIBRARY to reproduce single copies of this thesis and to lend or sell such copies of this thesis for private, scholarly or scientific research purposes only.

The author reserves other publication rights, and neither the thesis nor extensive extracts from it may be printed or otherwise reproduced without the author's written permission.

(Signed).....

PERMANENT ADDRESS:

340 Toledo St.
Thunder Bay, Ontario
P7A 2R6

Date:

One of the great tragedies in life . . .

is the murder
of a beautiful theory

by a gang
of brutal facts

B. Franklin

THE UNIVERSITY OF ALBERTA

FACULTY OF GRADUATE STUDIES AND RESEARCH

The undersigned certify that they have read, and recommend to the Faculty of Graduate Studies and Research for acceptance, a thesis entitled THE EFFECTS OF RADIATION ON NORMAL HUMAN BRAIN AS ASSESSED BY NUCLEAR MAGNETIC RESONANCE submitted by SUSAN KARIN ALBO in partial fulfillment of the requirements for the degree of MASTERS OF SCIENCE.

P S Allen

Dr. PS Allen (Co-supervisor)

R C Urtasun

Dr. RC Urtasun (Co-supervisor)

Brian D Sykes

Dr. BD Sykes

D J Griffiths

Dr. DJ Griffiths

Date: Sept 26/90

This thesis is dedicated

to all those patients who contributed

so much of their time to this study

Abstract

The initial purpose of this study was to determine if nuclear magnetic resonance (NMR) spectroscopy could be used to detect radiation induced changes in high energy phosphate metabolites found in human brain, and if these spectroscopic changes could be correlated with changes observed in NMR images of brain. The methodology involved acquisition of phosphorus (^{31}P) spectra and transverse relaxation (T_2) images from the central nervous system of patients undergoing radiotherapy (RT) for the treatment of brain tumors. A second group of brain tumor patients was analyzed utilizing proton (^{1}H) spectroscopy, in attempts to observe changes in the levels of brain metabolites, other than those visible by phosphorus NMR. This second group of patients was not imaged. In both cases, spectra were acquired from "normal" tissue in two regions of the brain, one region that received high doses of radiation, and another that was exposed to lower doses. Patients were analyzed prior to their radiation treatment, then scheduled for further analysis at intervals of 0,2,4,8 and 12 months following completion of RT.

The spectroscopy results are, as of yet, preliminary, and only tentative conclusions can be drawn. Phosphorus spectroscopy at its present level of sensitivity, seems to suggest that any radiation induced damage that may occur, does not alter the relative concentrations of phosphorus metabolites beyond the limits of normal variation. The ratios of ^{31}P metabolite peak areas display a variation of approximately $\pm$ 25 % in brains of healthy volunteers, the variability originating not only from biological variation, but also from measurement uncertainty and poor processing reproducibility. Therefore, in order to detect radiation damage, the metabolite concentration must increase or decrease by over 25%. Proton

spectroscopy, on the other hand, detects changes in the level of certain NMR visible metabolites, namely those with choline groups, following RT. Choline / creatine peak area ratios increase, and N-acetyl aspartate / choline peak area ratios decrease, in the brains of patients following RT, particularly in patients who are not receiving the anti-inflammatory drug, Decadron. Proton metabolite ratios also display large normal variations (± 20 %), but the radiation induced changes detected by ^1H spectroscopy exceed these limits.

The NMR imaging results confirm those of previous studies, namely, that regions of increased transverse relaxation times are observed in brain following RT. These increases in T_2 commonly occur in the peritumoral lesion, a post operative area of edema and necrosis that surrounds the original site of the tumor. We cannot correlate radiation effects in images with those in spectroscopy, due to the lack of observable changes in the case of the phosphorus spectroscopy, and in the lack of T_2 calculated images from patients entered into the proton spectroscopy study.

Further studies, particularly in the case of proton spectroscopy, are necessary for a more complete understanding of the damage imparted to normal brain by therapeutic radiation. A long term (2 years or more) follow up of patients undergoing radiotherapy, is required to quantify any damage, acute or delayed, that may occur. These studies, ideally, should be complimented by autopsies, or work with animal models.

ACKNOWLEDGEMENTS

I wish to thank Dr. Peter Allen for allowing me the opportunity to undertake this research project.

For his unending support and guidance, I am deeply indebted to Dr. Raul Urtasun. He instilled confidence and perseverance when the research was getting frustrating, and always had a word of praise when things finally worked. Many thanks also to Dr. Olu Agboola, Mrs. Debbie Huyser-Wieringa, Ms. Sandy McKinnon and Mrs. Janet Partington for their assistance with the patients.

The members of the University of Alberta *in vivo* NMR Group have all lent support over the past two years. I am especially grateful to the following:

-Mr. Dan Georghiu, for his assistance with the NMR, for continually upgrading the spectroscopy software, and for his patience with me!

-Dr. Chris Hanstock and Dr. Chunpen Thomas, who were always there with helpful suggestions and advice.

-Mrs. Ivy Ho, for developing the computer programs used for data analysis.

-Mr. Dave Ellinger, who helped with technical problems and kept the NMR machine running as smoothly as possible.

Above all, I would like to extend my most sincere gratitude to the cancer patients who volunteered their time to aid in this study. Thanks also to all the "normal" volunteers from whom the control data was acquired.

Financial support was provided by a studentship from the Alberta Heritage Foundation for Medical Research.

TABLE OF CONTENTS

Chapter			Page
1	GENERAL INTRODUCTION		14-64
	1.1	Introduction to the Thesis	14
	1.2	Introduction to Nuclear Magnetic Resonance	16
		1.2.1 The NMR Principle	17
		1.2.2 Classical Description of NMR	20
		1.2.3 Relaxation	23
		1.2.4 NMR Spectroscopy	25
		1.2.5 Localization	28
		1.2.6 Slice Selection	29
		1.2.7 Imaging	31
	1.3	Introduction to the Central Nervous System	34
		1.3.1 Normal Brain Physiology	34
		1.3.2 Physiology of Human Tumors	37
		1.3.3 Energy Metabolism in Brain	40
		1.3.4 Phosphorus Metabolism in Brain	42
	1.4	Introduction to Radiology	45
		1.4.1 X-radiation	45
		1.4.2 Radiobiology	47
		1.4.3 The Effects of Radiation on the CNS	50
		1.4.4 Radiotherapy of the CNS	52
	1.5	Introduction to NMR Spectroscopy of Brain	55
		1.5.1 Cerebral Phosphorus Spectroscopy	55
		1.5.2 Cerebral Proton Spectroscopy	60

Chapter			Page
2	METHODS		65-88
	2.1	Human Subjects	65
		2.1.1 Patient Selection	66
		2.1.2 Healthy Volunteers	67
	2.2	NMR Imaging	67
		2.2.1 Data Acquisition	67
		2.2.2 Image Analysis	70
	2.3	NMR Spectroscopy	73
		2.3.1 Phosphorus Spectroscopy	74
		2.3.2 Proton Spectroscopy	78
		2.3.3 Spectral Analysis	83
3	RESULTS AND DISCUSSION		89-131
	3.1	Phosphorus Spectroscopy	89
		3.1.1 General Considerations	90
		3.1.2 Data from Patients	96
		3.1.3 Data from Long Term Survivors	103
	3.2	NMR Imaging	106
		3.2.1 Variability of Transverse Relaxation Time Measurements in Brain	106
		3.2.2 Data from Patients	110
	3.3	Proton Spectroscopy	118
		3.3.1 General Considerations	118
		3.3.2 Data from Patients	123
4	CONCLUSIONS		132-136

Page

REFERENCES 137-150

APPENDIX I 151
APPENDIX II 152
APPENDIX III 153
APPENDIX 1V 154
APPENDIX V 158

LIST OF TABLES

Table		Page
1.00	Phosphomonoesters Found in Brain	43
1.01	Phosphorus NMR Resonances of Brain Spectra	55
1.02	Proton NMR Resonances of Brain Spectra	61
2.00	Age and Sex Distribution of Patients in the NMR Study	67
2.01	Relative Peak Areas of Phosphorus Metabolites at Various Repetition Times	78
3.00	Normal Variations in Brain Metabolite Concentrations	92
3.01	Processing Reproducibility in the Calculation of ^{31}P Metabolite Peak Area Ratios and pH	94
3.02	Metabolite/MDA Peak Area Ratios as Established from ^{31}P Spectra of Healthy Brains	95
3.03	Number of Patients Analyzed with ^{31}P Spectroscopy	96
3.04	Phosphorus Spectroscopy Data from Long Term Survivors	104
3.05	Slice Thickness Dependance of Transverse Relaxation Times of Cerebral Grey and White Matter	107
3.06	Area of the Peritumoral Lesion Calculated from NMR Images of Patient Brain	111
3.07	Comparison of Transverse Relaxation Times Between the Ipsilateral and Contralateral Cerebral Hemispheres	113
3.08	Comparison of Transverse Relaxation Times of Brain Tissue Within and Outside of the Peritumoral Lesion	116
3.09	Mean ^{1}H Metabolite Ratios from Brains of Healthy Volunteers	121
3.10	Estimates of Brain Metabolite Concentrations in Healthy Brain Determined by NMR	123
3.11	Metabolite/Water Peak Area Ratios from ^{1}H Spectra of the CNS of Patients	125

LIST OF FIGURES

Figure		Page
1.00	The Effect of a Static Magnetic Field on Nuclear Dipoles	18
1.01	Vector Representation of the Nuclear Magnetic Moments	20
1.02	Magnetization during Resonant RF Excitation	21
1.03	The Magnetization Vector Following RF Excitation	22
1.04	Spin Coupling	26
1.05	The B_1 Profile of a Surface Coil	28
1.06	Spatial Encoding	30
1.07	The Inversion Recovery Pulse Sequence	32
1.08	The Spin Echo Pulse Sequence	33
1.09	Representation of a Myelinated Neuron	35
1.10	Role of the Myelin Sheath in Transmission of Nerve Impulses	37
1.11	The Energy Metabolism Pathway	41
1.12	A Typical *in vivo* Phosphorus NMR Spectrum of Human Brain at 1.5 Tesla	56
1.13	A Typical *in vivo* Proton Spectrum of Human Brain at 1.5 Tesla	62
2.00	Isodose Distributions: A Map of the Relative Radiation Doses Imparted to Various Regions of the CNS of Patients	70
2.01	Determination of Transverse Relaxation Times in Brain from T_2 Calculated Images	71
2.02	Method Used in the Determination of the Area of the Peritumoral Lesion	72
2.03	Depth Pulse Sequence Used to Acquire ^{31}P Spectra	74

Figure		Page
2.04	The Experimental Apparatus Used to Acquire ^{31}P Spectra	76
2.05	Proton Density Depth Profile of a Human Head	77
2.06	The STEAM Pulse Sequence	80
2.07	An Example of Fourier Transformed Time Domain Data from the ^{31}P Free Induction Decay Signal	83
2.08	An Example of a Well Phased Phosphorus Spectrum	84
2.09	An Example of a Fully Processed ^{31}P Spectrum	85
2.10	An Example of Fourier Transformed Time Domain Data from the ^{1}H Free Induction Decay Signal	85
2.11	An Example of Well Phased Metabolite Peaks from a Proton Spectrum	86
2.12	An Example of a Fully Processed Proton Spectrum	87
3.00	An Example of a "Fitted" ^{31}P Spectrum of Healthy Human Brain	90
3.01	Temporal Variations in the pH of the CNS in Brain Tumor Patients	97
3.02	Temporal Variations in ^{31}P Metabolite Peak Area Ratios in the CNS of Brain Tumor Patients	99
3.03	^{31}P Metabolite Peak Area Ratios from Irradiated Brain of Long Term Survivors Compared to Similar Ratios from Healthy Brain	105
3.04	Temporal Changes in the Size of Peritumoral Lesion in Patient #4	112
3.05	Temporal Alterations in Transverse Relaxation Between the Two Cerebral Hemispheres	114
3.06	An Example of a "Fitted" ^{1}H Spectrum of Healthy Human Brain	118
3.07	Examples of ^{1}H Spectra of Brain Prior to and Following Cranial Irradiation	124
3.08	Peak Area Ratios from ^{1}H Spectra of the CNS of Patients	126
3.09	The Effect of Decadron on ^{1}H Metabolite Ratios from Irradiated Brain	130

CHAPTER 1: GENERAL INTRODUCTION

1.1 Introduction to the Thesis

This thesis embarks on a prospective clinical investigation intent upon biochemically quantifying the damage to normal brain tissue induced by therapeutic cranial radiation. Although clinical symptoms may eventually manifest themselves, autopsy studies have revealed the existence of radiation-induced cellular damage in the CNS, in the absence of any external symptoms (16). Our goal is to establish a non-invasive procedure which can detect and quantify radiation induced damage at the biochemical level, prior to the onset of clinical symptoms. Such a procedure might allow a more accurate calculation of the therapeutic ratio (benefit vs. harm) of radiation treatments being utilized, and possibly give an early indicator of CNS radiation effects.

Patients with high grade gliomas were chosen as candidates for this study, due to the high doses of cranial radiation that they would receive for the treatment of their brain tumors. The long term survival and follow up of numerous individuals undergoing radiotherapy, is imperative for a comprehensive study. Unforeseen to us was, in fact, the poor survival and slow accrual of patients, which led to a much slower accumulation of data than was originally expected. A comprehensive investigation, therefore, is beyond the scope of this thesis; it would require years of accumulation of clinical data. Nonetheless, this study provides a solid basis from which other investigations can be founded.

Nuclear magnetic resonance (NMR) was chosen as the non invasive technique by means of which we might reach our goal. NMR images have, in previous studies, visualized edema, demyelination or necrosis occurring secondary to irradiation of the CNS (43,96,25,85,111,26). These studies have shown that radiation damage might not be observed until several months following the irradiation of brain. Histological studies, which require invasive procedures such as biopsies or autopsies, reveal the cellular nature of the radiation-induced damage (16,110,112). NMR spectroscopy, however, allows biochemical analysis of relative metabolite concentrations *in vivo*. Both ^{31}P and ^{1}H NMR spectroscopy have the potential to observe radiation induced changes in metabolite levels in brain. Whether or not this is achievable in the clinical situation would depend upon the extent of damage which is imparted to brain during therapeutic radiation, and upon the sensitivity of NMR spectroscopy to detect radiation induced changes.

Initially, ^{31}P spectroscopy data were collected from patients, in order to monitor the relative levels of high energy phosphate metabolites, namely, phosphocreatine (PCr), inorganic phosphate (Pi), and adenosine triphosphate (ATP). The same brains were imaged, using an NMR pulse sequence that allowed calculation of transverse relaxation times directly from the images, for comparison with the phosphorus spectroscopy results. During the time that we were collecting our data, a paper was published by Grossman *et al* (43), which suggested that there were no observable changes in the relative levels of ^{31}P detectable brain metabolites following irradiation to the CNS. Although our images reflected some changes following radiotherapy, our ^{31}P results agreed with those of Grossman. We then attempted to detect radiation induced damage to brain from a different angle. A comprehensive literature search revealed that changes in some of the lipids and amino

acids that are found in brain, may occur following irradiation of the CNS. We therefore decided to utilize proton spectroscopy, in the hope of detecting one or more of these changes.

Our methodology is detailed in Chapter 2 of this thesis. Since the study was approached from three different angles, namely, NMR imaging, ^{31}P spectroscopy and ^{1}H spectroscopy, the methodology for each was considered separately. Similarly, the results (Chapter 3) are analyzed separately for each of the three analytical techniques. Raw data for the imaging results are included in section 3.2, while raw data for the spectroscopy results can be found in the appendices found at the end of the thesis. The correlation of ^{31}P spectroscopic findings with imaging and ^{1}H spectroscopic results is achieved in the conclusions (Chapter 4). In the last chapter we also developed a hypothesis, based on our findings, to rationalize physiological events that may be occurring in brain following therapeutic irradiation.

Some of the results, particularly those of the ^{1}H spectroscopy study, are very preliminary, often based upon a single data point. Further data collection from irradiated brain must be undertaken, before more concrete conclusions can be reached.

1.2 Introduction to Nuclear Magnetic Resonance

In vivo NMR allows the non-invasive observation of soft tissues in living systems. While NMR imaging reveals anatomical insights, spectroscopy provides biochemical characterization of the tissues.

A full explanation of NMR requires a detailed quantum mechanical analysis. However, the main principles can be understood from classical analogues of the

quantum mechanical results. For the purposes of this introduction, a description of NMR in classical terms will suffice.

1.2.1 The NMR Principle

In certain atoms, the spinning of intra nuclear charges can generate magnetic dipole moments along the axis of that spin. The magnetic moments of the nuclei in which this occurs, allow those nuclei to interact with magnetic fields. Nuclear magnetic resonance is a spectroscopic technique which exploits these interactions in order, first, to excite the nuclear spin system and then, to detect the signals from the nuclear dipoles following excitation. The energy emitted by the nuclear dipoles is in the radiofrequency range of the electromagnetic spectrum, and the detected signal can be mathematically processed and displayed as a frequency spectrum.

Magnetic nuclei are characterized by their gyromagnetic ratio, γ, which is a proportionality constant that relates the spin angular momentum, $\mathbf{p}$, and magnetic moment, $\boldsymbol{\mu}$, of a nuclear dipole;

$$\gamma = \mathbf{p} / \boldsymbol{\mu} \qquad (1)$$

Both the net spin angular momentum and magnetic moment are a function of the spin quantum number, I. The components of $\boldsymbol{\mu}$ and $\mathbf{p}$ along the z axis are given by:

$$p_z = m \hbar \qquad (2)$$

$$\mu_z = \gamma m \hbar \qquad (3)$$

where $\hbar$ is the Planck constant divided by 2π and m can have the value I, I-1,...-I. For nuclei that exhibit a magnetic dipole moment, the spin quantum number is greater

than or equal to one half. However, only the case where $I = {}^1/_2$ will be discussed in this thesis.

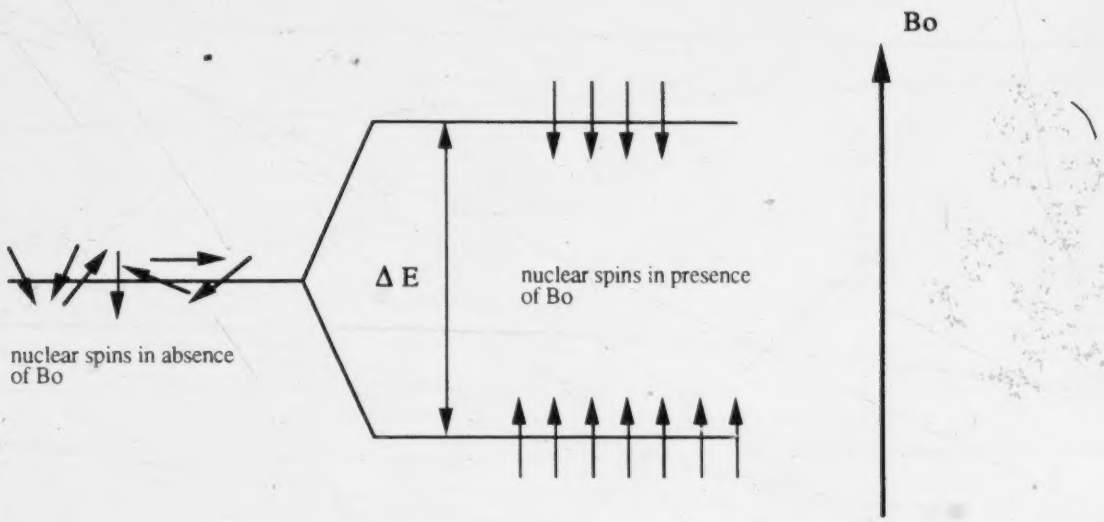

FIGURE 1.00:
THE EFFECT OF A STATIC MAGNETIC FIELD ON NUCLEAR DIPOLES

At thermal equilibrium and in the absence of any magnetic fields, the nuclear dipoles are randomly oriented in space. In the presence of a uniform static magnetic field (B_0) the dipoles will orient themselves with respect to the field, as illustrated in Figure 1.00. By convention, the direction of B_0 defines the z axis of a Cartesian coordinate system.

The nuclear spins orient themselves either parallel or antiparallel to the applied field. Each orientation can be described in terms of the energetic state, E, of the nuclei found in that orientation:

$$E = -\mu B_0 \cos\theta \qquad (4)$$

where θ is the angle between μ and static magnetic field, B_0. If we consider only the

z component of μ, when $\theta = 0$, and μ_z is defined as in Equation 3, then two distinct energy levels will form when a spin 1/2 system is exposed to a static magnetic field:

$$E_{lower} = - ({}^1/_2 \gamma \hbar) B_o \quad (5)$$

$$E_{higher} = - (- {}^1/_2 \gamma \hbar) B_o \quad (6)$$

Thus, the difference in energy, ΔE, between the two orientations is :

$$\Delta E = \gamma \hbar B_o \quad (7)$$

The population distribution of dipoles among these two nuclear magnetic energy states follows a Boltzman distribution. At thermal equilibrium in a static magnetic field, most dipoles adopt a lower energy (parallel) orientation, since the probability of occupying an energy level decreases with increasing energy.

In the NMR experiment, transitions between the two energy levels are induced by the application of a magnetic field, B_1, rotating in the xy plane. For maximum interaction between the B_1 field and the dipoles to occur, the field must rotate with a frequency, ν_o, given by:

$$\Delta E = h \nu_o \quad (8)$$

Combination of Equations 7 and 8 yields:

$$\gamma \hbar B_o = h \nu_o \quad (9)$$

Replacing $2 \pi \nu_o$ with the angular frequency term, ω_o:

$$\gamma B_o = \omega_o \quad (10)$$

This expression describes the resonance condition for an NMR experiment, which will allow the greatest number of transitions between high energy and low energy orientations of the nuclear dipoles

1.2.2 Classical Description of NMR

Any system of nuclear spins can be visualized as a set of vectors, each vector describing the magnetic moment of the individual nuclear dipoles. Summation of these vectors forms a resultant vector representative of the net magnetic moment of the ensemble of spins (Figure 1.01).

FIGURE 1.01: VECTOR REPRESENTATION OF THE NUCLEAR MAGNETIC MOMENTS

The net magnetic moment per unit volume can be expressed in terms of M, the magnetization vector. In the absence of a magnetic field, this net magnetization is zero. However, at thermal equilibrium and in the presence of a static magnetic field (B_0) the net magnetization, represented by the bold arrow, lies along the axis of the field.

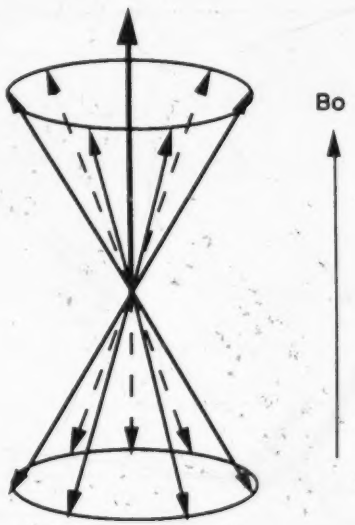

Application of a resonant oscillating magnetic field, B_1, perpendicular to the static field will perturb the net magnetization such that it rotates away from the z axis. The B_1 field is generated by passing an RF current through a coil to produce an oscillating magnetic field. This RF field, with frequency ω_0, causes a precession of

M about B_1, with an angular frequency $\omega_1 = \gamma B_1$ (35). In a time interval, t, the net magnetization rotates away from the z axis through an angle, θ, where:

$$\theta = \gamma B_1 t \qquad (11)$$

The time interval required to rotate the magnetization such that $\theta = 90^o$ is known as a 90 degree excitation pulse. Similarly, a 180 degree excitation pulse is dictated by the time at which the nuclear magnetization will have precessed through 180^o.

A convenient concept for describing this motion of the magnetization is that of the rotating frame of reference. The rotating frame refers to a coordinate system which rotates about B_o at the frequency of the B_1 field. By analogy with the laboratory frame, which has coordinates x, y and z, the coordinates of the rotating frame are labelled x', y', and z'. The z axes in the two frames of reference are identical, thus the x' and y' coordinates rotate about the z axis. Figure 1.02 describes the movement of the magnetization vector in the rotating frame, during application of a B_1 pulse.

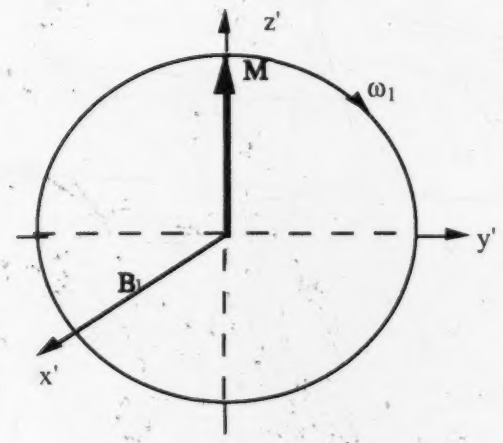

FIGURE 1.02: MAGNETIZATION DURING RESONANT RF EXCITATION

When the Larmor frequency of the nuclear dipoles equals the frequency of the rotating frame, the precession of nuclei about B_0 appears to be zero, and the position of B_1 appears stationary. Both B_0 and B_1 combine to produce a torque experienced by **M**, although in the rotating frame, only the latter appears to affect the magnetization vector. **M** will precess about B_1 in the z'y' plane at a frequency of ω_1.

Following application of the excitation pulse, the net magnetization will be at some angle, θ, from the z axis (Figure 1.03). A torque is experienced by the vector, and it precesses about the B_0 axis at an angular frequency, ω_0. This is known as the Larmor frequency and it is identical to the resonance frequency described in Section 1.2.1. The transverse component of this rotating magnetization will cause a time-dependant magnetic field to thread an RF coil and induce an electromotive force (EMF) within the coil. The same RF coil that is used to transmit the B_1 field can also be used to detect the resultant signal.

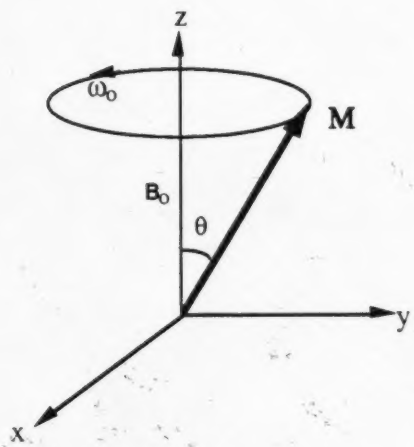

FIGURE 1.03:
THE MAGNETIZATION VECTOR FOLLOWING RF EXCITATION

The B_1 field is no longer present, but **M** remains at some angle, θ, from the z axis. The net magnetization experiences a torque, which causes it to precess about the static magnetic field, in the xy plane, at a frequency of ω_0.

The induced EMF is amplified and processed to produce the NMR signal. This signal is collected as a function of time but, due to relaxation processes which will be described in the next section, the signal decays. Free induction decay (FID) is the name given to this NMR signal in the time domain. In order to obtain the NMR spectrum in the frequency domain, mathematical conversion of the time domain data must be done. This can be achieved by employing a complex mathematical procedure

known as Fourier transformation, which interconverts spatial and temporal representations of the signal (35).

1.2.3 Relaxation

In general terms, relaxation is the process by which thermal equilibrium is reestablished to a system of nuclear spins following perturbation. The individual nuclei interact with each other and the environment causing two distinct processes, longitudinal and transverse relaxation, to occur. Longitudinal relaxation describes the recovery of the z component of magnetization. This recovery is often exponential in time, and is characterized by the time constant, T_1, known as the spin-lattice relaxation time. In the transverse case, the decay of the xy magnetization component to it's equilibrium state of zero, is described. Transverse relaxation is characterized by the exponential time constant, T_2, known as the spin-spin relaxation time.

Both of these processes, longitudinal and transverse, result from the interaction of the nuclear magnetic moments, μ, with the fluctuating local magnetic fields, B_{local}, generated by their environment through sevedral mechanisms, the main one being dipolar interactions. The tumbling motion of molecules will randomly alter the orientation of nuclear spins relative to B_0 and to each other, causing a change in the B_{local} environment. Thus, fluctuations in the B_{local} field are rendered time dependant by random molecular motion. The time scale of these fluctuations determines their relative contributions to the two types of nuclear magnetic relaxations.

Longitudinal relaxation involves the recovery of z magnetization to it's equilibrium value, and is intimately associated with B_{local} induced transitions of

nuclear dipoles between the two nuclear magnetic energy states. Acting in a similar manner to a B_1 field, any fluctuating B_{local} field, which has a magnetization component in the transverse plane, may induce the nuclear transitions, although longitudinal relaxation is most efficient when the average frequency of fluctuations in B_{local} equals the Larmor frequency. Dipole-dipole interactions are commonly a cause of these magnetic fluctuations. When a relaxation transition occurs, nuclear spin energy is exchanged with the kinetic energy of molecular motions in the surrounding lattice, resulting in the reestablishment of thermal equilibrium in the spin system.

The return of z magnetization (M_z) to its equilibrium value (M_o) can be described by the first order differential equation:

$$\frac{dM_z}{dt} = \frac{[M_o - M_z]}{T_1} \qquad (12)$$

Decay of transverse magnetization (M_{xy}) to it's equilibrium value of zero can also be described by a first order differential equation:

$$\frac{dM_{xy}}{dt} = -\frac{M_{xy}}{T_2} \qquad (13)$$

Transverse relaxation involves the dephasing of magnetization in the xy plane. Mechanisms that give rise to intrinsic T_2 processes are similar to those involved in longitudinal relaxation. It is the component of B_{local} fluctuations at $\omega \equiv 0$ that contribute to transverse relaxation. Small variations in the B_{local} felt by different nuclei give rise to a distribution of precessional frequencies of the magnetic moments. Consequently, some will precess slightly faster or slower about the z axis than the resonant rotating reference frame. In this frame of reference, there will be a 'fanning out' of the xy magnetization as the nuclear magnetic moments get out of phase with each other. This results in reduction of the xy component of the magnetization vector, and hence dephasing of the NMR signal.

In addition to the irreversible T_2 decay produced by the fluctuating B_{local} environments, static inhomogeneities in the B_o field will contribute a reversible component of transverse relaxation. In this case, the various B_{local} environments felt by different nuclei are constant in time. Application of a spin echo pulse sequence can rephase the nuclear magnetic moments, resulting in partial restoration of the xy component of magnetization vector. Only signal lost due to reversible transverse relaxation can be recovered; the other transverse relaxation process is irreversible due to the random nature of the magnetic field fluctuations which caused the relaxation. These random fluctuations cannot be mechanically duplicated, and therefor this signal cannot be restored through rephasing.

1.2.4 NMR Spectroscopy

An NMR spectrum is the frequency domain representation of the NMR signal, and is displayed as a function of the resonance (Larmor) frequency of the nuclei in an excited spin system. The separation of resonance frequencies from some arbitrary standard reference frequency is called the chemical shift, and is expressed in terms of parts per million (ppm) of the applied static magnetic field.

The resonance frequency of each nucleus is directly proportional to the actual magnetic field experienced by that nucleus. This magnetic field, B_{local}, is affected by several factors in the environment. One factor involves the electronic currents in atoms which are induced by B_o. Electrons surrounding a nucleus are spinning, charged particles, which create a small electronic field, B_σ, surrounding the nucleus, which opposes the direction of the applied field. The magnitude of B_σ is dependant upon the electronic environment of the nucleus. Electron donating groups adjacent to,

or high electron densities in close proximity to, the nucleus will increase the magnitude of the electronic field, thereby decreasing B_{local}, and causing a downfield shift of the nuclear resonance frequency. Similarily, electron withdrawing groups will decrease the sheilding, causing an upfield shift of the nuclear resonance frequency, This electron induced shielding is the basis of the chemical shift. .

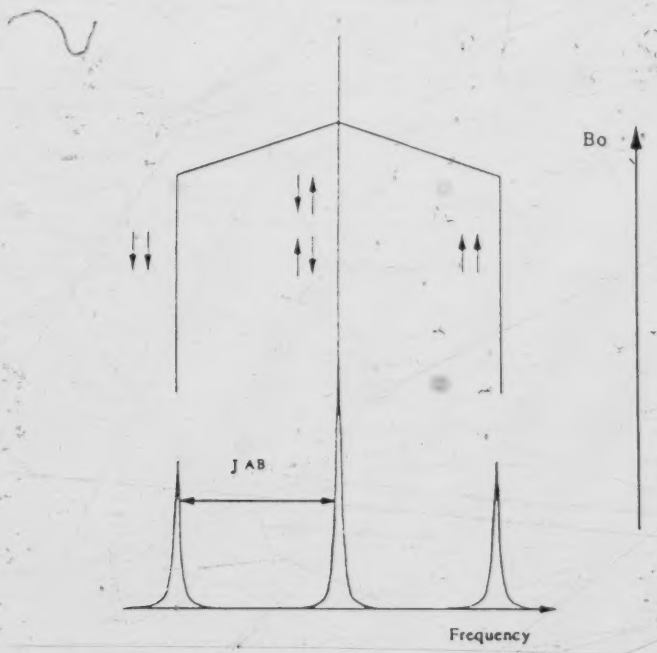

FIGURE 1.04: SPIN COUPLING

A set of 'n' nuclei will split the resonance peak of a similar nucleus into 'n' + 1 peaks. The resultant multiplet is centered at the frequency that one would find an uncoupled nucleus. In the above example, two similar nuclei are splitting a the resonance of a third nucleus with a coupling constant, J, describing the separation of the individual peaks of a multiplet.The arrows indicate the possible orientations, at any one time, of the two neighboring nuclei.

Alterations in B_{local} can also occur from magnetic field contributions from neighboring nuclei. If neighboring nuclei display a net parallel orientation to B_0, the

magnetic fields created by the individual nuclei will increase the Blocal experienced by a particular nucleus, and a resultant upfield frequency shift of the nucleus will occur. Similarly, net antiparallel orientation of neighboring nuclei will decrease the B_{local} of the nucleus. The magnetic field interactions are transmitted through chemical bonds and can create a phenomenon known as spin-spin coupling (Figure 1.04). Thus, identical nuclei in different chemical environments will give rise to spectral peaks at different frequencies. In general, spin-spin coupling is observed only in high resolution spectroscopy and rarely in *in vivo* spectra due to the broad linewidths observed in the latter.

NMR resonances often have a Lorentzian line shape. The peak width at half height, $\Delta\nu_{1/2}$, is a function of the transverse relaxation time, T_2 (35):

$$\Delta\nu_{1/2} = 1/\pi T_2 \qquad (14)$$

In biological tissues where transverse relaxation is efficient, the linewidths tend to be quite broad, relative to linewidths in pure liquids. For example, brain tissue, which has a T_2 of 100 ms, will have spectral widths at half peak height of approximately 3 Hz.

The relative concentrations of the NMR visible metabolite pools can be determined, in principle, from the areas under their respective resonances, since theses ares are proportional to the number of nuclei that contribute to them. In practice, however, quantification of metabolites is difficult. One reason stems from the fact that many resonances overlap one another, making individual area estimations impossible. Also, metabolites in concentrations of less than 1 mM often cannot be detected by NMR.

1.2.5 Localization

The aim of localized spectroscopy is to obtain NMR spectra from one particular region of a tissue, while eliminating signal from surrounding tissue. A number of techniques have been proposed to achieve this, however, each technique has its advantages and disadvantages. Two classes of experiments exist which provide localization of spectra, namely, B_1 and B_0 localization techniques.

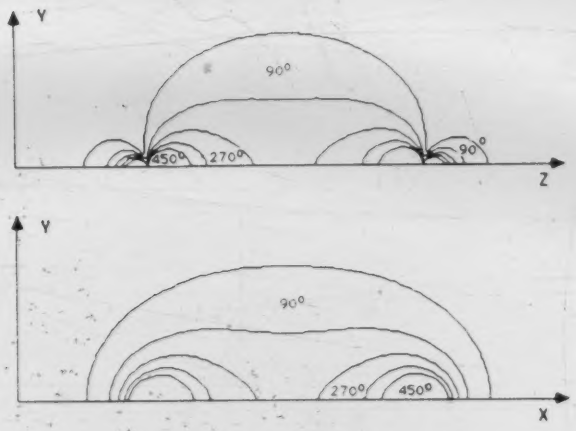

FIGURE 1.05: THE B_1 PROFILE OF A SURFACE COIL

This representation of the B_1 field produced by a surface coil lying in the xz plane shows the high flux bands (270^0 and 450^0) that are produced when the excitatory pulse length has been adjusted to create a 90^0 tip angle at a depth of one coil radius into the sample. Images computer generated by Ian Thomas.

One class of experiments uses B_1 gradients for the localization of the spectra; examples include rotating frame zeugmatography (45) and depth pulses (5). B_1 techniques employ the inhomogeneous RF field of surface coils for depth selection.

In practice, this localization is unsatisfactory since the shape of the sensitive volume follows the B_1 profile of the surface coil used (Figure 1.05). In addition, NMR sensitivity rapidly decreases with increasing distance from the coil, thus only tissues close to the surface of the sample can be readily observed. The depth pulse mode of spectral acquisition is further discussed in Chapter 2.

The second class of experiments use B_0 gradients to achieve localization. Examples of this spectral localization include DRESS (9), ISIS (84), SPARS (66) and STEAM (30). The STEAM method is further discussed in Chapter 2. B_0 techniques have the advantage that it is possible to define the sensitive volume of spectroscopy through the use of slice selective excitation. Each application of a slice selection achieves spatial selectivity through a one-fold reduction in the dimensions of a sample volume. We may therefore select a slice within a 3D sample, a column within a planar slice, or a cube within a column. A disadvantage of B_0 localization is that the use of switched field gradients create time-dependant fields due to decaying eddy currents, which may degrade spectral resolution. Another problem is that spatial localization is subject to a chemical shift dependant offset and consequently NMR signal from two metabolites, with different chemical shifts, will arise from two volumes that are also slightly shifted from one another.

1.2.6 Slice selection

The selective excitation of nuclear spins in a slice within a larger sample volume, is known as slice selection. Nuclei within a chosen slice are excited, without perturbing nuclei on either side of the slice, by the selective irradiation of a system of spins having a distribution of Larmor frequencies imposed by static linear magnetic field gradients.

Consider a linear gradient, G_x, along the x axis of a sample in a static magnetic field (Figure 1.06). The gradient will cause resonance frequencies of nuclear dipoles in the sample to spatially vary:

$$\omega_x = \gamma\ (B_o + G_x\ .\ x\ ) \qquad (15)$$

where x is the distance along the x axis from the center of the gradient. Therefore, in the diagram below, at point A, $\omega_A = \gamma(\ B_0 - G_x.x_1\ )$, and at point B $\omega_B = \gamma B_0$, and at piont C $\omega_C = \gamma(\ B_0 + G_x.x_2\ )$

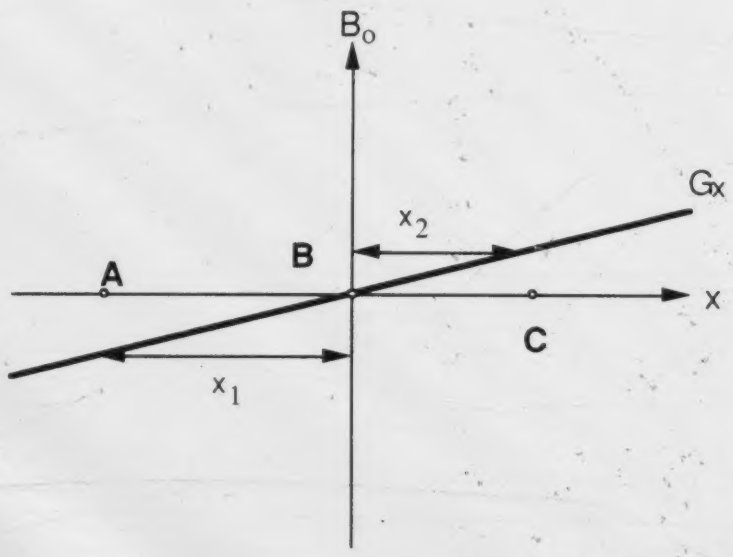

FIGURE 1.06: SPATIAL ENCODING

A pulse from the radiofrequency field, B_1, is then applied to the spin system. In order to excite only some spins, the band width of B_1 must be small compared to the gradient offset of G_x. The narrower the frequency band of the RF pulse, the narrower will be the range of nuclei with corresponding Larmor frequencies that

respond to the excitation, and hence the thinner will be the selected slice. The center frequency of B_1 can be adjusted to select the slice at the desired location within the sample.

A simple square RF pulse time domain envelope would result in the excitation of spins in a region with poorly defined boundaries (35). Modification of the RF pulse is required to excite spins in a rectangular slice with sharp boundaries. This can be achieved through the multiplication of the RF time domain by a SINC (sinx/x) function, the fourier transform of which would result in a rectangular frequency domain envelope. Extensive wings found on a SINC function can be greatly reduced by Gaussian multiplication, without significantly affecting the shape of the resultant RF excitation band.

1.2.7 Imaging

Imaging experiments require that the B_0 field be inhomogeneous so nuclei in different parts of the sample can be characterized by their resonance frequency. This spatial information is encoded into the NMR signal by means of linear field gradients set up in three orthogonal directions. For acquisition of a two dimensional image, one gradient is used to localize the signal to a slice using selective excitation. The other two gradients then encode spatial dependency of the sample into the NMR signal. An image is produced through the application of a two dimensional fourier transformation. The principles of 2D NMR imaging are covered in the literature. (69)

Images reflect not only the proton density at various points throughout a sample, but also the magnitude of the transverse and longitudinal relaxation. An images represents a mixture of these three parameters. However, it is possible to vary

the experimental conditions in such a way that the image is particularly sensitive to one of the parameters.

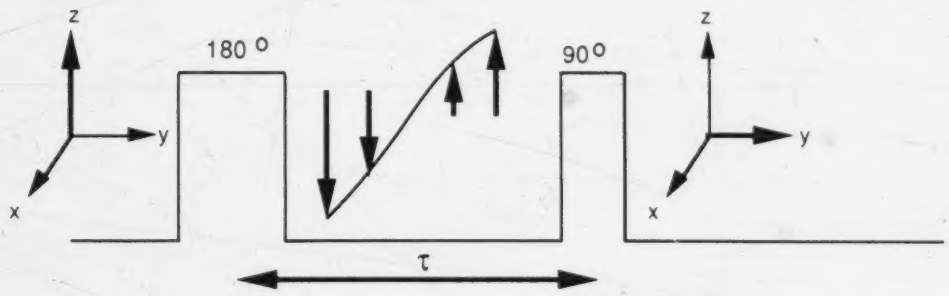

FIGURE 1.07: THE INVERSION RECOVERY PULSE SEQUENCE

T_1 weighted images are measured with an inversion recovery NMR sequence. (Figure 1.07). Following a 180° inversion pulse, the net magnetization of the perturbed spin system lies along the -z axis. Longitudinal relaxation then occurs during a time interval, τ, allowing z magnetization to recover towards its equilibrium value, M_0, with a time constant, T_1. In order to detect the extent to which M_z has recovered after the interval τ, a 90° interrogation pulse is applied, and the subsequent FID is recorded. By repeating this sequence several times, each with a different value of τ, the rate of decay of M_z can be calculated. T_1 can then be obtained from a plot of $\ln [M_0 - M_z (\tau)] / 2M_0$ versus τ which yield a straight line of slope $-1/T_1$. (35)

A method of determining T_2 employs a spin-echo pulse sequence (Figure 1.08). The 90° pulse tips the magnetization into the xy plane and the magnetization then precesses about the z axis. Due to different B_{local} experienced by the various nuclei (refer to section 1.2.3) some will precess faster or slower than others. After a

time interval, τ, a 180° inversion pulse is applied. Instead of dephasing further, components of the magnetization now begin to moye closer together, and at a time τ following the 180° pulse, spins will be refocussed. This results in the formation of an echo at a time 2τ after the initial 90° pulse.

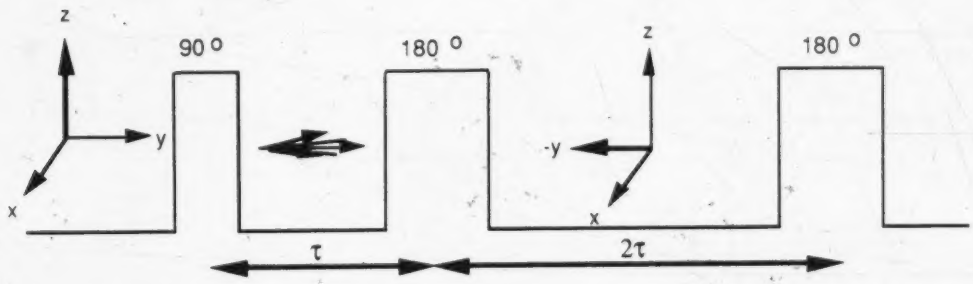

FIGURE 1.08: THE SPIN ECHO PULSE SEQUENCE

The magnitude of the magnetization decreases during the interval 2τ due to irreversible transverse relaxation, and hence the NMR signal is reduced in intensity from the initial signal immediately following the 90° pulse. If the signal is allowed to further dephase, a second 180° pulse can be applied at a time 2τ following the previous inversion pulse. Again, spins will begin to refocus, and a second echo can be acquired at a time τ following the second inversion. The magnitude of the magnetization is further decreased due to the occurrence of more irreversible transverse relaxation. More 180° pulses can be applied with an interval of τ between subsequent inversions. Corresponding echoes will have progressively less magnetization, until finally transverse relaxation causes loss of all coherence of the xy magnetization vector. T_2 measurements can be calculated by plotting the ln (M_{xy}) versus time which yields a straight line of slope $-1/T_2$ (35).

1.3 Introduction to the Central Nervous System

The human central nervous system perceives and responds to environmental stimuli, controls thoughts and memory, and regulates many basic bodily functions. Peripheral nerves and ganglia are involved in the relay of electrochemical messages to and from the central nervous system (CNS). Peripheral nerves (spinal and cranial) carry sensory impulses to, and motor impulses from the brain, while ganglia are involved in the autonomic innervation of smooth muscle, cardiac muscle and glands. The central nervous system itself is composed only of the brain and spinal cord.

1.3.1 Normal Brain Physiology

Enclosed within the protective skull and surrounded by the cerebral spinal fluid, the brain is buffered from physical injury. Four ventricles are found within the brain structure, each filled with cerebrospinal fluid (CSF). There are several anatomically distinct regions of the CNS: the spinal cord, medulla oblongata, pons, midbrain, diencephalon, cerebellum and two cerebral hemispheres. It is the latter region that composes the majority of brain mass.

The hemispheres contain two regions of gray matter: the corpus striatum, found medially, and the cerebral cortex, which forms a thin layer along the outer edges of the hemispheres. Between the two regions of gray matter lies an expanse of white matter. Both tissue types are composed of support cells (oligodendrocytes, astrocytes and microgliocytes) and parenchymal cells (neurons). Neurons have a unique cellular structure designed to allow rapid transmission of nerve impulses (Figure 1.09).

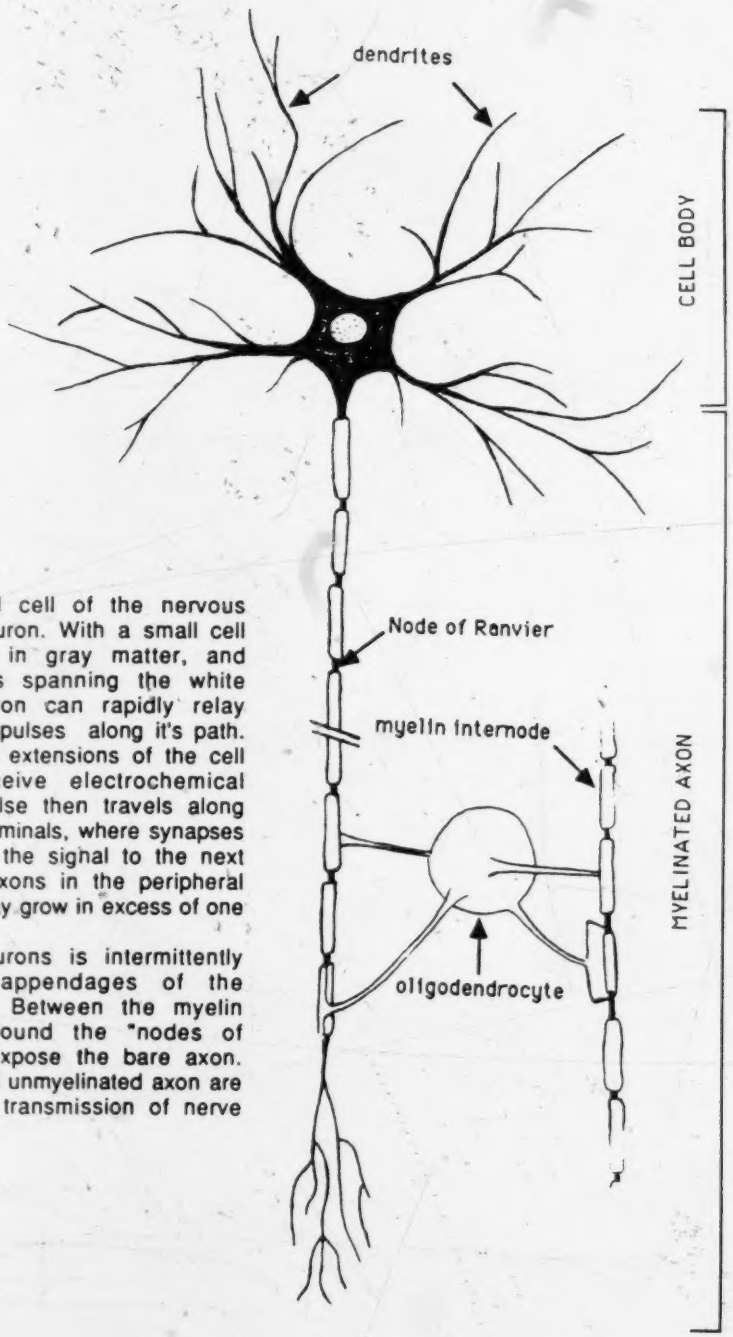

Figure 1.09
THE NEURON

The parenchymal cell of the nervous system is the neuron. With a small cell body embedded in gray matter, and myelinated axons spanning the white matter, the neuron can rapidly relay electrochemical impulses along it's path. Dendrites are the extensions of the cell body which receive electrochemical stimuli. The impulse then travels along the axon to the terminals, where synapses occur to transmit the signal to the next neuron. Some axons in the peripheral nervous system may grow in excess of one meter in length.

The axon of neurons is intermittently myelinated by appendages of the oligodendrocytes. Between the myelin internodes are found the "nodes of Ranvier", which expose the bare axon. These segments of unmyelinated axon are important for the transmission of nerve impulses.

Gray matter contains mainly the cell bodies of neurons while white matter has a high concentration of myelin-covered dendrites. A network of capillaries is found throughout the hemispheres providing the nutritional supply required by the active parenchymal tissue.

The brain parenchyma in adults is a non-dividing tissue. Growth of brain stops around puberty and cells remain quiescent in their differentiated form. Subsequent division of parenchymal cells cannot occur; they are fixed post-mitotic. The glial cells (oligodendrocytes, astrocytes and microgliocytes) form the stromal (structural and supportive) component of brain. Unlike neurons, glial cells may revert back to a proliferative form in response to damage. Stem cells from the subependymal plate may function in the regular repair and slow turnover of the glia, however it is the endothelial cells of the blood vasculature which undergo most rapid cell division. Only actively proliferating cells undergo mitosis, which is considered to be the stage of the cell cycle in which the cells are most prone to damage by irradiation.

The neurons are metabolically active in the transmission of electrochemical nerve impulses which travel from the axon of one nerve fibre to the cell body of the next. Although nerve impulses can move along all nerve fibres, myelin-coated axons experience a much more rapid movement of the depolarization wave at a lower expense of energy. (Figure 1.10)

Axons in the central nervous system are enveloped with a myelin sheath provided by the oligodendrocytes. Oligodendrocytes are glial cells which have a small cell body and numerous broad, flat appendages branching outward from the cell. Each appendage is a membrane bilayer rich in cholesterol and phospholipids (especially sphingomyelin) and low in water content. By wrapping several times

around a section of the axon, the extension of the oligodendrocyte forms an internode of myelin (Figure 1.09). Each oligodendrocyte is capable of forming 30 - 50 internodes of myelin, not necessarily on the same axon. Cerebral white matter contains large quantities of myelinated nerve axons. Analysis of proteolipids in rodent brain suggest that 40 - 50 % of the dry weight of white matter is myelin. (73)

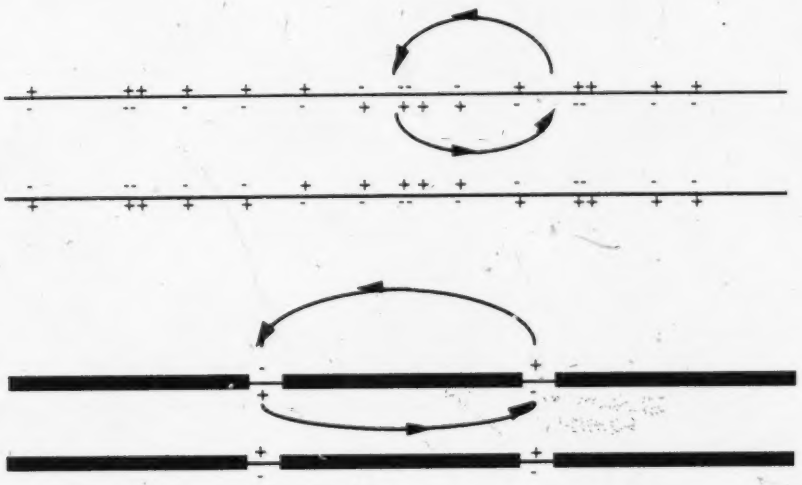

FIGURE 1.10: ROLE OF THE MYELIN SHEATH IN THE TRANSMISSION OF NERVE IMPULSES
Conduction of a nerve impulses involves a wave of depolarization moving along the axon. The upper diagram displays the progression of the depolarization wave in an unmyelinated nerve. In a myelinated nerve (lower diagram) the impulse can only be propagated from one unmyelinated node to the next, thereby forcing the depolarization to be transferred over longer distances in a short time.

1.3.2 Physiology of Human Brain Tumors

A tumor is, by definition, an uncontrolled growth of tissue forming an abnormal mass, the growth of which exceeds and is uncoordinated with that of surrounding normal tissue. Tumors, just like normal tissue, contain parenchymal

cells and support cells. Neoplastic cells form the parenchyma of a tumor, while fibrous tissue, vasculature and normal incident cells form the stroma. Tumors differ from other forms of aberrant growth by the fact that the growth persists in the same excessive manner after cessation of the stimulus which evoked the initial response.

The tumors of any given cell type may show a wide range of behavior in their rates of growth, modes of spread and degree of danger to the victim. Some grow slowly, remain quite local, and may even stop growing eventually. The only danger they present may be in their position in the body, or due to secondary complications such as excessive hormone production. These tumors are called 'benign'. Other tumors of the same cell type can grow rapidly, invading neighboring tissues with finger-like projections that extend outward from the central neoplasm. This type of tumor is 'malignant' and will continue to grow, if left untreated, until death of the host.

Between these two extremes, many tumors with intermediate behavior exist, and it is often difficult to characterize them as one type or another. Histological studies have aided in the classification of tumor malignancy. Benign tumors tend to have well differentiated cells that resemble those of the tissue of origin. The percentage of cells found in mitosis is also similar to that of the tissue of origin. Malignant cells, however, are usually poorly differentiated and show a very high percentage of cells undergoing mitosis. The single, most definitive indicator of malignancy is the presence of metastasized cells in the bloodstream, although not all malignant tumors have the ability to metastasize.

Several malignant human brain tumors exist; astrocytomas being the most common. Histopathalogical grading of astrocytomas into grades one to four (Gr.I -

IV) depends upon the degree of malignancy and morphological characteristics of the tumors. For example, a Gr.I astrocytoma is composed of well differentiated astrocytes, Gr.II astrocytomas are composed of the less differentiated cells, and the high grade astocytomas contain a high mitotic index, giant cells, endothelial hyperplasia and areas of necrosis. The Gr.IV astrocytoma, commonly called glioblastoma multiforme, is a very aggressive tumor with a doubling time of 6-7 days in humans (8). Progression of astrocytomas from one grade to another is rare, although recurrent tumors may be more malignant than the original tumor.

A single transformed cell must undergo approximately 30 doublings before the tumor mass is detectable by conventional diagnostic techniques. Initial cell growth of the tumor is exponential, but the rate of cell loss (relative to cell proliferation) increases with larger tumor size. Tumor cell loss is largely due to the formation of a necrotic region in the center of solid tumors. As the tumor grows, peripheral blood vessels are pushed further from cells at the center of the tumor. Oxygen and nutrients can no longer diffuse to the central cells, causing necrosis. Oxygen deprivation also creates a hypoxic cell fraction surrounding the region of necrosis.

Hypoxic cells are relatively radioresistant due to decreased levels of oxygen being available for fixation of radiation-induced free radicals. Regeneration of the tumor may occur following radiotherapy due to this hypoxic population of cells. Clinical experience has shown that glioblastoma patients have a mean life expectancy of only nine months (8), usually as a consequence of tumor recurrence at or near the original site.

1.3.3 Energy Metabolism in Brain

In the brain, there is a constant demand for energy to support trophic functions, synthesis of neurochemicals, and transmission of nerve impulses. As in all organ systems, the main foodstuff for energy metabolism is the glucose molecule. A constant supply of glucose is pumped into the brain via the bloodstream, however, the actual concentration of free glucose in brain is lower than in most other tissues. (37). The brain does have a large pool of free amino acids, the most abundant one being glutamate (8-12 μm/g). This provides an alternate source of foodstuff for energy metabolism in times of glucose deficiency.

Glucose metabolism in brain is composed of three different stages: glycolysis, the citric acid cycle and oxidative phosphorylation. Glycolysis in brain is irreversible. It involves the breakdown of glucose molecules into two pyruvate molecules, with the release of ATP and NADH. This reaction takes place in the cytoplasm of the cell. The overall chemical equation is as follows:

$$Glc + 2\ Pi + 2\ ADP + 2\ NAD^+ \text{----> } 2\ Pyr + 2\ ATP + 2\ NADH + 2H^+ + 2\ H_2O$$

The next step, the citric acid cycle, occurs in the mitochondria of the cell:

$$Pyr + 4\ NAD^+ + FAD + GDP + Pi \text{ ---} 3\ CO_2 + 4\ NADH + 4\ H^+ + FADH_2 + GTP$$

Each pyruvate reacts with coenzyme A to form Acetyl Co-A (Figure 1.11), which then enters a cyclic chain of events that release high energy metabolites, although none in the form of ATP.

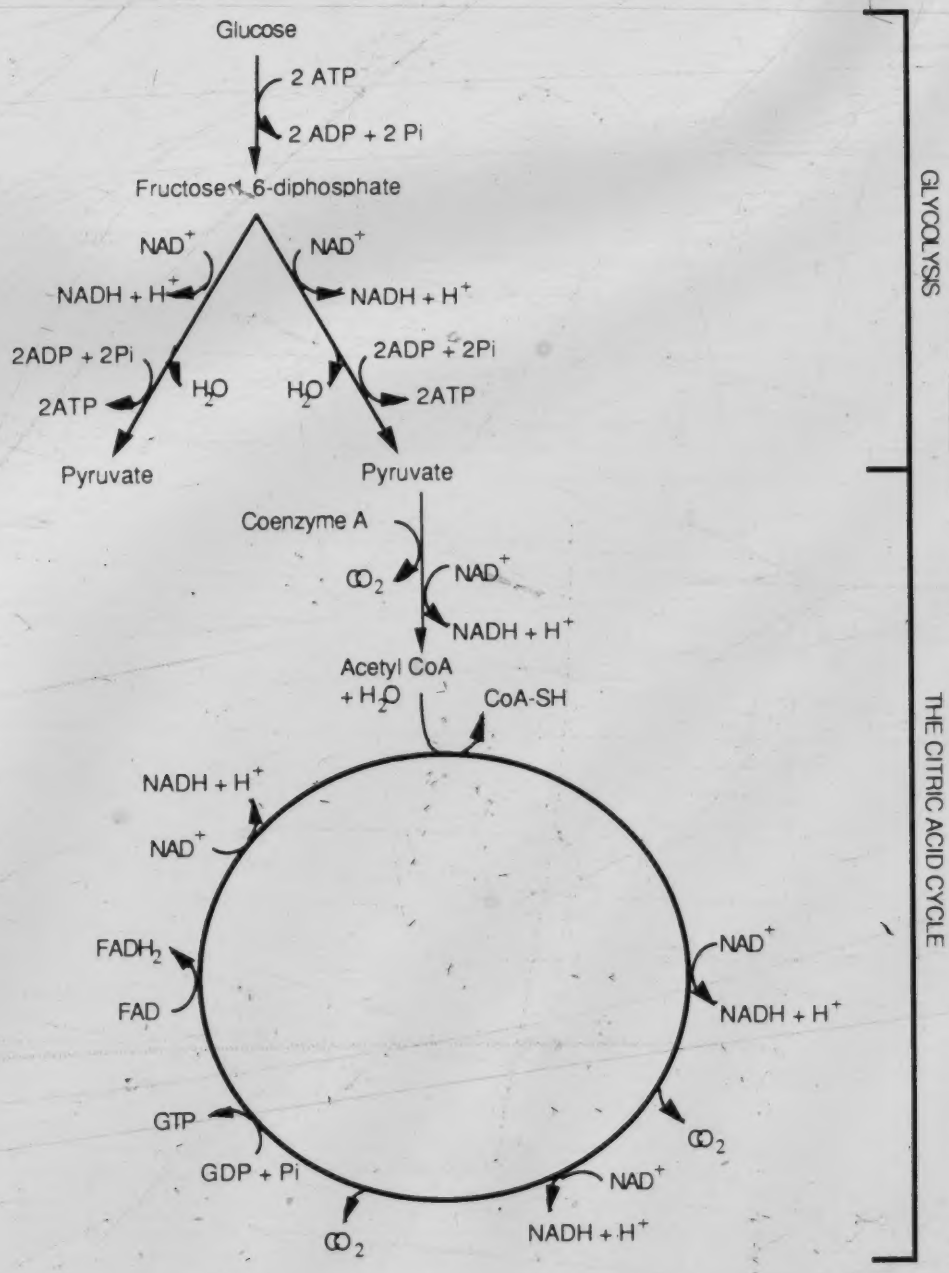

FIGURE 1.11: THE ENERGY METABOLISM PATHWAY

NADH and $FADH_2$ contain energetic protons, while GTP possesses a high energy phosphate. Both NADH and $FADH_2$ can undergo oxidative phosphorylation to produce ATP. Oxidative phosphorylation is a complex electron transfer procedure which occurs in the inner mitochondrial membrane. Special proteins called cytochromes undergo redox reactions which transfer protons across the membrane. These protons, in turn, release their energy to form adenosine triphosphates. NADH molecules are capable of producing three ATP while $FADH_2$ can only yield two.

Each molecule of glucose has the potential to convert 38 molecules of ADP to ATP. However, this will not necessarily occur. Often metabolic side paths will scavenge some of the molecules produced by glucose metabolism. For example, glucose-6-phosphate can be removed from the glycolysis pathway to be used as a precursor for the production of nucleic acids. Similarly, dihydroxy acetone phosphate is removed for the production of prostaglandins, which are important for the normal functioning of brain. The theoretical yield does give an idea of the amount of energy stored within the bonds of a molecule as simple as glucose.

1.3.4 Phosphorus Metabolism in Brain

Phosphorus metabolism includes the biochemistry of the high energy phosphates in brain, as well as other phosphate containing compounds. The largest contribution to the phosphate pool in brain tissue comes from the phosphodiesters. These include the lipids phosphatidylserine (PS), phosphatidylcholine (PC), phosphatidylethanolamine (PE), phosphatidylinositol (PI), sphingomyelins and plasmalogens. Approximately 20% of dry cell weight is phospholipids from membrane structures, although cells composing the myelin sheath in brain

(oligodendrocytes) have a much higher concentration of phospholipids than other neuroglial cells. Apart from their structural capacities, the phosphodiesters serve several important metabolic roles. Plasmalogens can be converted to prostaglandins and prostacyclins, which have a variety of potent biological activities of a hormonal or regulatory nature. Sphingomyelin possesses an insulating capacity against electrical charges, and is found in high concentrations in the myelin sheath of nerve axons. Another important metabolically active phosphodiesters is phosphatidyl inositol; it is an integral part of the "PI cycle" and indirectly stimulates intracellular Ca^{++} release, which in turn regulates many enzymatic processes.

intermediates in the biosynthesis of nucleotides	intermediates in lipid metabolism	components of the energy metabolism pathway
ribose-5 phosphate	phosphocholine	glucose-6-phosphate
inosine monophosphate	phosphoethanolamine	phosphoenolpyruvate
adenosine monophosphate	phosphoserine	fructose-6-phosphate
guanine monophosphate	phosphoinositol	fructose-1,6-diphosphate
cytosine monophosphate		dihydroxyacetone phosphate
thymine monophosphate		phosphoglycerate
uracil monophosphate		α glycerophosphate
		phosphoglyceroyl phosphate

TABLE 1.00: PHOSPHOMONOESTERS FOUND IN BRAIN

Various phosphomonoesters (PME) are also found in significant quantities in brain tissue, and are listed in Table 1.00. The phosphomonoesters are mainly intermediary metabolites, precursors or breakdown products, of nucleotides, lipids,

or molecules involved in cellular energy metabolism. Changes in the concentrations of PME may prove to be a good indicator of cell damage.

Adenosine triphosphate (ATP), phosphocreatine (PCr) and inorganic phosphate (Pi) are three phosphorus containing cerebral compounds which reflect the energy state of brain cells. High levels of ATP must be maintained to ensure cellular homeostasis. ATP is not used for storage of energetic phosphates, but rather acts as a transporter and supplier of energy. During excitation, nerve cells have a high demand for energy, and ATP is degraded to provide this energy:

ATP ---> ADP + Pi + energy

The glucose metabolism pathway normally produces sufficient supplies of energy to convert adenosine diphosphate and inorganic phosphate back into ATP:

ADP + Pi + energy ---> ATP

During times of energy stress, the rate of ATP production by glucose metabolism is slower than the rate of utilization. To avoid depletion of ATP, phosphocreatine acts as a buffering agent in neurons by contributing high energy phosphates:

ADP + PCr ----> ATP+ Cr

Consequently, during energy stress, ATP utilization will cause an increase in the concentrations of ADP and Pi in the cell, while breakdown of phosphocreatine will decrease PCr concentrations and temporarily increase intracellular creatine levels. The concentrations of these metabolites are all interrelated; changes in one will invariably effect the others.

1.4 Introduction to Radiology

The discovery of X-rays in 1895 opened up an entirely new era for the field of diagnostic and therapeutic medicine. Since then, the capacity for ionization has been observed in γ-rays, neutrons, α particles and heavy ions. Each of these forms of radiation is capable of depositing sufficient doses of energy in molecules to excite electrons beyond their atomic orbitals.

Use of radiation in medicine exceeded the knowledge of its biological effect. Superficial malignancies were being treated with large single doses of X-rays soon after the turn of the century. Ailments as trivial as ringworm warranted radiation treatment, and these patients sometimes returned later with symptoms associated with radiation damage (27). Investigations in radiobiology were suddenly increased due to public pressure following the detonation of the two bombs in Japan at the end of the World War II. Cell culturing techniques developed during the 1950s provided another breakthrough by allowing scientists to observe cell inactivation by radiation directly. Research continues presently, now concentrating on radiobiology at the molecular level, however there is much yet to be discovered before we have a complete understanding of the effects of radiation on cells and tissues *in vivo*.

1.4.1 X-radiation

At the high energy end of the electromagnetic spectrum lie both X-rays and γ-rays. Although physically identical, the two forms of electromagnetic radiation originate from different sources. Gamma rays are emitted by decaying radioactive nuclei, while X-rays are produced by means of several mechanisms, namely,

electronic transitions between high and low energy orbitals, velocity changes in high speed electrons (bremsstrahlung), or vibrations of electrons. The energy of X-rays utilized in radiotherapy (1.25 - 25 MeV) exceeds that of diagnostic procedures (12.5 - 125 keV).

Due to the uncharged nature of a photon beam (X-ray or γ-ray) it cannot ionize directly the sample though which it passes, but must first transfer it's energy to a small number of "primary" electrons. These primaries are liberated from their atomic orbitals, and absorb surplus energy from the photon; X-rays of therapeutic strength transfer their energy mainly through Compton interactions while the lower energy diagnostic X-rays favor photoelectric interactions. High energy primary electrons travel along a "track", interacting with the molecules that they pass through and causing excitations and ionizations. Approximately 33 eV are required to cause ionizations in biological tissues. In conventional radiotherapy, treatment fractions of approximately 200 centigrays (cGy) are imparted to tissue, which corresponds to 3.75×10^{14} ionizations per gram of tissue. (200 cGy = 1.25×10^{16} eV/g).

Because the amount of energy deposited in a given tissue mass strongly influences the intensity of the resulting biological effects, the concepts of absorbed dose and linear energy transfer have been introduced to specify such energy deposition. The absorption unit, the gray (Gy), describes the total energy absorbed per 100 g of matter, while linear energy transfer (LET) describes the distribution, in space and time, of the ionizations per unit distance along the radiation track. Both the total absorbed dose and the distribution intensity of ionizations and excitations, govern the probability of biological changes. Cells receiving numerous ionizations are more apt to display visible alterations than cells more sparsely ionized. Primary

electrons deposit energy diffusely in tissue, although ionizations occur more frequently near track ends where the electrons begin to lose momentum.

The quality of radiation should also be considered, especially when considering a particular type of radiation for a specific purpose. The quality, or penetrating ability, of radiation determines to what depth the beam can infiltrate. The intensity of the photon beam decreases exponentially with distance from the surface of a sample, as described by Equation 16:

$$N = N_0 e^{-\mu x} \qquad (16)$$

Where N_0 is the initial number of photons and N is the number of photons penetrating to a depth, x. μ is the linear attenuation coefficient, relating the fraction of photons that interact per unit distance of the tissue through which the beam passes. The primary electrons have the capacity to travel beyond the depth to which the original photon beam penetrates.

1.4.2 Radiobiology

Ionizing radiation sets off a series of chemical and biochemical processes which are initiated less than one second after radiation enters the living tissue. Within the first 10^{-12} seconds ionizations and excitations occur in protein, lipid and carbohydrate molecules, as well as in water. The amount of ionizations occurring in the various types of biological molecules is proportional to the relative concentrations of each in the cell. Water, composing approximately 75% of tissue mass, incurs most ionizations and then immediately (within 10^{-6} seconds) proceeds to undergo a process known as radiolysis. Radiolysis results in the production of two highly

reactive free radicals, namely hydrogen (H·) and hydroxide (OH·). These free radicals are highly oxidative, and will scavenge hydrogen radicals from biological molecules, causing indirect radiation damage:

$$R\text{-}H + H\cdot \longrightarrow R\cdot + H_2$$

$$R\text{-}H + OH\cdot \longrightarrow R\cdot + H_2O$$

In vitro studies by Chapman *et al* (20) showed that scavenging of water free radicals by DMSO (dimethylsulfoxide) reduced radiation induced damage in cells by 62%. This suggests that most damage incurred by cells following irradiation is actually due to the harmful effects of water free radicals rather than directly by radiation.

Free radical damage of biological molecules can be reversible; fixation or repair of the damage occurs less than one second following the creation of the radicals. Repair occurs directly through reaction of the organic free radical with a hydrogen radical to reestablish the initial chemical bond. The presence of oxygen impairs the repair process by scavenging, and reacting with, free radicals to produce a superoxide:

$$R\cdot + O_2 \longrightarrow RO_2\cdot$$

Superoxide radicals are relatively stable intermediates that will not readily liberate their oxygen, thereby fixing the radiation-induced damage. The proportion of biological radical fixation versus repair is dependant upon the availability of oxygen in the damaged tissue.

Radiation damage occurs in numerous subcellular components, however, the redundancy of most enzymes and organelles prevents accurate estimation of their inactivation. Only the DNA molecules are unique; damage to these molecules may extensively effect metabolism within a cell by altering the production of proteins and

impairing cellular processes. Fixation of radiation-induced genetic mutations occurs when the damaged DNA is replicated during the synthesis phase (S-phase) of the cell cycle. Permeability of membranes may also be altered through the harmful effects of radiation. Cellular integrity, therefore, is vulnerable to radiation-induced changes resulting from damage incurred by DNA or damage to the plasma membrane.

Radiation-induced alterations in the membrane structures are not well understood, but may occur secondary to, or separately from, damage to DNA molecules. Since damage to DNA is not fixed until the pre-mitotic S-phase, non dividing cell populations, which do not undergo DNA replication, have a greater potential to repair nuclear damage. However, membrane damage can be more debilitating, since the plasma membrane is responsible for maintaining the intracellular environment required for normal cell functioning. Non-dividing cells, therefore, often experience interphase (due to damaged membranes) rather than mitotic (due to replication of damaged DNA) deaths.

Certain biochemical changes have been observed in neurons following irradiation. One such change is the lysis of chromosomes which can occur several hours following the application of large doses of radiation, and may be associated with the conglomeration of lysosomes in irradiated cells. (59) Acid phosphatases and other destructive enzymes found in the lysosomes are found in increased concentrations in radiation damaged tissue. Further proof of chromosomal lysis arises from a sedimentation experiment on DNA from irradiated rat brains (118) which indicates the appearance of slow sedimenting (damaged) DNA up to four weeks following the application of a single dose. Density of the genetic components increases during the next four weeks, possibly due to repair processes in effect. The slow sedimentation fraction then manifests itself again 10 weeks post radiation and

remains as a marker of permanent damage to the DNA. Humans, due to their slower metabolism, may experience the same sequence on an extended time scale.

Radiation damage to cells has been described by several mathematical models (19), but all models include two components of cell targeting. The α component represents irreparable damage, whereas the β component reflects molecular lesions which potentially may be repaired. Cellular recovery is based upon the efficiency of the molecular repair processes; cells may or may not recover from the damage imparted by single or multiple ionization events. Thus, radiation damage of a tissue is a combination of the nature and extent of the original radiation damage as well as the efficiency of inherent repair processes.

1.4.3 The Effects of Radiation on the CNS

Both acute and delayed damage is caused in the CNS by therapeutic radiation. Acute edema of the brain occurs during the treatment period. Symptoms due to radiation induced edema include headaches, nausea and vomiting (102). These symptoms can be alleviated with corticosteroid therapy (74). Subacute edema, which is associated with demyelination, can occur within several weeks of radiotherapy (65,75,97). The spread of edema is not random but tends to follow white matter tracts (24). A decrease in the number of oligodendrocytes secondary to irradiation supports the theory that subacute edema is associated with demyelination (13).

The controversy that exists is 'what came first, edema or demyelination?'. X-ray diffraction studies of chemically induced edema in neuronal cultures shows a splitting of the myelin at the interperiod line. Fluid rapidly accumulates in the normally dehydrated myelin, followed by the formation of vacuoles and subsequent

degradation of the sheath.(61) Elevated levels of myelin basic protein have been found in the cerebrospinal fluid following radiation of the CNS, thereby reflecting demyelination (99) . Macrophages, which migrate towards necrotic and damaged tissue, also release large quantities of lipases and acid proteases which are destructive to myelin. Although demyelination normally occurs in conjunction with vascular damage, animal experimentation has shown regions of myelin loss with no vascular alterations. (2,114)

Damage to the blood brain barrier is another consequences of exposure to radiation. The lining of the vasculature in the brain consists of rapidly dividing endothelial cells. These cells form a selectively permeable barrier between blood flowing within the capillaries and the surrounding parenchyma. Following irradiation, the endothelium becomes damaged and the permeability of the capillary walls increases. This allows plasma and toxic substances to enter brain tissue, possibly contributing to the late delayed effects of radiation.(110,16)

This delayed damage, which occurs several months or years following exposure, is a progressive phenomenon. For the central nervous system, two hypotheses exist to account for delayed radiation necrosis. According to one hypothesis, damage to the glial cell population is regarded as the primary stage in the development of the lesion, while the other hypothesis considers the vascular system to be the primary target. Irradiation of rat spinal cord shows that therapeutic radiation doses result in vascular damage (112), while mitotic studies performed on irradiated brain cells suggest that radiation damage to glial stem cells of the subependymal plate eventually leads to white matter necrosis (54). Since evidence supports both hypotheses, late delayed necrosis may be caused by a combination of vascular damage and the direct effect of radiation upon glial cells.

Histologically, white matter of the brain appears to be more sensitive to radiation damage than grey matter, and the variation in dose response of the different white matter structures is also evident. (15). Blood vessels in damaged CNS appear dilated possibly due to necrosis of perivascular smooth muscle. Enlargement of endothelial nuclei is correlated with hyperplasia and hypertrophy of astrocytes, both consequences of brain irradiation. (15) Vasculature in irradiated regions displays thickened and hyalinized walls often leading to the occlusion of blood vessels. Regions of necrosis develop in brain parenchyma made ischemic by the vascular occlusions. Development of necrotic lesions appear first as minute focal lesions scattered throughout the white matter (16). Progression of necrosis involves enlargement and coalescence of the lesions. The areas of necrosis are often surrounded by regions of vascular proliferation and zones of demyelination (23). Symptoms associated with demyelination have been observed in some patients who have received radiation therapy (11,52) Other adverse symptoms related to late radiation damage include headaches, speech impediments, ataxia, whole body or focal seizures, and visual impairment.(70,42) Neuropsychiatric effects such as euphoria, confusion, memory loss, intellectual deficits, depression and (in extreme cases) dementia may also occur. (11,70,72)

1.4.4 Radiotherapy of the CNS

The therapeutic benefits of using radiation in the treatment of cancer were realized over half a century ago. The theory behind radiotherapy, is the fact that cells in the mitotic stage of the cell cycle are more sensitive to damage by ionizing radiation than cells in other stages of the cell cycle. Tumor cells, which divide more rapidly

than surrounding, normal tissues, will have a higher mitotic index; a greater percentage of cells undergoing mitosis at any one time. Therefore, the tumor cells should be more prone to radiation damage than surrounding tissues. This theory applies particularly to organs such as brain, in which the parenchymal cells are quiescent.

Brain tumors, such as meningiomas, oligodendrogliomas, astrocytomas and glioblastomas, have conventionally been treated with a megavoltage photon beam utilizing total doses of 6000 cGy delivered in daily fractions of 200 cGy. Since cells are most sensitive to damage by radiation while in mitosis, fractionation allows the rapidly dividing tumor cells to progress into mitosis between subsequent doses of radiation, while the non-dividing brain normal brain cells remain in their more resistant phase. Theoretically, the tumor cells should be more radiosensitive than the surrounding normal brain. Nonetheless, survival studies have indicated that many tumor cells display a high inherent radioresistance, regardless of their high mitotic index (119). Radiosensitivity may involve either the susceptibility of cells to initial damage imparted by ionizing radiation, or the capacity of cells to repair the potentially lethal damage. Perhaps the most radioresistant of all tumors is the Glioblastoma Multiforme.

Glioblastoma Multiforme is a malignant brain tumor found in humans. It is a very aggressive tumor, and generally cannot be successfully treated utilizing current conventional radiotherapy schemes. In attempts to enhance the long term survival of Glioblastoma patients, alternative treatment schedules are now being used. Previous clinical experience has demonstrated that human malignant gliomas display a dose-response behavior that gives rise to better control and survival with increased dose of radiation. In addition, if the tumor cells are proficient in repair, decreasing time

between fractions will decrease the repair capacity of these cells. One of the promising avenues in the treatment of Glioblastomas is, therefore, to increase the total radiation dose using a hyperfractionation technique in the hope of exploiting the repair potential between normal CNS and tumor tissue. Hyperfractionation treatment involves the application of radiation multiple times daily, and potentially increasing damage to tumor cells relative to normal tissue by increasing the total dose by 20 - 30% above the dose achieved with conventional fractionation.

Tumor cell-kill may also be enhanced through the application of chemical agents that increase the radiosensitivity of tumors compared to normal tissue. One such radiosensitizer, IUdR (iododeoxyuridine), can be intravenously infused into cancer patients. IUdR is a modified nucleotide that is rapidly incorporated into proliferating tumor cells, but not the surrounding quiescent cells, weakening the DNA strands of tumor cells. The weakened DNA is then prone to breakage at the IUdR junctions during radiotherapy. Unfortunately, IUdR can only be infused in limited amounts due to its toxicity.

1.5 Introduction to NMR Spectroscopy of Brain

1.5.1 Cerebral Phosphorus Spectroscopy

^{31}P is the only naturally occurring phosphorus isotope, comprising 100 percent of phosphorus in biological systems. The brain contains a limited number of phosphorus containing metabolites in concentrations large enough to be detected by NMR. These metabolites and their relative chemical shifts are summarized in Table 1.01.

Compound	% of ^{31}P in vivo	% of ^{31}P in vitro*	ref.	Chemical shift (ppm)
total phosphomonoester (PME)	7 ± 1.3	13.8±3.8	(17)	6.4
phosphoethanolamine + ribose5-PO4		5.8	(89)	6.9
phosphocholine		2.2	(89)	6.4
inorganic phosphate (Pi)	9 ± 1.8	13.4 ± 1.6	(17)	4.8
total phosphodiester (PDE)	38 ± 7.3	8.3 ± 1.6	(17)	2.7
phosphoethanolamine		2.4 ± 0.2	(64)	3.1
sphingomyelin		1.3 ± 0.3	(64)	2.9
phosphatidylserine		1.4 ± 0.1	(64)	2.6
phosphatidylcholine		2.9 ± 0.2	(64)	2.1
phosphocreatine (PCr)	17 ± 2.4	16.1 ± 1.6	(17)	0
adenosine triphosphate (ATP)				
γ peak	9 ± 1.2			-2.5
α peak	11 ± 1.9			-7.8
β peak	9 ± 1.7	14.2 ± 2.2	(17)	-16.9

* refers to amounts found in aqueous brain extracts

TABLE 1.01: PHOSPHORUS NMR RESONANCES OF BRAIN SPECTRA

A typical ^{31}P spectrum of a human brain at 1.5 Tesla shows only seven distinguishable peaks (Figure 1.12). The baseline hump observed in the spectrum is broad resonance originating from membrane bound phospholipids. Poor localization techniques may result in an increase in the baseline hump due to additional contribution to the broad resonance by phosphates in the skull.

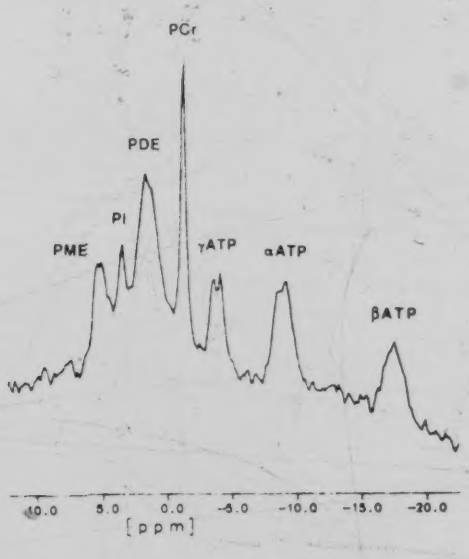

FIGURE 1.12:
A TYPICAL *IN VIVO* PHOSPHORUS NMR SPECTRUM OF HUMAN BRAIN AT 1.5 TESLA

Several of the metabolites with similar chemical shifts are difficult to resolve when doing *in vivo* NMR. As mentioned in Section 1.3.4, the large phosphodiester peak centered at 3 ppm and the phosphomonoester peak centered at 6 ppm are each composed of resonances from numerous different sources. The phosphoethanolamine (PE) and phosphocholine (PC) lipids compose the majority of the PDE peak area due to their relatively high concentrations in cells (17). Similarly, the phosphomonoester

peak is composed mainly of phosphoethanolamine and phosphocholine. Recently, work by Luten *et al* (67) has, through the use of proton decoupling, shown splitting of both the monoester and diester peaks with phosphorus NMR.

Phosphorus spectroscopy is an effective probe in the *in vivo* generation and utilization of phosphate bond energy. The key metabolites in brain phosphorus energy metabolism (ATP, Pi and PCr) can all be detected by NMR spectroscopy. In brain cells, phosphocreatine acts as a buffer to maintain ATP levels during times of energy stress, when the rate of ATP consumption exceeds the rate of production. If high energy phosphates are not readily available from the energy metabolism pathway, ADP will scavenge the phosphorus from PCr to maintain homeostasis of ATP. Consequently, the PCr levels in the cell will decrease when this molecule is used as an alternate energy source. The total phosphate pool in a cell remains unchanged during energy stress (50), and the decrease in PCr levels is reflected in a corresponding increase in the levels of inorganic phosphate. When the energy metabolism of a cell is severely compromised, decreases in ATP levels will occur. Thus, changes in relative concentrations of high energy phosphate metabolites may act as indicators of the degree of energy stress experienced by the brain

A cell undergoes energy stress whenever ATP produced by the glucose energy metabolism pathway cannot replace ATP at the rate at which the molecule is utilized. In brain, this can occur during hypotension or stoke (79,62) when the glucose-rich blood supply to brain is decreased, or during times of hypoglycemia (51,92) when the levels of glucose in blood are very low. Hypotension studies in rats (79) require that the blood flow to brain be decreased by greater than 50% before changes in ^{31}P NMR are detected. Levels of Pi increase and PCr decrease once the cerebral blood flow (CBF) is 40% of normal. The ATP levels remain unaffected until

the CBF is decreased to 30% of normal. Insulin-induced hypoglycemia in rabbits show a sudden decrease in the PCr/Pi area ratio when the blood glucose levels fall to 26mg%. Changes in ATP levels also occur, although these changes are much more gradual. However, similar experiments in human volunteers showed no significant changes in the levels of any of the ^{31}P metabolites (51).

Stroke-induced ischemia can be mimicked in animal models by the clamping of blood vessels leading to brain. Experimentally induced ischemia in mammalian brains shows a slight reduction of the PCr/Pi ratio during mild ischemia (62), and larger changes in the case of more severe ischemia (53,62). In mild ischemia, the ATP levels do not change at all, reflecting maintenance of cell homeostasis. In the case of the severe ischemia, changes in ATP levels (α, β and γ peaks) are observed, but not until the PCr concentration has dropped to half of the initial value (62).

Changes in pH are also observed in ^{31}P NMR studies of energy-stressed brains in animal models. A drop in the pH is associated with the severe ischemia, the lower pH being evident by a shift in the Pi peak. This shift can occur prior to changes in the ATP peak, suggesting that lactoacidosis can develop without the energy state of the cell being severely effected (62).

Measurement of the intracellular pH (pH_i) of brain is an inherent capability of phosphorus spectroscopy. pH affects the chemical shift of phosphorus metabolites, although only Pi and PME are significantly altered within physiological pH ranges (98). Since individual phosphomonoester peaks cannot be resolved in *in vivo* NMR, the Pi peak is typically used as the indicator of pH_i.

Under physiological conditions, inorganic phosphate exists as one of four species of phosphoric acid, and the phosphorus is in rapid exchange between the various forms. Each form has a characteristic chemical shift, and the chemical shift of

Pi (δPi) that we observe in NMR results from an averaged value dependant upon the ratio of phosphorus nuclei found in each separate form. Equation 17 describes the observed chemical shift of inorganic phosphate.

$$\frac{[H_2PO_4^-]\delta_1}{[Pi]} + \frac{[MgH_2PO_4^+]\delta_2}{[Pi]} + \frac{[HPO_4^=]\delta_3}{[Pi]} + \frac{[MgHPO_4]\delta_4}{[Pi]} = \delta Pi \qquad (17)$$

Each term of the equation represents the contribution of each individual chemical shift to the value of the observed shift of Pi.

A derivation of the Henderson-Hasselbach equation has been developed (90) which allows the calculation of intracellular pH from the difference in chemical shift between the PCr an Pi peaks of the NMR spectrum. (Equation 18)

$$pHi = 6.77 + \log [(\delta Pi - 3.29) / (5.68 - \delta Pi)] \qquad (18)$$

The first numerical value represents the pK' (negative log of the apparent dissociation constant) of $H_2PO_4^-$ to $HPO_4^=$. The other two numerical values represent the chemical shift of a basic and acidic solution of phosphoric acid (respectively) in a magnesium solution of physiological concentrations (5 mM). In the basic solution, the phosphorus exchanges between $HPO_4^=$ and the $MgHPO_4$, while the acidic solution contains the protonated equivalents.

Phosphorus spectroscopy has been used to detect high pH levels found in human brain tumors. Astrocytomas and meningiomas display pH values of 0.1 - 0.2 units higher than that of normal brain (82). *In vivo* ^{31}P spectroscopy has also revealed differences in the NMR-visible metabolite concentrations. The most notable change is the decrease in the PCr/Pi peak area ratios. This has been observed in astrocytes, meningiomas and oligodendrogliomas, the latter two showing more than a 50% decrease in the PCr/Pi ratio (82). Portions of the brain tumor may be ischemia or

hypoxic, causing reduced PCr and increased Pi levels due to compromised energy metabolism. Some investigators have also observed high levels of PME in human brain tumors (48,104), although other studies contradict this (82,56).

Differences between the ^{31}P spectrum of normal brain and tumor can be used to distinguish between these two tissues. This capability has been exploited in the monitoring of the effectiveness of radiotherapy on human brain tumors. Phosphorus NMR spectra taken during the course of radiotherapy reveal a progressive change from an 'abnormal' spectrum, to one that closely resembles normal brain tissue (48). A long-term monitoring of normal brain tissue surrounding the tumor may reveal changes in normal phosphorus metabolism induced by radiotherapy.

1.5.2 Cerebral Proton NMR Spectroscopy

Proton NMR spectroscopy provides access to a larger number of metabolites *in vivo* than does phosphorus spectroscopy. Combined NMR and gas chromatography on mammalian brain extracts has led to the identification of almost fifty resonances (Table 1.02). Due to the large number of observable metabolites, and the small chemical shift dispersion, the task of peak identification *in vivo* is often difficult. However, differences among the relaxation times of cerebral metabolites can be exploited to simplify the proton NMR spectrum. Spectra acquired utilizing short spin echo times display numerous NMR resonances, but many of these resonances disappear with increasing spin echo time (τSE). The disappearance of the peaks is attributed to the short relaxation times of the protons contributing to the NMR signal. Brain metabolites with long transverse relaxation times (200-400ms) include protons of NAA, Cho, Cr and lactate.

Chemical shift (ppm)	brain metabolite	proton resonance
0.9	leucine	CH_3
1.0	valine	CH_3
1.2	βOH-butyrate	CH_3
1.3	lactate, threonine	CH_3
1.5	alanine	CH_3
1.7	lysine	CH_2
1.9	acetate	CH_3
	GABA	βCH_3
2.0	NAA	CH_3
2.1	glutamine, glycine	βCH_3
2.3	glutamine	γCH_3
	GABA	αCH_3
2.4	glutamine	γCH_2
	succinate	CH_2
2.5	NAA	βCH
2.7	NAA, aspartate	$\beta' CH$
2.8	aspartate	βCH
3.0	GABA	γCH_2
	lysine	CH_2
	creatine	CH_3
3.2	choline	CH_3
3.3	inositol	H_5
	taurine	NCH_2
3.4	taurine	SCH_2
3.5	threonine, glycine	αCH
	inositol	H_1, H_3
3.6	inositol	H_4, H_6
	choline	NCH_2, γCH, βCH
3.7	alanine, glutamine, glycine	αCH
3.9	serine	CH
	choline	PCH_2
	aspartate	αCH
4.1	inositol	H_2
	lactate	αCH
4.3	threonine	βCH
	choline	αCH_2
4.4	NAA	αCH
6.9	tyrosine	CH
7.2	tyrosine	CH

TABLE 1.02: PROTON NMR RESONANCES OF BRAIN SPECTRA

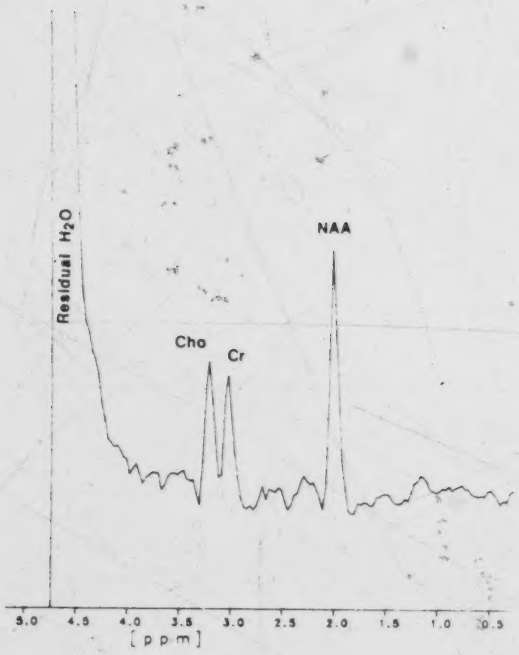

FIGURE 1.13:
A TYPICAL *IN VIVO* PROTON SPECTRUM OF HUMAN BRAIN AT 1.5 T

A typical ^1H spectrum of healthy human brain, acquired using a long SE time (τSE = 134 ms), is shown in Figure 1.13. Only three metabolite resonances are visible in the proton NMR spectrum. These metabolites are N-acetyl aspartate (NAA), choline (Cho) and creatine (Cr). The three peaks result from the methyl protons of the metabolites; the Cr resonance having contributions from the methyl groups of creatine and phosphocreatine. The NAA peak is the most prominent NMR resonance of all the brain metabolites. The chemical shift of the NAA peak is conventionally set to 2.0 ppm and is used as a chemical shift reference by which to identify other proton resonances. The methyl groups of choline and creatine are found at 3.2 and 3.0 ppm respectively. Although pH does influence the chemical shifts of proton resonances, there is little change relative to one another within the physiological pH range (29).

Detailed biochemical information may be obtained from proton NMR on metabolism of free amino acids, fatty acids, and neurotransmitters, as well as energy metabolism. Abnormal energy metabolism can be observed utilizing ^{1}H NMR spectroscopy, through monitoring of the intensity of a resonance due to the methyl group of lactate. This peak appears at a chemical shift of 1.3 ppm and has been observed in brains post-mortem (91), following stroke (12), and in some brain tumors (121). Lactate is found at a concentration of 1.6 mM in the cerebral hemispheres, and therefore cannot be readily detected by NMR in healthy brain tissue. Only when energy metabolism is compromised, forcing an increase in anaerobic glycolysis, will the lactate be visible in a proton spectrum.

Artificially induced hypercarbia in rats has resulted in a decrease of the glutamate/creatine ratio in brain. Decreased pH levels, associated with hypercarbia, are thought to be the cause of this decrease (107). Observation of amino acid derivatives, such as NAA, choline and creatine, may also provide clues to faulty metabolism. Clinical studies of brain following stroke have shown the disappearance of the NAA peak (12). The author suggests that this decrease may be due to the activation or release of degradative enzymes in damaged nerve cells. *In vitro* NMR of irradiated rat brains also suggests an increase in the intensity of the choline resonance, and decreased levels of serine and lecithin (96).

Brain tumor spectra differ remarkably from spectra obtained from healthy brain tissue. In most cases, the concentrations of NAA and creatine + phosphocreatine are reduced below detectability, whereas mobile lipids, lactate and choline containing compounds are generally enhanced. Comparison of spectra from astrocytomas, meningiomas and oligodendrogliomas suggest that histologically similar tumors tend to display similar proton spectra (121). STEAM spectra acquired

with short SE times show the presence of a lipid resonance in all three cases, although this signal disappears at longer SE times. In astrocytomas and meningiomas, the NAA and creatine signals disappear completely, while in oligodendrogliomas, small, but significant, amounts of the two metabolites still remain. Differentiation between astrocytomas and meningiomas can be achieved through comparison of relative areas of the choline and lactate resonances of the proton spectrum. In astrocytomas the lactate peak is larger, while in meningiomas it is the choline peak that dominates over the lactate.

CHAPTER 2: EXPERIMENTAL METHODS

In order to study the effects of radiation upon normal human brain tissue, NMR spectroscopy and imaging were utilized as non-invasive methods of observing potential radiation damage *in vivo*. All NMR experiments were carried out on a 1.5 Tesla Philips Gyroscan clinical system. The 60 centimeter free bore of the unit accommodated all but the largest patients; the analysis of one person had to be discontinued due to his gain in weight. Patients undergoing therapeutic cranial irradiation were analyzed prior to their radiation treatment, then scheduled for further analysis at intervals of 0, 2, 4, 8 and 12 months following completion of radiotherapy. Due to deteriorating health, many patients could not complete the entire course of study.

NMR spectra and images were acquired from a group of healthy volunteers, and a group of patients. T_2 calculated images from patients were taken to monitor the intensity and duration of radiation-induced edema. ^{31}P spectroscopy was performed to monitor alterations in energy metabolism through changes in the high energy phosphate components of the spectrum, while proton spectroscopy hoped to reveal changes in lipid or amino acid concentrations. The procedures used for collection and processing of the NMR data are outlined in this chapter, as are problems encountered with the various procedures.

2.1 Human Subjects

Patients undergoing radiotherapy for treatment of brain tumors at the Cross Cancer Institute in Edmonton were referred to us by Dr. R.C. Urtasun. Many of

these patients had high grade astrocytomas, although some had lower grade tumors. The NMR analysis of healthy volunteers allowed us to establish normal baseline values for our spectroscopy and imaging data. These healthy subjects were friends and acquaintances from around the university. All participants of this study were required to lie still for 1 - 2 hours. Persons with metal implants, or those suffering from claustrophobia, were excluded from the study.

2.1.1 Patient Selection

Brain tumor patients were chosen due to the high dose of cranial radiation they would receive in the treatment of their tumors. Patients entering this study were scheduled to receive radiation doses of up to 8000 cGy utilizing either daily or multiple daily fractions with a 6 Mv linear accelerator as the source of high energy x-rays. One of three different treatment schemes was used to combat the brain tumors:

1) 5000 - 6000 cGy total (for treatment of low grade gliomas and pituitary adenomas)

Total doses of 5000 - 6000 cGy are delivered in daily doses of 180 - 200 cGy, 5 days per week for a period of approximately 6 weeks. The dose of radiation is usually concentrated around the tumor, with peripheral regions of brain receiving little or no radiation.

2) 6000 cGy plus IUdR (for treatment of high grade malignant gliomas)

IUdR (iododeoxyuridine) is a radiosensitizer which is incorporated into the DNA of cycling cells. The dose fractionation of 180 cGy daily is delivered to 3/4 brain volume to a total of 4500 cGy, with an additional 1500 cGy delivered to the tumor plus marginal normal brain.

3) 8000 cGy hyperfractionation (for treatment of high grade malignant gliomas)

Individual doses of less than 100 cGy are imparted to brain three times daily over the course of several weeks, to a total dose of 8000 cGy. These low fractions increase the tolerance of brain and other late reacting tissues to radiation, thus allowing an increase in the overall dose applied (116). 4000 cGy are delivered to 3/4 brain volume while another 4000 cGy is applied to the tumor region plus marginal normal brain.

Upon entering the NMR study, each patient was assigned a number from 1 to 23, and throughout this thesis, individual patients are referred to using their assigned number. Each patient was chosen on the basis of his or her individual prognosis; patients in poor health following surgery were not recommended for this study. Older patients tend to have a poorer prognosis, hence the majority of our patients were relatively young. The study group consisted of both males and females; the actual distribution of age and sex is outlined in Table 2.00.

	31P spec	1H spec	imaging	total
Males 30 - 35	5	2	5	7
Males 36 - 50	3	4	3	7
Males over 50	2	2	2	4
Females 20 - 35	1	1	1	2
Females 36 - 50	2		2	2
Females over 50		1		1

TABLE 2.00:
AGE AND SEX DISTRIBUTION OF PATIENTS IN THE NMR STUDY

All patients who entered the ^{31}P spectroscopy study were also analyzed using NMR imaging. Individuals entered in the ^{1}H spectroscopy study were not imaged.

2.1.2 Healthy Volunteers

Attempts to age-match patients and volunteers proved futile. The healthy volunteers were between 20 and 40 years of age, while most patients were considerably (10 - 20 years) older. From ^{31}P NMR studies on human muscle, there are indications that changes in ATP and PDE levels occur with age (100). This fact was taken into consideration, when analyzing the spectra from older patients, by allowing for a 10% elevation in the PDE/ATP ratio for every increase of 10 years in age. Most of the volunteers were also male, however, comparison of spectra and of images, between males and females, showed no observable differences.

Two volunteers were analyzed, using ^{31}P spectroscopy, several times over the course of a few months to determine normal temporal variations in cerebral metabolite levels. Spectra from opposite hemispheres were also compared, to observe any spatial variation, and to test measurement reproducibility.

2.2 Imaging

2.2.1 Data Acquisition

For acquisition of an image, each patient lay supine on the NMR bed with their head supported by a foam head rest. A laser beam was used to align the patient vertically in the magnet such that a point on the forehead between the eyebrows was at the isocenter of the NMR machine. All imaging was carried out using the Philips

head coil of diameter 34 cm. From each patient, a single T_2 weighted image with eight subsequent echoes was acquired, the slice being oriented in either the transverse or coronal plane, and passing through the high radiation dose region of the brain. The location of the slice was carefully reproduced for each patient in subsequent NMR sessions.

Each image had a slice thickness of 3-5 mm, with a resolution of 512 x 512 pixels over a 250 x 250 mm field of view. Tuning and matching of the head coil, optimization of power attenuation and pulse length, and adjustment of the shim gradients was all performed automatically by the Philips Gyroscan operating system. Eight echoes were acquired with a spin-echo time (TE) of 50 ms, allowing T_2 calculation of normal brain tissue (T_2 = 75-120 ms) and pathological tissue ($120 < T_2 < 2000$ ms). A repetition time (TR) of 3000 ms was chosen to allow relaxation of biological ^1H nuclei, yet still acquire the spectrum within a reasonable time frame (25 minutes). From these 8-echo images, a T_2 calculated image was created; the signal intensity of each pixel in the T_2 calculated images reflecting the transverse relaxation time of the water protons in that region. An automatic scaling mechanism within the Philips software arbitrarily normalizes the pixel data values in the reconstructed image. To determine the correct T_2 values from the reconstructed data, this normalization factor must be ascertained. The computer program used to calculate this factor was written by Mr. Ravi Menon, and can be found in Appendix I. It involves loading known pixel data values (zeros and 1000s) onto the Philips operating software, and observing the pixel intensities displayed on the resultant image. Scaling factors varied from 0.18 to 0.5 between different images.

2.2.2 Image Analysis

Reconstruction of the T_2 calculated images on the Philips console showed a region of high signal intensity near the site of the original tumor, which resulted partially from the edema present. This region, which was found in all the patients imaged, was carefully analyzed for temporal changes in size or intensity.

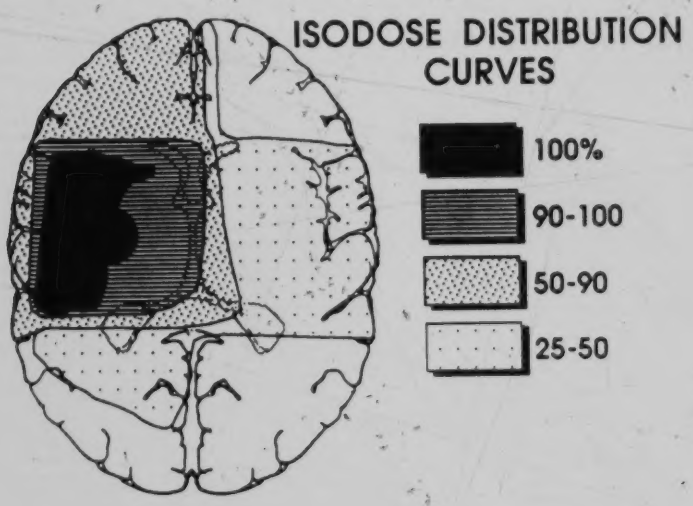

FIGURE 2.00:
ISODOSE DISTRIBUTIONS: A MAP OF THE RELATIVE RADIATION DOSES IMPARTED TO VARIOUS REGIONS OF THE CNS OF PATIENTS

During the course of radiotherapy, the radiation doses received by the head are recorded on an isodose distribution diagram. The percentage of the total dose received by the various regions of brain are as indicated.

Processing of the T_2 calculated images was carried out on the RAMTEK graphics workstation. The reconstructed image data was transferred, via magnetic tapes, from the Gyroscan unit to the RAMTEK workstation. An in-house software

program was developed, by Mrs. Ivy Ho, to analyze the NMR images. One feature of this software package allowed calculation of the signal intensity for a single pixel, a line of pixels or a group of pixels.

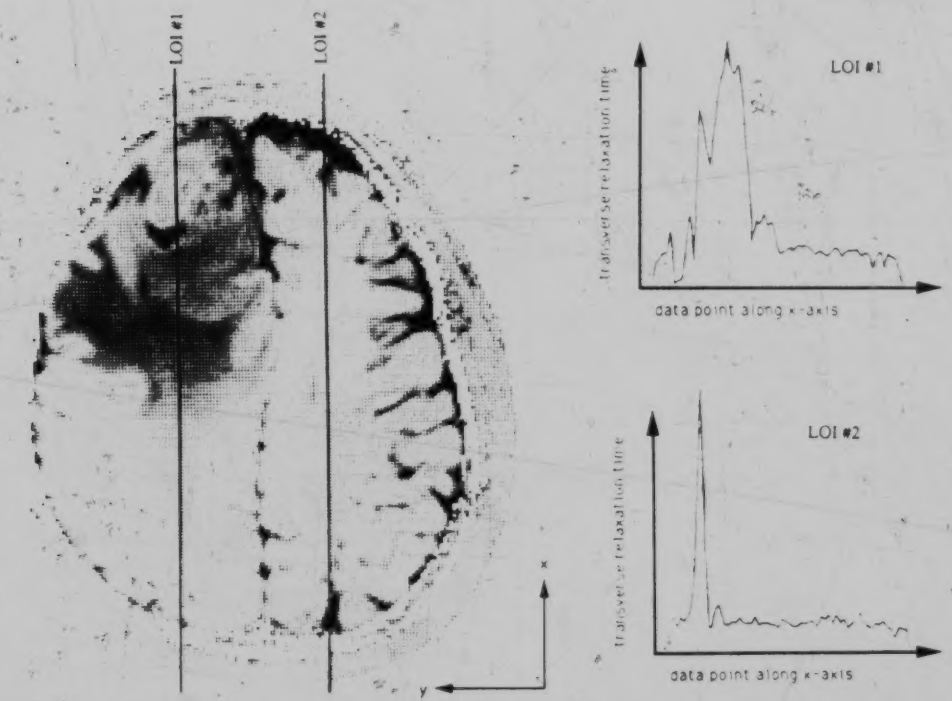

FIGURE 2.01: DETERMINATION OF TRANSVERSE RELAXATION TIMES IN BRAIN FROM T_2 CALCULATED IMAGES

T_2 profiles of brain tissue found along LOI #1 displays the contrast between normal and damaged tissue. The above image shows a post operative peritumoral lesion, which is common to all the brain tumor patients studied, in the right frontal lobe of the brain.

In the T_2 calculated images, the locations of the lines of interest (LOIs) were established, using an isodose distribution diagram as a guide (Figure 2.01). One LOI was located in the ipsilateral hemisphere of the brain, in a region that received high

doses of radiation, and was arranged such that the line passed through the peritumoral lesion. A second LOI passed through a similar anatomical region of brain, but in the contralateral hemisphere, where the brain received less than 50% of the total radiation dose. These lines of interest (Figure 2.01) were duplicated in images from subsequent NMR sessions, and the changes in T_2 intensity were recorded. The transverse relaxation times were calculated from data points found along the line of interest. Each data point represented the mean transverse relaxation time of 9 pixels (3x3), each pixel corresponding to a voxel of 0.5 x 0.5 mm in area.

FIGURE 2.02: METHOD USED IN THE DETERMINATION OF THE AREA OF THE PERITUMORAL LESION

For alterations in the size of the peritumoral lesion, a grid system was developed to facilitate calculation of the area of these regions. Each section of the grid measured exactly 1 cm^2 of the actual brain area. By superimposing the grid on T_2 weighted images, individual squares contained within the peritumoral lesion were counted. (Figure 2.02). If a grid square was only partially filled with tissue from the peritumoral lesion, it was counted as one half of a square. The final count was always rounded down to the nearest full square centimeter.

2.3 NMR Spectroscopy

During each NMR session, spectroscopy was performed on two regions of "normal" tissue in brain. One region, an area that received high radiation doses (where we expected to see some damage) and another region, an area that was exposed to lower doses of radiation. High dose regions received 80-100% of the total radiation while low dose regions received less than 50%. If possible, similar lobes of the brain were analyzed in opposite hemispheres; one contralateral (low dose) and the other ipsilateral (high dose) to the tumor.

At the beginning of this project, ^{31}P spectroscopy was utilized in attempts to observe changes in the status of the energy metabolism through relative levels of high energy phosphate metabolites and intracellular pH in brain. Analysis of this data, 8 months after beginning the study, suggested that phosphorus NMR may not provide adequate sensitivity to observe specific radiation damage. At a later stage, ^{1}H spectroscopy was used as an alternative means to observe radiation induced cerebral metabolic changes. Thus, individuals who entered this NMR study from September 1987 to November 1988 underwent ^{31}P spectroscopy, while those who joined after

December 1988 were analyzed using proton spectroscopy. Those patients who began their NMR sessions prior to the change-over date, continued to be analyzed with phosphorus, not proton, spectroscopy beyond that date.

2.3.1 Phosphorus NMR Spectroscopy

The pulse sequence used for ^{31}P spectral acquisition was a depth pulse sequence ($\theta/5$, $\theta/3$, θ, acquire). This sequence removed signal from the high flux bands that are created by the surface coil, and minimized signal from surface muscle of the scalp. The $\theta/3$ pulse is responsible for removing signal from the 270° band while the $\theta/5$ pulse removed the 450° band of the high flux signal.

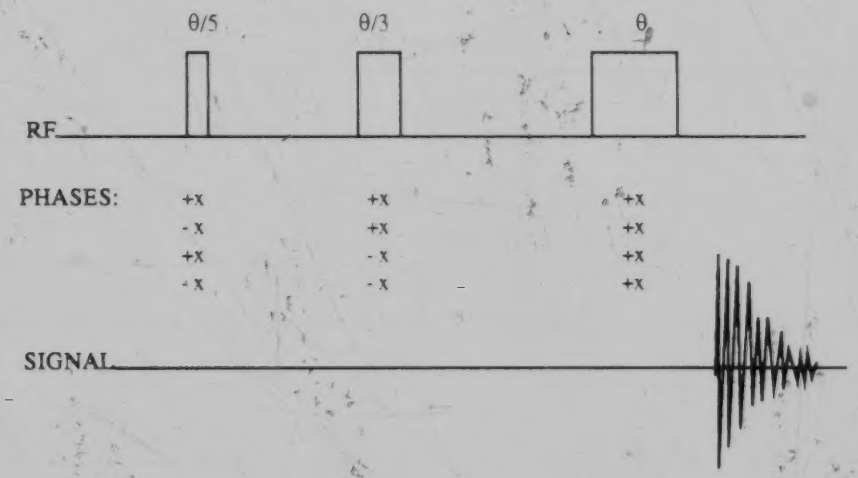

FIGURE 2.03:
DEPTH PULSE SEQUENCE USED TO ACQUIRE PHOSPHORUS SPECTRA

A series of four sequences, with phase cycling of the θ/3 and θ/5 pulses, can be used for cancellation of transverse magnetization resulting from the high flux regions. This pulse program, with the respective phase cycles, is outlined in Figure 2.03. Although additional localization, using an ISIS technique, was attempted to further remove signal from surface structures, it was found that the resultant increase in spectral acquisition time (to almost 30 minutes) was too great for patient well being.

An external standard of methylenediphosphonic acid (MDA) was included in a 1.0 molar solution enclosed in a 1.5 ml sphere. This standard sphere was placed equidistant and on the opposite side of the coil from the region of interest in the brain. The length of the depth pulse was adjusted to create a 90 degree tip angle at the MDA sphere, in order to establish the 90 degree pulse length, θ, required to collect signal from the ROI in the brain.

A special apparatus was designed to support the head of the patient, and the NMR surface coil system. This experimental setup is represented in Figure 2.04. When a patient was positioned supine in the clinical NMR system, their head could be secured in a foam head rest. An RF coil attached to the vertical arm of the a plexiglass support could be adjusted in height (along the x axis of the magnet). Rotation of the patients head allowed the coil to be placed close to any lobe of the cerebral hemispheres, ranging from the occipital to frontal regions. The distance of the MDA sphere from the coil was also adjustable. The coil system used for phosphorous spectroscopy was a concentric coil system with the outer coil of diameter 6 cm being tuned to the phosphorus resonance frequency, while the inner coil of diameter 5.5 cm is tuned for protons so that magnet shimming could be carried out using the water proton resonance.

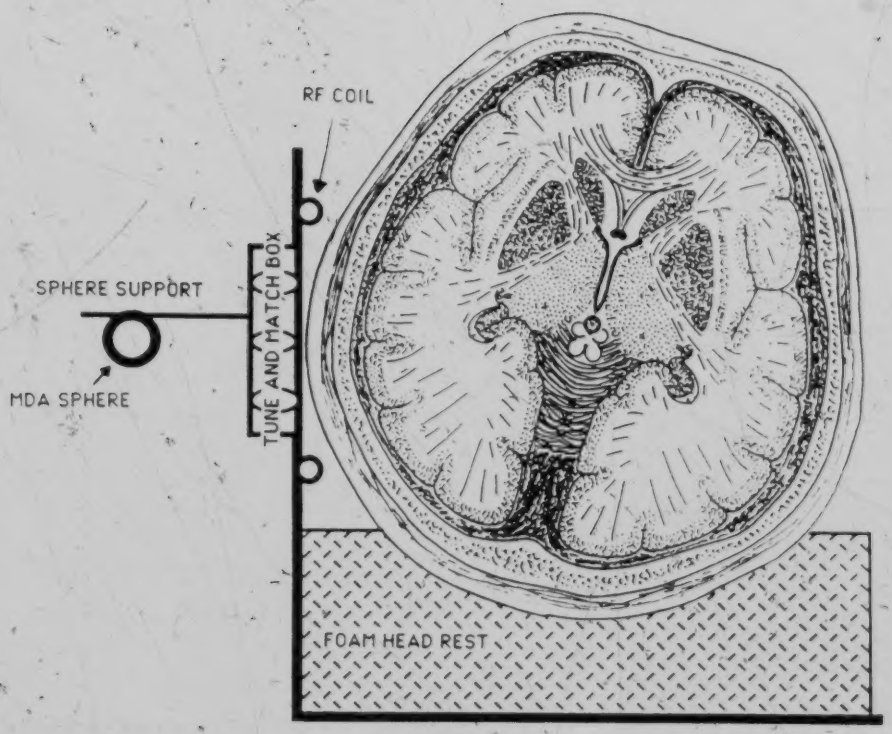

FIGURE 2.04:
EXPERIMENTAL APPARATUS USED TO ACQUIRE PHOSPHORUS SPECTRA

A profile of the proton signal distribution allowed determination of the appropriate pulse length required to provide a 90° tip angle for shimming on the ROI in brain (Figure 2.05). Water proton line widths of 0.5 - 0.3 ppm were obtained with non-localized shimming, while localization using depth pulse sequences usually resulted in line widths of 0.3 - 0.1 ppm.

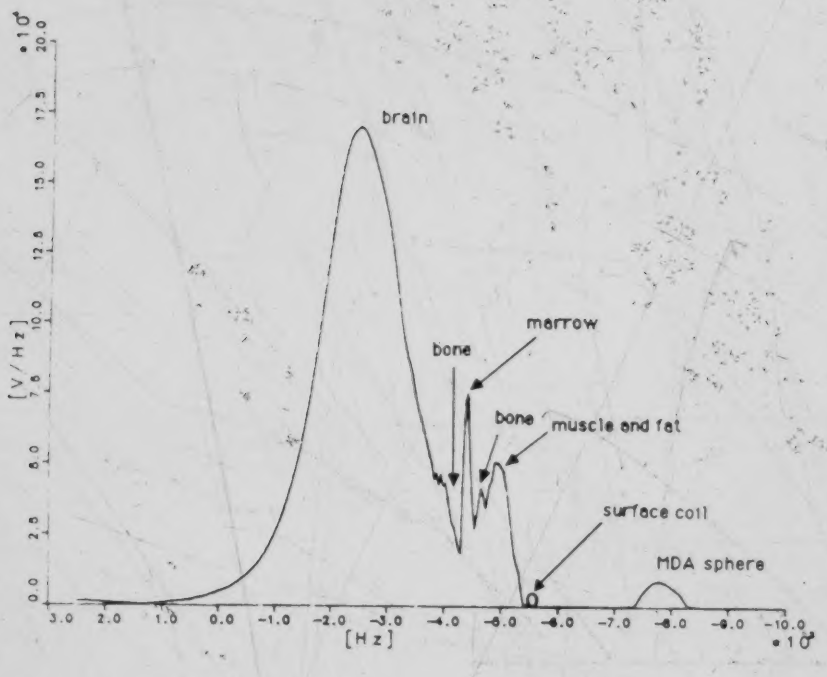

FIGURE 2.05: PROTON DENSITY DEPTH PROFILE OF A HUMAN HEAD

Observation of the proton signal distribution along the y axis (horizontal) of the human head allows determination of the pulse length required to shim on the ROI in the brain. Above is a depth pulse profile, with the 90 degree tip angle at a depth of 3 cm from the surface coil. Proton signal arising from surface structures is clearly visible.

Phosphorus nuclei resonate at 25.8576 MHz in a 1.5 Tesla magnetic field. The range of frequencies observed, the sweep width, was set to 2000 Hz in order to encompass all the phosphorus metabolites, as well as the external MDA standard. Ideally, the TR should be greater than 5 x T_1 for maximum relaxation of signal between subsequent scans, but according to this criterion, the T_1 of PCr (approximately 3 seconds) would give rise to a repetition time too long to be feasible for our purposes. We chose instead, a repetition time of 4.0 seconds, since experiments altering TR showed little changes in relative peak areas with TR $\geq$ 4 seconds (Table 2.01).

		Repetition Time				
		5 sec	4 sec	3 sec	2 sec	1 sec
Relative Peak Areas	PME	1.18	1.05	0.94	1.23	1.40
	Pi	1.30	1.50	1.15	1.23	2.29
	PDE	3.49	3.75	3.32	3.50	3.86
	PCr	2.33	2.50	2.13	1.79	2.31
	γ ATP	0.91	1.03	0.91	0.91	1.14
	α ATP	1.09	0.95	0.83	1.07	1.33
	β ATP	1.00	1.00	1.00	1.00	1.00

TABLE 2.01: RELATIVE PEAK AREAS OF PHOSPHORUS METABOLITES AT VARIOUS REPETITION TIMES

Spectra were obtained by Fourier transformation of 156 signal averaged FIDs, each FID containing 512 sets of data points. Careful positioning of the coil and imaging of coil orientation ensured that no signal from tumor would be detected. The images of coil location also proved useful for similar orientation of the surface coil in subsequent NMR sessions.

2.3.2 Proton NMR Spectroscopy

Proton spectroscopy was initiated in the latter part of this study in order to evaluate an independent measure of brain metabolism, and possibly substantiate results from the phosphorus work. Moreover, due to the slow accrual of patients

with high grade brain tumors, we extended our observations to include patients undergoing treatment for low grade astrocytomas or pituitary tumors. These observations required the spectral interrogation of regions deep in the brain, especially in the case of the pituitary tumors. In consideration of this, we chose to utilize STEAM (stimulated echo acquisition mode), a spectroscopic technique which was capable of localization, using B_0 gradients, to observe brain tissue in the deeper regions.

STEAM was implemented on our NMR machine by Dr. Chen Thomas, but certain program optimizations were required before acceptable spectra could be obtained from our patients. These optimizations included adjustment of the spoiler gradients to maximize removal of transverse magnetization from outside the ROI, removal of a time shift in the FID, and increasing the water suppression to allow visualization of metabolites found 1 ppm or more from the center of the water resonance. An aqueous phantom containing 2.5 mM choline, 12.5 mM creatine, 5 mM NAA, 12.5 mM lactate and 0.5 mM sodium azide was used when optimizing STEAM.

The STEAM sequence contains three selective 90° pulses, each along a different orthogonal plane, to excite spins in the volume of interest, while dephasing gradients remove signal from outside the ROI. The first set of dephasing gradients cause transverse signal to dephase across the volume of the ROI. A second set of dephasing gradients, identical in strength and duration to the first, have a similar effect, but in the ROI, this allows refocussing of the previously dephased signal. A Dante pulse at the beginning of the sequence can create a 90° tip angle over a very narrow (80 - 100 Hz) band width centered over the water peak. The resultant transverse magnetization from the water resonance can then be dephased using

spoiler gradients. A selective inversion pulse, created by a hyperbolic secant, is also found near the beginning of the pulse program. This can be used to excite a narrow frequency band centered over the metabolites, inverting the metabolites, but not the water, thus allowing further suppression of the water resonance. This sequence incorporates phase cycling of the 90° pulses to ensure maximum cancellation of pulse errors, while cycling of the receiver prevents realization of the constant voltage offset generated by the electronics of the system. All the pulse lengths required for the STEAM sequence are calculated automatically by the Gyroscan software.

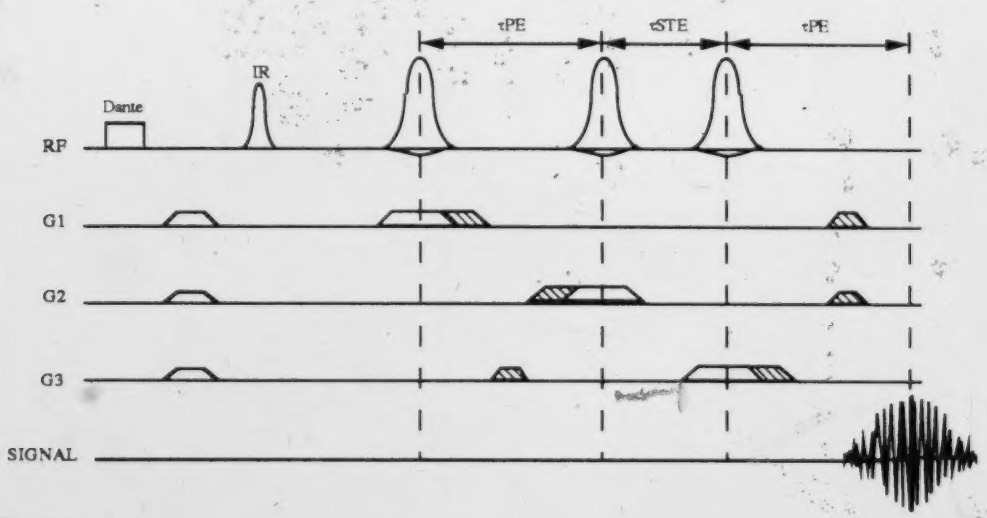

FIGURE 2.06: THE STEAM PULSE SEQUENCE

Our variation of the STEAM pulse sequence used to collect the proton spectroscopy data is a modification of the sequence proposed by Heindel *et al* (48). The adjustable spoiler gradients are marked with hatching.

In order to acquire our spectra, subjects were asked to lie supine on the NMR bed, and were vertically centered in the magnet at the level of their brain tumor. The

Philips head coil was used to take 3 - 5 transverse image slices of the brain with a field of view of 250 x 250 mm. These orientation images then allowed computerized orientation of a 30 x 30 x 30 mm cube of interest within the brain. Prior CT or NMR images, as well as the aid of the attending physician, were used to ensure that the ROI did not include any tumorous tissue.

The head coil, used as both the RF transmitter and receiver, was used to carry out the proton spectroscopy. Tuning and matching of the head coil, calculation of the power attenuation and determination of the pulse length required for spectroscopy, was all performed automatically by the Gyroscan operating system prior to acquisition of the orientation images. In our experiments, a spin echo time of 136 ms (τPE = 68 ms) was used for two reasons. First, it minimized eddy current effects, and second, it simplified the proton spectrum of brain by avoiding the detection of resonances from metabolites with short relaxation times. The short τSTE (40 ms) minimized longitudinal relaxation during this time. The repetition time was 3.0 seconds to allow for relaxation of metabolites, without prolonging the time required for the acquisition of the spectra.

A "water spectrum" was acquired from the CNS of many patients to determine the peak area of the water resonance, for use as an internal concentration standard. In this case, the band width of the inversion recovery pulse was 200 Hz, and it was centered directly on the water peak (at 0 Hz). This allowed appropriate inversion of the water peak to correspond with the phases of the receiver. Although the Dante pulse remained engaged, the pulse length was minimized (1% of the calculated 180° pulse length) to effectively remove the water suppressive effect of the Dante. A total of 16 FIDs were signal averaged, and Fourier transformed, to obtain a water spectrum.

For acquisition of the "metabolite spectra", in which the water is suppressed sufficiently to allow detection of the metabolite peaks, the STEAM sequence was modified somewhat. The inversion recovery pulse was again 200 Hz in width, but it was centered at 150 Hz down field from the water resonance. All the metabolites that we were interested in seeing were included in this narrow frequency band, and were equally inverted by the IR pulse. The pulse length of the Dante was set to 60% of the calculated 180° pulse length, which proved most efficient at bringing the water signal into the transverse plane. Metabolite spectra were obtained by Fourier transformation of 128 signal averaged FIDs, each FID containing 512 sets of data points. The metabolites were inverted every second scan, and the receiver phase was adjusted accordingly, so that signal from the metabolites was additive, while the water signal subtracted itself. Phase cycling of all the peaks involved resulted in 16 scans being required to acquire the desired signal.

Metabolite peaks were sometimes obliterated by one of two larger peaks: water or fat. Due to the absence of adipose tissue in brain, the associated broad lipid resonance should not be visible in brain spectra. If a lipid signal was noted, relocation of the ROI to a more proximal location resulted in disappearance of the signal, suggesting that the lipid resonance was due to surface fat. Metabolites close to the water peak were sometimes hidden under the wings of the water resonance. This problem was minimized by maximizing the magnetic homogeneity in the ROI through shimming. Localized shimming, using STEAM, resulted in a peak width at half height of the water resonance ranging from 5 - 11 Hz. Anything greater resulted in poor water suppression and unacceptable resolution of metabolite peaks.

2.3.3 Spectral Analysis

Raw time domain data was transferred from the clinical unit to the RAMTEK workstation via portable magnetic tapes. All NMR spectra were processed on the RAMTEK graphics display unit utilizing in-house software programmes developed by Dr. Carey Gibson and Mrs. Ivy Ho.

In the case of the phosphorus spectrum, an exponential multiplication function, with a line broadening of 5 Hz, was applied to the FID to smooth out the data points, without significantly reducing the spectral resolution. The spectrum was then Fourier transformed to produce a frequency spectrum (Figure 2.07).

FIGURE 2.07: AN EXAMPLE OF FOURIER TRANSFORMED TIME DOMAIN DATA FROM THE ^{31}P FID

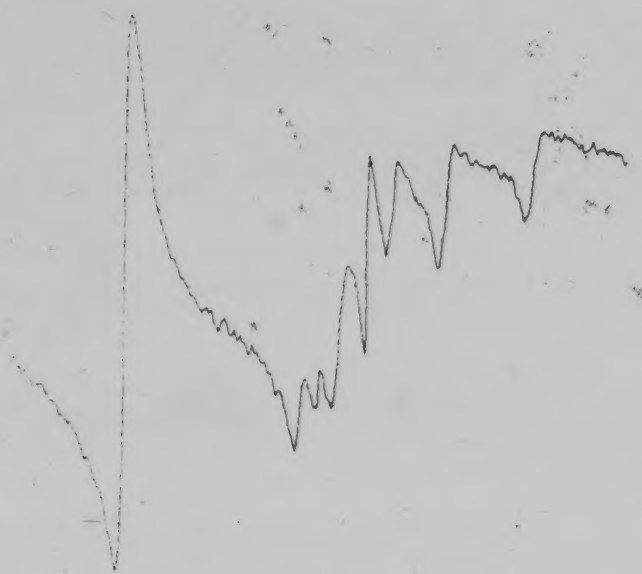

Phasing of the spectrum was achieved by, first, utilizing a zeroth order phase correction to phase the left hand peak, then, applying a first order phase correction centered on the left hand peak, to phase the other resonances. The resultant spectrum has seven identifiable metabolite peaks superimposed on a baseline with a broad hump (Figure 2.08).

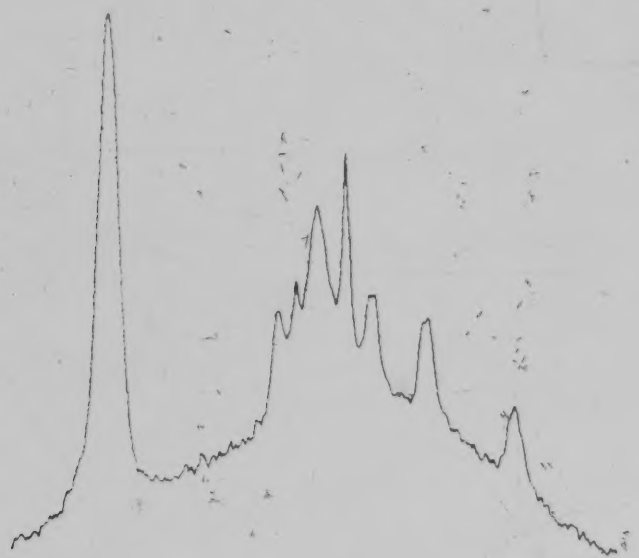

FIGURE 2.08: AN EXAMPLE OF A WELL-PHASED ^{31}P SPECTRUM

Removal of the baseline hump was accomplished through generation of a smooth baseline curve which was then subtracted from the spectrum. Being an interactive rather than an automated process, baseline correction is difficult to duplicate precisely, even when reprocessing the same raw data. Following baseline correction, the phosphorus spectrum is fully processed (Figure 2.09).

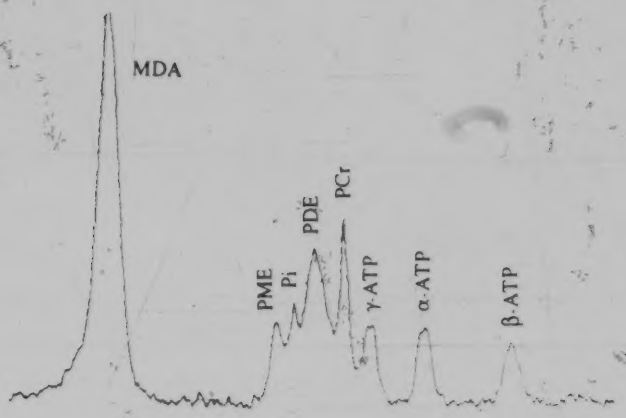

FIGURE 2.09: AN EXAMPLE OF A FULLY PROCESSED ^{31}P SPECTRUM

Proton spectra present several unique problems, which must be corrected for during the processing of the spectra. Following application of an exponential multiplication (line broadening = 2 Hz) to the FID, the data is Fourier transformed. The resultant frequency spectrum (Figure 2.10) is dominated by signal from the water resonance, which is never completely removed by water suppression techniques.

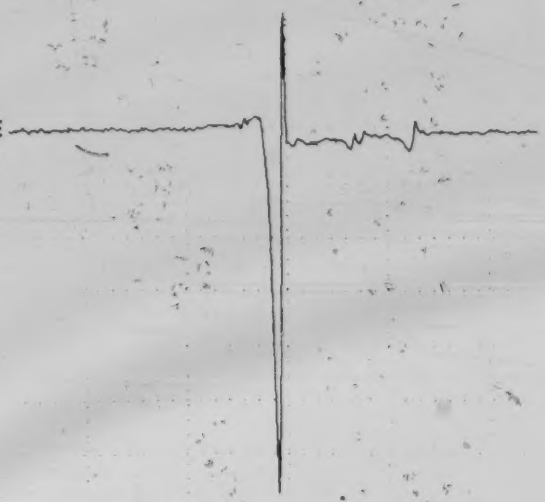

FIGURE 2.10: AN EXAMPLE OF FOURIER TRANSFORMED TIME DOMAIN DATA FROM THE ^{1}H FID

Signal from the water peak was excluded from the spectrum by reducing the frequency window. Three metabolite peaks could then be observed above the background noise. These peaks can usually be phased using a simple zeroth order phase correction. (Figure 2.11)

FIGURE 2.11: AN EXAMPLE OF WELL PHASED METABOLITE PEAKS FROM A ^1H SPECTRUM

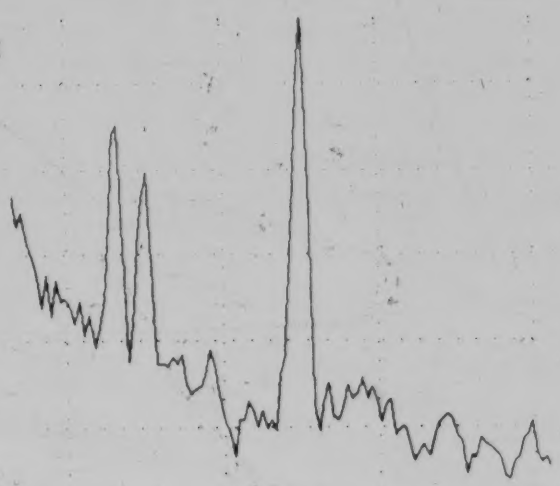

The metabolite peaks of the proton spectrum are superimposed on the wings of the water resonance (Figure 2.12). In order to flatten the baseline, a smooth baseline curve was constructed just beneath the actual baseline, and this was subtracted from the original spectrum.

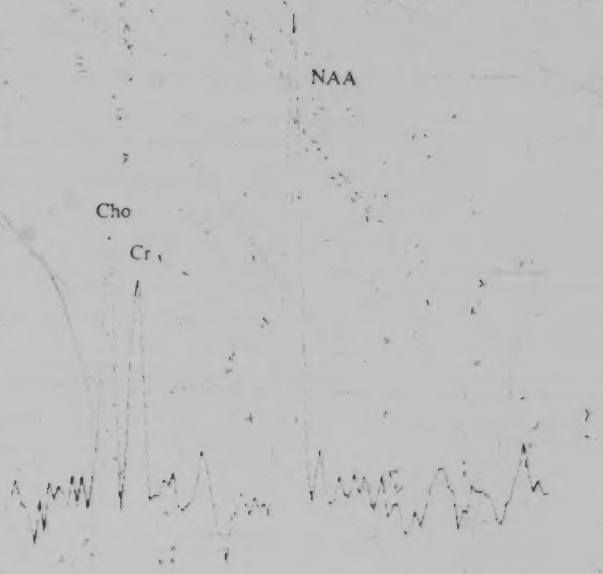

FIGURE 2.12: AN EXAMPLE OF A FULLY PROCESSED ^{1}H SPECTRUM

The processed spectrum, both in ^{31}P and ^{1}H spectroscopy, had several identifiable peaks set on a flat baseline. Estimation of the area under the peaks is important to establish relative concentrations of the corresponding NMR-visible metabolites. Area estimation can be achieved by fitting the NMR peaks to Lorentzian or Gaussian shapes. In the phosphorus spectrum, the PCr and Pi peaks were fitted using Lorentzian curves, but all other ^{31}P metabolite peaks were fitted best by Gaussian curves. Metabolite peaks visible in the proton spectrum were best fitted with Gaussian curves, while the water resonance was best fitted with a Lorentzian.

Lorentzian curves follow the equation:

$$y(f) = \frac{ad}{[d^2+(f-f_o)^2]\pi} \qquad (20)$$

Gaussian curves are represented by the equation:

$$y(f) = \frac{a}{d\sqrt{2\pi}} \exp\left[-(f - f_o)^2 / 2d^2 \right] \qquad (21)$$

Where **y(f)** is the amplitude at any given frequency, **f**. The area under the curve, **a**, the center frequency of the curve, **fo**, and the damping frequency, **d**, are all adjustable variables of the curves. These three variables were altered by a SIMPLEX optimization routine which minimized the residual error, and hence determined the best fit. Subtraction of the fitted curves from the original spectrum of peaks yielded the error, and iterations were continued until the residual error had stabilized at a minimum.

CHAPTER 3: RESULTS AND DISCUSSION

Previous *in vivo* NMR spectroscopy studies of CNS radiation damage have centered on single dose irradiation of animal brains (43,63,96). However, the animal model studies that use single dose irradiation are not likely to reflect accurately the damage caused to human brain by the fractionated doses received during radiotherapy. It is a well established fact, that in bacterial and tissue cell cultures, the surviving fraction of cells following single doses of radiation is lower that the surviving fraction of cells subjected to fractionated radiation of the same total dose.

The purpose of our study was to observe the changes, detectable by NMR, that occur in human brain following radiotherapy. Three aspects of NMR were utilized to investigate brain irradiation effects, namely phosphorus (^{31}P) spectroscopy, proton (^{1}H) spectroscopy and proton imaging. The application of these techniques to monitor brain tissue in humans non-invasively, allowed actual clinical data to be established, hence removing the degree of uncertainty found in data from animal model studies. These results may serve as a reference for future treatment planning of patients undergoing cranial radiotherapy.

3.1 Phosphorus Spectroscopy

^{31}P NMR spectroscopy is a popular tool for the investigation of brain biochemistry *in vivo*. It offers a relatively simple quantification of brain energy metabolism by measuring the relative concentrations of adenosine triphosphate

(ATP), phosphocreatine (PCr) and inorganic phosphate (Pi). Phosphorus spectroscopy is also able to measure the pH of brain.

3.1.1 General Considerations

Our *in vivo* spectra of human brain at 1.5 tesla allowed the resolution of seven distinguishable peaks. Five of the peaks (γATP, Pi, PCr, PME and PDE) could not be resolved down to the baseline, and a calculation of the areas under these peaks required the utilization of curve-fitting techniques.

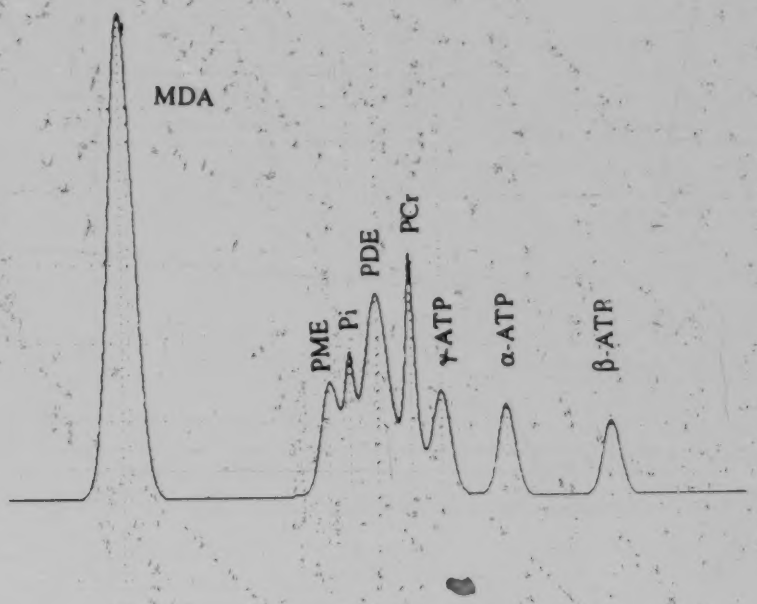

FIGURE 3.00:
AN EXAMPLE OF A 'FITTED' ^{31}P SPECTRUM OF HEALTHY HUMAN BRAIN

Although single resonance lines in liquids are normally Lorentzian in shape, many of the peaks in our spectra are composed of several resonances (Table 1.01). Bearing in mind also, the heterogeneity of the sample, we explored the possibility of fitting the broader peaks with Gaussian curves. Only the Pi and PCr peaks were fitted with Lorentzian curves. The initial curve fitting was optimized, using the SIMPLEX routine to minimize residual error between the resonance line shapes and the Lorentzian or Gaussian curves. The resultant 'fitted spectrum' (Figure 3.00) was then used for further analysis.

Among the healthy volunteers, a considerable variation was detected in the ratio of several metabolite peak areas relative to that of ATP (Table 3.00). All metabolite ratios display standard deviations of approximately ± 20%, with the exception of PCr, which has less than a 15% deviation. Although the greatest variations are observed when comparing data from several different volunteers, there is still a significant variation in peak area ratios (14 -21 %) found within each individual. Individual variation represents the standard deviation found in each of two volunteers that underwent several NMR scans from different regions of brain, and over a prolonged period of time. For each volunteer, data from all their scans was compared, and the resultant two standard deviastions were averaged. Similarily, standard deviations from each of four different NMR sessions were averaged to determine the variation among different regions of the brain, in a single individual. This spatial variation compares different hemispheres and different lobes of the brain, but all data is collected within a single NMR session, to remove temporal effects. Changes, with time, in the metabolite ratios from a single region of brain, are represented by temporal variation. The differences in metabolite concentrations between different regions of the brain (spatial variation) and changes in the metabolite

concentrations over time (temporal variation) are also substantial (8-19 %). A similar clinical study of the normal variation in brain metabolites, as observed by ^{31}P spectroscopy, shows total variations of up to 30% in healthy volunteers (105). ^{31}P studies on human prostate also show large variability in metabolite ratios. For example, PME/ATP ratios differ by ± 20% while the PCr/ATP ratios vary ± 25% (109).

NMR peak ratios	mean peak area ratio	total variation	individual variation	spatial variation	temporal variation	processing variation
PME/ATP	0.313	18.7 %	16.2 %	13.5 %	7.9 %	7.0%
Pi/ATP	0.438	20.5 %	21.1 %	18.9 %	16.7 %	12.8%
PDE/ATP	1.060	17.6 %	16.9 %	16.5 %	11.0 %	4.9%
PCr/ATP	0.706	13.0 %	13.8 %	13.0 %	13.1 %	4.5%
n		28	10	3	4	12

TABLE 3.00:
NORMAL VARIATIONS IN BRAIN METABOLITE CONCENTRATIONS

Variations in peak areas are represented by the percent standard deviation from the mean. The number (n) of NMR spectra that were pooled to calculate each of the variations is also recorded.

A significant portion of the variation observed in the peak area ratios of brain metabolites probably arises from the processing of NMR spectra. For example, if the same spectral file is analyzed several times using the procedure described in Chapter 2, discrepencies of up to ±12% are observed between the successive estimates of

peak area. Three possible sources for manual error exist in the processing technique: phasing, baseline correction and peak area estimation.

With phasing, there seems to be little manual error. For example, the Fourier transformed data from one spectrum was phased several times, but values for zeroth and first order phasing varied by less than 3% between successive phasing attempts. The potential for manual error in the baseline correction is somewhat more difficult to quantify. By processing a spectrum several times, changing only the baseline correction, the final peak areas were compared to estimate the subsequent effects of deviations in baseline corrections. The standard deviation in the peak areas ranged from 12% for the γATP peak to less than 2% for the total ATP peaks (Table 3.01). Finally, initial estimations of peak area, through interactive fitting of the resonanaces to Gaussian or Lorentzian curves, will affect the final fit estimated by the SIMPLEX routine. Quantification of this error is acheived through the multiple processing of the same raw data file, changing only the initial peak area estimates. In this case, the Pi peak area showed the greatest variability, with a standard deviation of ±12.6% (Table 3.01). The total ATP peak area again displayed the least variability (±0.9%).

The lack of reproducability in peak areas due to these three interactive processing procedures can therefore cause substantial variation in area ratios of metabolite/ATP peaks. One might therefore conclude that much of the "normal variation" found in our ^{31}P spectra from healthy volunteers is due to uncertainty arising from the spectral processing. However, much of the lack of processing reproducibility may, in turn, be due to measuremant uncertainty. Processing reproducibility is a strong function of the initial signal-to-noise ratio (S/N) of the spectrum. The S/N in the ^{31}P brain spectra was approximately 10:1 for the majority of peaks, although the PCr and PDE peaks had a greater S/N (20:1). Therefore, if the

signal to noise ratio is considered the determinant of measurement uncertainty, then the peak areas calculated from the spectra are only accurate to ± 5% (± 2.5% for PCr and PDE).

NMR peaks	total error	baseline error	error of estimation
PME	6.3 %	4.5 %	4.9 %
Pi	11.9 %	5.7 %	12.6 %
PDE	4.7 %	4.6 %	3.5 %
PCr	4.4 %	5.7 %	1.3 %
γATP	10.0 %	11.7 %	3.1 %
αATP	4.4 %	2.9 %	1.3 %
βATP	5.4 %	6.2 %	2.6 %
total ATP	2.1 %	1.7 %	0.9 %
pH	0.6 %	0.3 %	0.5 %

TABLE 3.01: PROCESSING REPRODUCIBILITY IN THE CALCULATION OF ^{31}P METABOLITE PEAK AREA RATIOS AND pH

The spread of 0.10 pH units that is observed in the pH of brain from our healthy volunteers may also be due mainly to spectral processing and measurement uncertainty. For example, the chemical shift between PCr and Pi, in ppm, varied from 4.79 - 5.02 when a single raw data file was processed several times. A chemical shift spread of this magnitude resulted in a standard deviation of ±0.04 in the corresponding pH values, which accounted for almost all the "normal variation" observed in the healthy volunteers.

The normal brain pH values recorded in our study (7.12 ± .05) agree well with the values established by other clinical investigators (82,86,90). Mammalian pH values determined from healthy brain in previous NMR studies varied from 7.00±.06 (105) to 7.48±.03 (117). The large variability between the NMR measured pH values suggest a lack of consistency between laboratories, in the methods used to calculate the pH.

TABLE 3.02: METABOLITE/MDA PEAK AREA RATIOS AS ESTABLISHED FROM PHOSPHORUS SPECTRA OF HEALTHY BRAINS

The MDA standard was included in 8 of 28 31-P spectra from the healthy brains of volunteers. Metabolite/MDA peak area ratios were determined for each of these 8 volunteers, and the means are recorded in this table. Standard deviations (SD) arise from the individual variations from the mean, and are expressed as a percentage of the mean.

NMR PEAK	Mean Ratio ± SD
PME	.166 ±19%
Pi	.179 ±17%
PDE	.445 ±18%
PCr	.280 ±10%
γ ATP	.114 ±18%
α ATP	.140 ±15%
β ATP	.100 ±17%
α+β+γ ATP	.367 ±14%
α + β ATP	.232 ±17%

Although an external standard of methylene diphosphonic acid (MDA) was included in many of the spectra, data collected during their first nine months of this study had no standard included. For these early spectra, it was necessary to try and utilize the NMR peak of one of the brain metabolites as a possible internal

concentration standard. Since alterations in PCr and Pi concentrations are expected to preceed changes in the levels of ATP in damaged cells, the use of the total area under ATP as an internal standard was thought to be our best chance of providing a stable marker for observing changes in the other metabolites. In healthy volunteers, the ATP/MDA area ratio displayed only 14% standard deviation (Table 3.02). Although the βATP peak is often used as an internal concentration standard in other NMR studies, in our experiments, processing reproducibility of the total area under all three ATP peaks displayed less than half the variability of the area under the βATP peak alone. Also, the total area of all the ATP peaks displayed a greater consistency with the area of the MDA peak .

3.1.2 ^{31}P NMR Data from Patients

Thirteen patients entered the ^{31}P spectroscopy study, and 5 survived more than one year following the end of radiation therapy (Table 3.03).

NMR session	pre RT	post RT	2 month	4 month	8 month	12 month
# patients	13	13	11	9	5	5

TABLE 3.03:
NUMBER OF PATIENTS ANALYZED WITH PHOSPHORUS SPECTROSCOPY

Since the mean survival time for patients with malignant gliomas is 9 months from the time of diagnosis (8), poor patient survival should have been expected. Tumor recurrence was the most common pathology in the patients that dropped out of the ^{31}P study. Most patients analyzed had malignant gliomas, and were treated with 6000-8000 cGy of radiation in fractionated doses of less than 200 cGy per fraction. Appendix III outlines the tumor diagnosis, and the radiotherapy undergone by each patient.

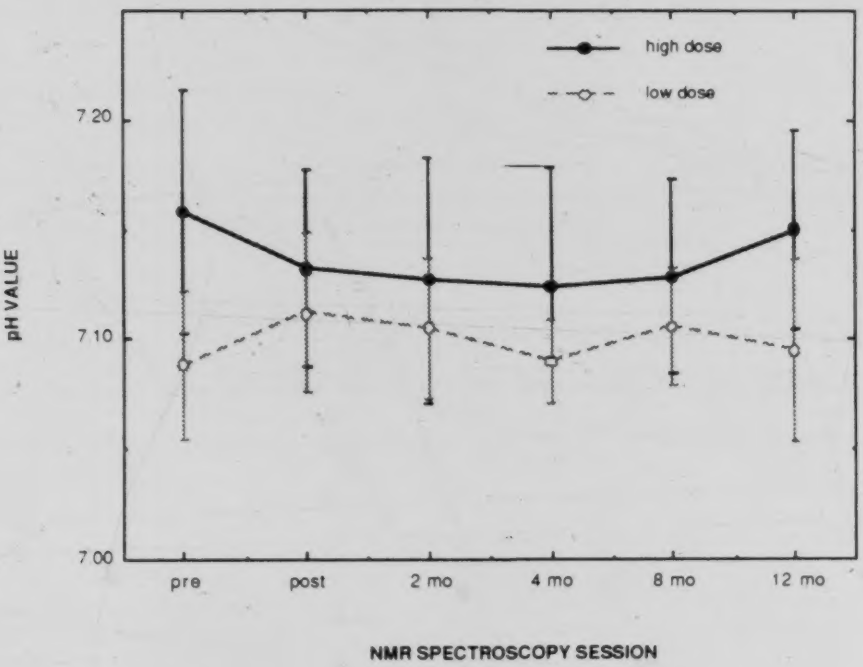

FIGURE 3.01: TEMPORAL VARIATIONS IN THE pH OF THE CNS IN BRAIN TUMOR PATIENTS

The NMR peak area ratios of brain phosphorus metabolites are plotted in Figure 3.01. Mean metabolite ratios and were determined for each NMR session, allowing observation of temporal changes in metabolite levels between cerebral tissue irradiated with either high or low doses of x-rays. The mean pH of brain from the low dose region is 7.10 ± .03, while the high dose region displays a slightly higher mean pH (7.14 ± .05). Statistical analyses of pH values (ANOVA) gave rise to the conclusion that there were no significant temporal changes in pH, and neither hemisphere displayed a significantly higher or lower pH values than that of healthy volunteers (mean pH = 7.12 ± .05). This suggests that radiotherapy did not alter the pH of brain tissue beyond the limits of normal variability. In spite of this, the pH data did show one difference, namely, the pH of the high dose region remained consistently elevated above that of the low dose region. However, this pH difference was only statistically significant ($p<0.05$) in the pre RT data.

The relative alkalinity associated with the high dose region of brain prior to RT (Figure 3.01) is likely due to surgical trauma. Blood plasma, having a pH of approximately 7.4, will cause a temporary increase in the pH of the extracellular fluid as the plasma leaks, from severed capillaries, into the interstitial spaces in the brain. Since the chemical shift of the Pi peak is influenced by inorganic phosphate in both intracellular and extracellular environments, an increase in the extracellular pH will effect the overall pH observed. Several months may be required for the brain to clear the residual blood from its interstitial spaces, accounting for the consistently elevated pH levels in the high dose region. Error bars in Figure 3.01 represent the standard deviation in brain pH that is observed among the different patients, and the shaded region represents the range of pH values observed among the brains of healthy volunteers.

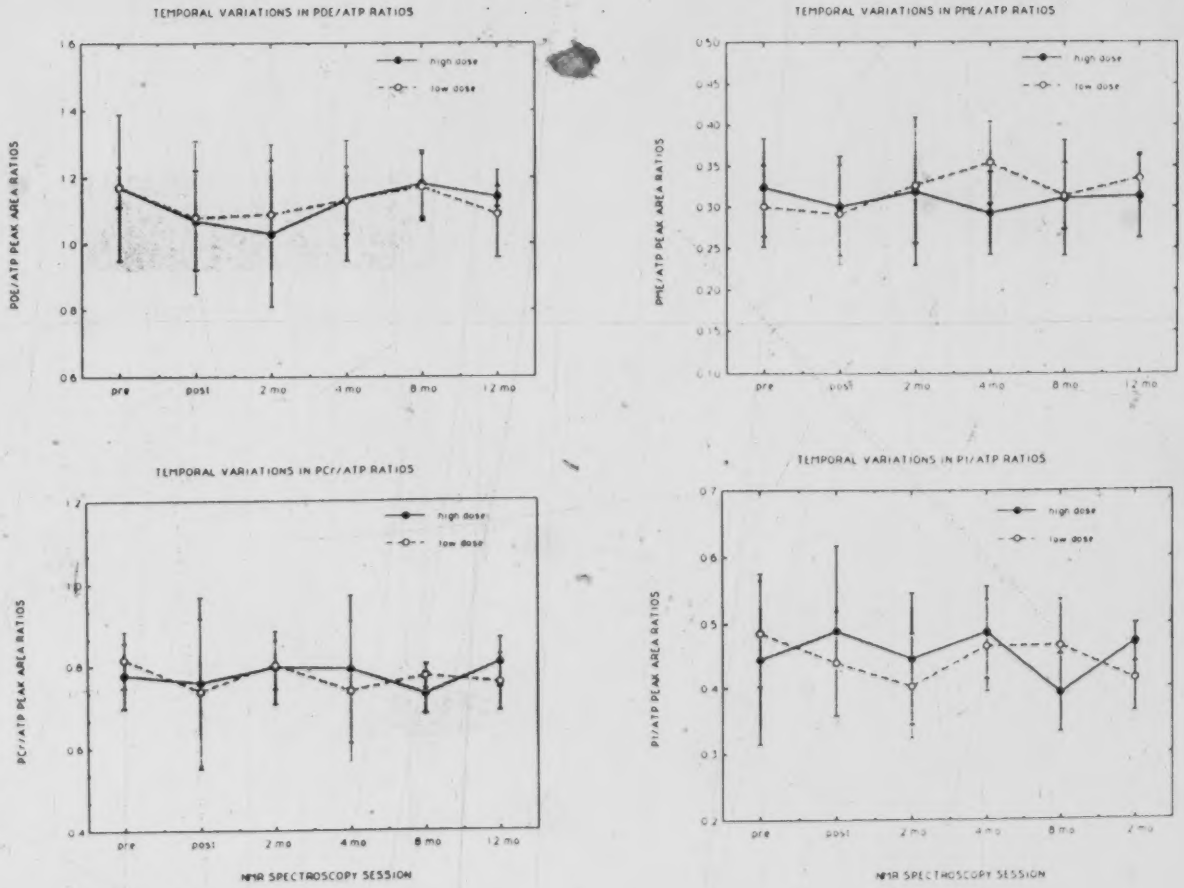

FIGURE 3.02:
TEMPORAL VARIATIONS IN ^{31}P METABOLITE PEAK AREA RATIOS IN THE CNS OF BRAIN TUMOR PATIENTS

The mean peak area ratios ±SD are plotted for regions of brain receiving high doses and low doses of radiation. Shaded areas on the graph refer to the normal range of values found in the brains of our healthy volunteers.

Statistical analysis of variance (ANOVA) of the ^{31}P data confirmed there were no significant changes in Pi/ATP or PME/ATP ratios between hemispheres, between normal and irradiated brain, or with time following radiotherapy. Although there was a statistically significant ($p<0.05$) increase in PCr/ATP and PDE/ATP ratios over those of healthy volunteers, these ratios did not change significantly following radiotherapy. These elevated metabolite ratios were apparent prior to radiotherapy, and persisted throughout the time span of this study. Some factor common to patients, but not to the volunteers, that was present prior to radiotherapy must have been the cause of elevated metabolite ratios. This common factor must have a global effect on the brain, since both hemispheres display the high metabolite levels.

Residual tumor found in the ipsilateral hemisphere often infiltrates surrounding normal tissue, but glioblastomas typically exibit a low PCr/ATP ratio, therefore this could not account for the higher ratios that we observed in the patients. All patients analyzed by ^{31}P spectroscopy underwent brain surgery for subtotal removal of the tumor. The trauma associated with such surgery might have temporarily affected metabolism of brain cells, through breakdown of the blood brain barrier, although one might expect these effects to be local, and to lessen with time following surgery. All patients were also on medication in order to reduce cerebral effects induced by the tumor, surgery, and radiotherapy. Appendix II lists the medications taken by each patient. We could find no literature on the immediate or residual effects of the medications on the ^{31}P spectrum of brain, and our study suggests that there is no correlation between any particular drug and the elevated PCr/ATP or PDE/ATP ratios.

Finally, when comparing data from patients with that from healthy volunteers, one must consider the age difference between the two groups; the mean age of the

volunteers was 26, while the mean age of the patients was 37. Attempts to age match volunteers and patients met with little success due to the lack of older volunteers willing to become involved in our study. Little data is available on the effect that aging has on phosphorus compounds in brain, although gerontological studies on human muscle may yield clues to biochemical changes in brain. In skeletal muscle of older volunteers, increased PDE levels have been observed (76,100). These changes were initially thought to be associated with decreased levels of type II muscle fibres, although more recent clinical studies have shown that the biochemical changes preceded the alterations in cell type (100). Studies in aged rat brains have displayed increased methylation of phosphodiesters, suggesting that altered phospholipid metabolism may occur with age (14). Studies on human gastrocnemius muscle have also shown an increase in the (Pi + PCr) / ATP ratio with age (100).

Aging might therefore account for the elevated metabolite ratios that we noted in the brains of patients compared to the brains of the healthy volunteers. The increase in the PDE/ATP and PCr/ATP ratios are likely due to a combined decrease in ATP levels and increase in concentrations of PDE and PCr. Although no evidence in the literature was found to support the increased PCr levels, the relatively unchanged Pi/ATP and PME/ATP ratios between healthy volunteers and the patients, suggests that decreased ATP levels alone may not be sufficient to cause metabolite ratios from the patients to extend beyond the range of normal variation established by our healthy volunteers.

When we initiated this study, we expected to see increased levels of Pi and decreased levels of PCr in brain cells following radiotherapy. Previous ^{31}P spectroscopy work on brains that had been stressed energetically through ischemia or hypoxia, suggested that Pi and PCr would be the most sensitive to changes in the

energy status of the cell (53,62,79,86,92). This sensitivity was expected to result from a combination of two factors. First, during times of energy stress, when ATP utilization exceeds ATP production, PCr acts a buffer for ATP by contributing high energy phosphates to ADP. Such a mechanism would serve to maintain the levels of ATP, at the expense of PCr. Second, ATP utilization releases low energy inorganic phosphates in the cytoplasm of the cell. If energy metabolism is in any way impaired, Pi cannot be utilized to form ATP again, and the inorganic phosphate will temporarily accumulate in the cell. The high energy phosphates observed in ^{31}P spectroscopy should, therefore, reflect any alterations in energy metabolism of the brain cells following irradiation.

One hypothesis, regarding changes in the CNS following radiotherapy, involves damage to the rapidly dividing endothelial cells of the vasculature (112). If this is the case, one might expect that the gradual degradation of the vasculature would result in the development of ischemia and hypoxia in regions of the irradiated brain. Even mild ischemia affects the concentrations of PCr and Pi in brain (62). Therefore, vascular damage should be reflected as compromised energy metabolism in brain. From our results, we are unable to detect such damage. No observable decrease in PCr or increase in Pi levels could be detected when comparing NMR spectra of brain prior to and following radiotherapy (Figure 3.02). Possible reasons for this finding are listed below.

i) The damage to vasculature develops extremely slowly so that it is not fully realized, even one year following RT.

ii) The damage to vasculature is such that it cannot be detected due to the variability of our ^{31}P NMR spectroscopy.

iii) No damage to the vasculature occurs at all.

Another hypothesis of radiation changes in the CNS involves direct damage to the neuroglia (112). The integrity of the cell can be compromised by a combination of damage to the DNA and to the membrane. The former is not usually realized until the division of cells occurs, and will rarely become evident in non-dividing cell populations such as those in brain. Membrane damage, however, may be detected by ^{31}P NMR through increases in the concentration of phosphomonoesters (PME) and phosphodiesters (PDE) in the cell cytoplasm. For instance, mobile PME and PDE compounds can be produced by the breakdown of membrane lipids, resulting in increased cytoplasmic concentrations. In addition, high concentrations of lipid precursors, which are also mobile PME and PDE compounds, may be produced to repair the damaged membranes. No observable changes in either of these two NMR peaks were detected in patient brain following radiotherapy (Figure 3.02), although membrane disruptions, undetectable by phosphorus spectroscopy, might be occurring.

3.1.3 Data from Long Term Survivors of Brain Tumors

In order to test the hypothesis that delayed radiation damage may be detectable by ^{31}P spectroscopy only after long periods of time, another small group of volunteers was studied. Each of these individuals had undergone radiation treatment for brain tumors several years earlier, and had survived without recurrence. Four long term survivors were evaluated; two females and two males. The females each received a total of 5500 cGy of radiation in daily fractions. (188 cGy/fraction). One female was treated for a high grade mixed glioma, while the second had a low grade astrocytoma. Each of the two males had a high grade astrocytoma that had been

treated with a total dose of 6000 cGy delivered with a hyperfractionation schedule (89 cGy/fraction, 3 fractions/day). These long term survivors underwent a single ^{31}P NMR spectroscopy session, with spectra being acquired from two regions of the brain, namely, one that had received a high dose of radiation, and another that had received a lower dose. The results of the NMR scans of these volunteers are summarized in Table 3.04.

	long term survivor	Age	Time elapsed since RT	NMR Peak areas relative to ATP				pH
				PME	Pi	PDE	PCr	
IPSILATERAL HEMISPHERE	D Wi	39	9 years	.426	.550	1.44	.797	7.12
	S C	45	5 years	.365	.462	1.45	.726	7.11
	R W	54	7 years	.339	.351	1.20	.733	7.14
	D Wa	58	8 years	.296	.530	1.16	.794	7.04
	average	49	7.3 years	.357±.05	.473±.09	1.31±.15	.763±.04	7.10±.04
CONTRALATERAL HEMISPHERE	D Wi	39	9 years	.302	.654	1.25	.798	7.12
	S C	45	5 years	.327	.523	1.20	.646	7.17
	R W	54	7 years	.324	.365	1.37	.907	7.14
	D Wa	58	8 years	.275	.613	1.24	.838	7.07
	average	49	7.3 years	.307±.02	.538±.13	1.27±.07	.797±.11	7.13±.04

TABLE 3.04:
PHOSPHORUS SPECTROSCOPY DATA FROM LONG TERM SURVIVORS

The pH values from both the high dose and low dose regions of brain are within the range of normal variation, as established by our healthy volunteers (7.12 ± .05). None of the metabolite ratios recorded from the long-term survivors differed significantly ($p < 0.05$) from those acquired from our short-term patients, and we can therefore conclude that if any long term damage does occur in brain, it is too small to be detected using ^{31}P NMR spectroscopy at its present level of precision. The areas of the NMR peaks for PME, Pi, PCr and PDE relative to ATP are compared with values from normal volunteers in a series of histograms (Figure 3.03). Although the phosphodiester levels are significantly ($p<0.01$) elevated in irradiated brain, this might be accounted for by the age related elevation in PDE levels, since the long term survivors were an average of 23 years older than the healthy volunteers.

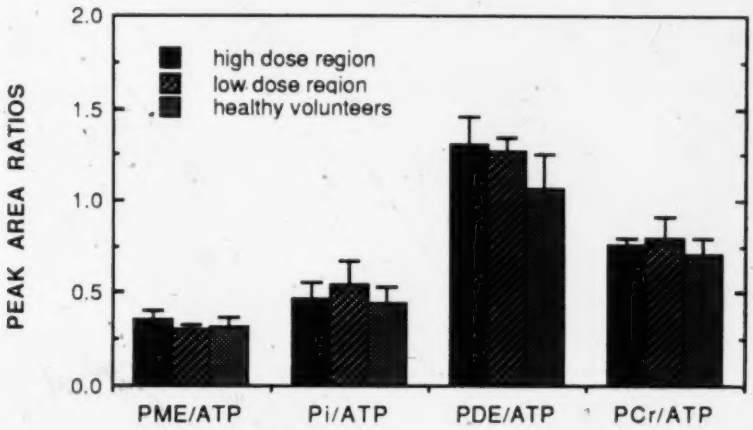

FIGURE 3.03: METABOLITE PEAK AREA RATIOS FROM THE IRRADIATED BRAIN OF LONG TERM SURVIVORS COMPARED TO SIMILAR RATIOS FROM HEALTHY BRAIN.

3.2 NMR Imaging

Radiation induced changes in the central nervous system (CNS) have been noted frequently in magnetic resonance images (26,43,47,85,111). The radiation damage appears as high intensity regions, particularly in white matter, on NMR images obtained with long repetition intervals (3 - 4 s) and long echo times (> 50 ms). Both T_1 and T_2 weighted images display the white matter lesions, although the latter provide superior contrast between normal and damaged tissues (4).

The present study was primarily designed to correlate radiation-induced changes in T_2 calculated images of the CNS with metabolic changes reflected in the phosphorus spectrum of brain. All of the patients who were entered in the phosphorus spectroscopy study also underwent imaging during each NMR session. Unfortunately, imaging data was not acquired prior to radiotherapy from three of these patients (#1 - #3), and consequently their data was considered unsuitable for use in the analysis of the imaging study. The tumor location and zone of irradiation for patient #13 differed from that of all the other patients, and the data could not be analyzed similarly to that of the other patients. Data from this patient was therefore also considered unsuitable for image analysis.

3.2.1 Variability of Transverse Relaxation Time Measurements in Brain

Transverse relaxation times for normal white and grey matter in brain, at 1.5 Tesla, were determined from T_2 calculated NMR images of healthy volunteers. Calculation of the transverse relaxation times, as outlined in Section 1.2.7 of the Introduction, allows the signal intensity of each pixel in a T_2 calculated image to be

directly related to the transverse relaxation time of the corresponding voxel of the imaged tissue.

The slice thickness dependance of such calculated transverse relaxation times of grey and white matter found in the cerebral hemispheres of human brain is listed in Table 3.05. Altering the slice thickness seems to have little effect on the calculated transverse relaxation times of white matter, although the calculated T_2 of grey matter, as well as the range of grey matter values, seem to increase slightly with increased slice thickness. The increased range is reflected through a higher standard deviation associated with the mean transverse relaxation time of the grey matter.

slice thickness	3mm	5mm	10mm
T_2 of WM (ms)	87 ± 6	85 ± 5	85 ± 4
range of WM T_2	(79-98)	(76-95)	(79-91)
T_2 of GM (ms)	97 ± 8	97 ± 10	103 ± 20
range of GM T_2	(87-114)	(89-127)	(87-167)

TABLE 3.05: SLICE THICKNESS DEPENDANCE OF TRANSVERSE RELAXATION TIMES OF CEREBRAL GREY AND WHITE MATTER

The reason for the slice thickness dependance follows from the phenomenon known as the partial volume effect. For example, because of the convoluted distribution of grey matter, CSF and white matter found near the surface of the brain, the measurement of transverse relaxation time of cortical grey matter is often very

difficult *in vivo*. In the thicker slices, there exists an increased probability of overlying tissues or fluids being incorporated into each voxel in the region from which a single data point arises, and this will result in the alteration of the calculated relaxation times, particularly when CSF is incorporated into a voxel together with brain tissue. The use of thin (3 mm) imaging slices was therefore considered beneficial in reducing the probability of CSF underlying, and hence contributing to the apparent T_2 of grey matter. The transverse relaxation times that we measured for brain tissues *in vivo* agree well with those established by other investigators (10,120).

Each T_2 data point is the average transverse relaxation time of 9 adjacent pixels, arranged in a 3 x 3 square matrix. A calculated uncertainty, ranging from 0 - 5% in homogeneous tissue, arises from T_2 variation among the individual pixels. However, these uncertainties increased with greater anatomical inhomogeneity in the region from which the data point arose. The incorporation of two or more pixels with unusually high T_2 values (greater than that of normal brain tissues) into the 3 x 3 matrix of a single data point will increase not only the measured T_2 value, but also the associated uncertainty. CSF, in particular, will noticeably increase the observed relaxation time of a data point, and large T_2 uncertainties were particularly evident in transverse relaxation times for brain tissue found in close proximity to cerebrospinal fluid. This two fold effect of abnormal pixel values allowed us to omit certain data points from the analysis in a systematic way. The omitted points had calculated uncertainties in excess of 10% of the T_2 value, and usually had transverse relaxation times longer than that of normal grey or white matter. In addition, they always arose from CNS tissues close to the periphery of brain, or near CSF-filled fissures and sulci. By comparison, certain other high T_2 values were not omitted. These were

commonly associated with irradiated brain tissue, and displayed small (less than 10%) uncertainty values.

In vivo relaxation time measurements are also subject to error due to magnetic field inhomogeneities, imperfections in the gradient fields and variations in the RF excitation. For a predefined excitation sequence, the spatial variation of image-derived T_2 measurements in our clinical NMR system was quantified (± 5%) using images of an aqueous $CuSO_4$ phantom. Another laboratory has found a spatial variability of ± 7% in $CuSO_4$ phantoms at 1.5 Tesla (71).

The absolute relaxation time of grey or white matter vary also from one anatomical structure to another. A study by Johnson *et al* (120) showed that frontal grey matter at 0.5 Tesla has a transverse relaxation time of 112 ± 15 ms while other cerebral grey matter has a T_2 of only 102 ± 16 ms. Our own studies have shown that white matter structures in the internal capsules of brain have an average transverse relaxation time of 107 ms, which is 20 ms higher than that of surrounding white matter. Real variations in the absolute transverse relaxation times, due to differences in the composition of various anatomical structures, cause approximately a 20% standard deviation in the T_2 values of brain tissue.

In order to interpret radiation induced changes in transverse relaxation times of brain tissue, normal variations in healthy tissue, due to causes such as those outlined above, must be taken into account. For example, relaxation times in the range of 75-120 ms span the normal variation for all tissues found within the cerebral hemispheres. Although this range does not exclude some abnormal values for some tissue types in some locations, it does contain all normal values, and therefore allows us to interpret all values outside this range as abnormal. This strategy is supported by a study in human brain at 0.35 Tesla (26), that showed the transverse relaxation time

of radiation lesions was 50% greater than that of healthy brain tissue. Pathological tissue found in our study was therefore expected to be well beyond the "normal" range of T_2 values that we arbitrarily set.

3.2.2 Imaging Data from Patients

In this imaging study, we attempted to assess radiation damage in the brains of patients, by comparing transverse relaxation times from T_2 calculated images of brain taken prior to radiotherapy, with those from images acquired following RT. Data was collected along lines of interest (LOIs) through the brain, with one LOI being located in the ipsilateral hemisphere, through a region of brain receiving a high dose of radiation, and another LOI located in the contralateral hemisphere, through a region receiving less than 50% of the total radiation dose (refer to Figure 2.01). Due to the similarity in transverse relaxation times between normal white and grey matter, it is difficult to distinguish between these two types of normal tissue in a T_2 calculated image. This is not, however, the case between normal and abnormal brain tissue, where the T_2 differences are much more marked.

In all patients, a peritumoral lesion was noted prior to RT, which displayed transverse relaxation times ranging from 150 to 800 ms. Edema and/or residual tumor are likely contributors to the long T_2 observed in this region. Also, prior to radiotherapy, transverse relaxation times for brain tissues outside of the peritumoral lesion ranged from 76 - 102 ms in white matter, and 86 - 120 ms in grey matter. Patients experiencing T_2 alterations in any region of brain following RT were suspected of having radiation-induced damage. Moreover, any increase in the size of the peritumoral lesion following RT was also cause to suspect radiation damage.

	NMR Spectroscopy Session						
patient	pre RT	post RT	2 mnths	4 mnths	8 mnths	12 mnth	slice orientation
4	30	32	48	33	19	16	transverse
5	38	43	38	35	47	27 A	transverse
6	26	20	21	20			transverse
7	8	12	12	11	11	10	coronal
8	26	25	23	23	21	18	coronal
9	16	14	21	34			coronal
10	31	35	34	37			coronal
11	21	19					coronal
12	17	33					coronal

TABLE 3.06: AREA OF THE PERITUMORAL LESION CALCULATED FROM NMR IMAGES OF PATIENT BRAIN

The symbol 'A' refers to atrophy of brain occurring in the ipsilateral hemisphere. Image slice orientations, in most patients, were coronal, to correspond with the orientation of the isodose distribution diagrams.

The areas of the peritumoral lesions measured from T_2 weighted images taken during each NMR session from each patient entered in the imaging study, are recorded in Table 3.06. Assuming that magnitude changes in the plane we observe reflect similar size changes in all dimensions, the peritumoral lesion spread by greater than 20% following irradiation of brain in patients #4, #5, #9 and #12. This increase in area suggests the presence of radiation induced damage to brain. Several months

following the cessation of RT, a decrease in size was noted in patients #4 and #8, which is indicative of repair of the peritumoral lesion. Figure 3.04 demonstrates temporal alterations in the size of the peritumoral lesion of patient #4. The high reproducibility of slice orientation in successive NMR sessions is also exemplified by the anatomical similarity of the four image slices in Figure 3.04.

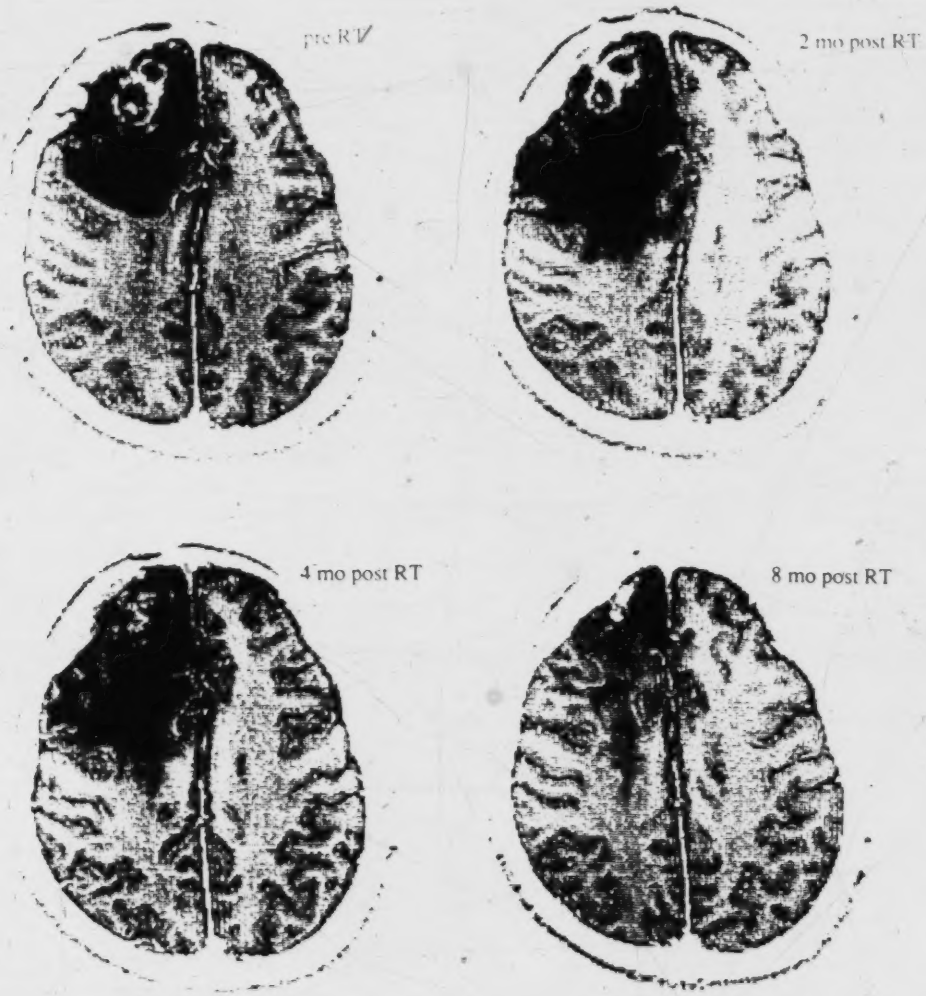

FIGURE 3.04:
CHANGES IN THE SIZE OF THE PERITUMORAL LESION IN PATIENT #4

		Averaged Transverse Relaxation Times (ms) ± Standard Deviations					
patient	region of brain	pre RT	post RT	2 mnths	4 mnths	8 mnths	12 mnth
4	high dose	124±95	120±46	145±71	132±43	115±32	100±14
	low dose	102±30	96±11	93±20	95±16	92±15	103±28
5	high dose	134±57	129±55	134±57	148±77	148±51	236±197
	low dose	94±20	99±21	97±11	102±14	93±12	108±19
6	high dose	132±49	155±87	136±45	167±60		
	low dose	102±21	110±40	114±58	113±22		
7	high dose	316±288	457±552	518±617	584±696	668±788	634±780
	low dose	114±45	108±14	112±22	122±34	128±48	148±66
8	high dose	450±478	587±666	657±789	618±728	634±792	752±911
	low dose	109±25	104±21	107±23	116±31	99±34	106±24
9	high dose	180±125	194±159	199±213	149±93		
	low dose	98±13	102±16	110±41	99±23		
10	high dose	132±69	157±73	155±60	171±81		
	low dose	94±14	99±21	99±19	98±18		
11	high dose	200±123	160±110				
	low dose	106±12	108±26				
12	high dose	112±25	178±97				
	low dose	93±11	93±14				

TABLE 3.07:
COMPARISON OF TRANSVERSE RELAXATION TIMES BETWEEN BRAIN TISSUE OF THE IPSILATERAL AND CONTRALATERAL HEMISPHERES

Image derived transverse relaxation times of brain in the ipsilateral (high dose) and contralateral (low dose) hemispheres of brain are recorded in Table 3.07. Each transverse relaxation time is the mean T_2 of data points found along a LOI, with standard deviations arising from the variation of T_2 values of individual data points from the mean transverse relaxation time. These results show that the ipsilateral hemisphere displays greater increases in T_2 following radiotherapy than the contralateral hemisphere. In fact, only in patient #7 was there any observable increase in transverse relaxation of brain tissue in the contralateral hemisphere. In most

instances, increases in T_2 values of the ipsilateral hemisphere were observed following RT. The degree of these increases was quite variable. For instance, some patients experienced more than a two-fold increase in the transverse relaxation times, while others experienced only minor (10-20%) increases. Figure 3.05 displays these two extremes by plotting temporal alterations in the transverse relaxation times of brain of two patients, one (patient #7) that experienced large increases in T_2 following RT, and another (patient #4), that showed only minor changes.

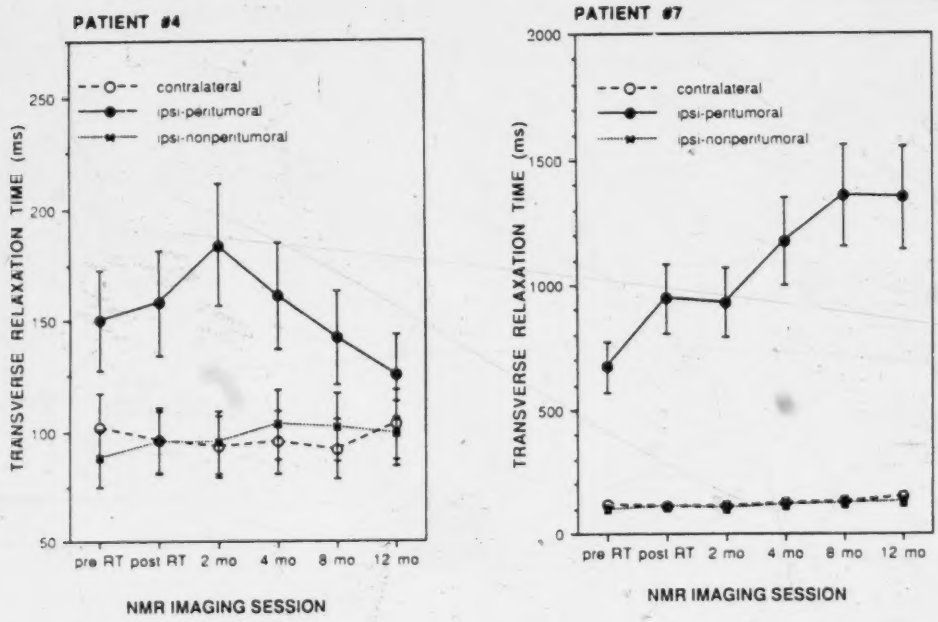

FIGURE 3.05: TEMPORAL ALTERATIONS IN THE TRANSVERSE RELAXATION BETWEEN THE TWO CEREBRAL HEMISPHERES

Data from the two patients plotted to show small (#4) and large (#7) increases in the ipsilateral hemisphere of brain following RT. Patient #7 was the only individual entered in this study to display mean T_2 values in the contralateral hemisphere that extended beyond the limits of normal variation.

Histological studies have previously shown that the extent of radiation damage is dependant not only upon the total dose received, but also on the size of the individual doses and the time interval over which the treatment was given (16). The ipsilateral hemisphere, which receives higher radiation doses than the contralateral hemisphere, is therefore more prone to radiation damage. The presence of edema prior to RT may also predispose the peritumoral region to radiation damage (13), possibly due to increased free radical damage. If this be the case, radiation induced changes in T_2 of the ipsilateral hemisphere might be attributed mainly to alterations in the peritumoral lesion. Confirmation of this was achieved by recording the transverse relaxation times of brain tissue in the ipsilateral hemisphere (Table 3.08). The T_2 of tissue found outside of the peritumoral lesion (TOL) was determined separately from the T_2 of the tissue found within the peritumoral lesion (TIL).

No increases were observed in the in the T_2 of brain found outside of the peritumoral lesion, except in the case of patient #7. Therefore, increases in the overall transverse relaxation time of the ipsilateral hemisphere were, in the majority of cases, due to increased T_2 of the peritumoral lesion. Again, these changes were very large in some cases, and insignificant in others. Of particular interest were the extremely high T_2 values noted in two of the IUDR patients (# 7 & # 8). These patients received no unique surgery or medication compared with the other nine patients, however, examination of augmented cerebral CT scans from the two patients revealed the presence of post-operative poroencephalic cysts, with little or no edema/residual tumor found surrounding the cysts. Hence, all measurements of the long T_2 of the peritumoral lesion in these patients was limited to the cyst. The CSF found inside the cysts could account for the high transverse relaxation times observed in the peritumoral region of patients #7 and #8.

		Averaged Transverse Relaxation Times (ms) ± Standard Deviations					
patient	region of brain	pre RT	post RT	2 mnths	4 mnths	8 mnths	12 mnth
4	TIL	150±30	158±49	184±75	161±40	142±39	125±9
	TOL	88±13	95±17	95±9	103±19	102±16	99±12
5	TIL	166±46	167±61	187±49	211±68	176±42	396±198
	TOL	100±11	94±8	92±10	93±5	94±12	104±10
6	TIL	166±49	188±100	158±45	206±50		
	TOL	93±7	102±24	106±23	102±7		
7	TIL	673±134	945±588	930±596	1177±648	1357±652	1348±739
	TOL	100±17	109±23	102±8	114±26	122±42	128±42
8	TIL	835±437	1153±585	1381±709	1271±639	1518±665	1579±744
	TOL	112±28	101±21	104±42	95±13	95±13	100±17
9	TIL	354±62	344±162	454±264	279±135		
	TOL	97±14	97±9	98±9	96±17		
10	TIL	226±37	261±54	221±24	247±53		
	TOL	107±6	91±6	112±9	113±6		
11	TIL	297±97	248±135				
	TOL	92±7	99±25				
12	TIL	126±25	230±82				
	TOL	97±11	90±11				

TABLE 3.08:
COMPARISON OF TRANSVERSE RELAXATION TIMES BETWEEN TISSUE WITHIN AND TISSUE OUTSIDE OF THE PERITUMORAL LESION

In our study, we noted that the spread of the peritumoral lesion following RT was concentrated in the white matter. We suspect that the nature of the radiation lesion may therefore be demyelination, or vasogenic edema, since both pathologies are associated with spreading along the white matter (24). Prior clinical imaging studies have also noted that the radiation induced damage is commonly found in deep white matter tracts, with relative sparing of brainstem, cerebellum, internal capsules

and basal ganglia (26). The majority of demyelination studies suggest that demyelination and vasogenic edema are related events.

Histological evaluation of radiation induced cerebral edema in animal models shows gradual vascular changes which provide a marked increase in capillary permeability (16). Vasogenic edema, resulting from the extravasation of fluid and small plasma proteins from damaged capillaries, can act as an early indicator of breakdown of the blood brain barrier. Following radiation, histological changes have also been noted in the brain neuroglia. Demyelination has been observed in brain 3-8 weeks following therapeutic irradiation of the CNS (26), and a decrease in the number of oligodendrocytes has also been observed (83). Each oligodendrocyte is capable of maintaining 30 - 50 internodes of myelin, hence destruction of a few oligodendrocytes could perceivably precipitate extensive damage to the myelin sheath. We propose that, following irradiation, damaged oligodendrocytes can no longer maintain the relatively dehydrated state of the myelin sheath (40% H_20) and the sheath begins to swell with increased water content. During demyelination, fluid accumulates in the periaxonal space and between the myelin lamella (106). Approximately half the dry weight of white matter is myelin, thus the hydration of myelin during breakdown would affect the overall relaxation of white matter considerably.

3.3 Proton Spectroscopy

Our proton spectroscopy experiments were used as a pilot study to evaluate the feasibility of using this method to detect and monitor radiation induced damage in brain. All the results are very preliminary, and the conclusions that one might draw can only be substantiated by a long and extensive study of brain tumor patients.

3.3.1 General Considerations

Utilizing the STEAM pulse sequence with a long spin echo time (refer to Section 2.3.2 of the Methods), *in vivo* proton spectra of human brain were obtained at 1.5 Tesla. Under these conditions, three distinct metabolite peaks were observed. These three NMR peaks were the resonances of methyl protons from choline (Cho), from creatine and phosphocreatine (Cr) and from N-acetyl aspartate and other acetyl compounds (NAA). The resolution of all three peaks was, in the majority of cases, complete, although the choline and creatine peaks sometimes overlapped slightly.

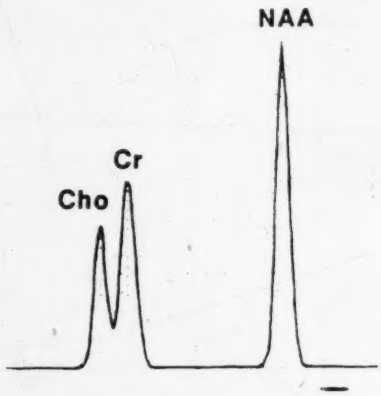

FIGURE 3.06:
AN EXAMPLE OF A FITTED ^{1}H SPECTRUM OF HEALTHY BRAIN

In keeping with the curve-fitting techniques employed in the phosphorus spectroscopy study, Gaussian line shapes were used to fit the metabolite peaks. Only the water peak was best fitted with a Lorentzian curve. Again, the initial curve fitting was optimized using the SIMPLEX routine, and the resultant fitted spectrum (Figure 3.06) was used in our experimental analysis.

Due to day to day mechanical changes in the NMR machine, inclusion of a concentration standard is imperative for the accurate assessment of NMR spectra. However, since the B_0 localization method of the STEAM pulse sequence prevented the inclusion of an external concentration standard in the field of view, the exploitation of one of the naturally occurring metabolites in the brain as a concentration reference had to be considered. Unfortunately, no really suitable candidate exists. Nonetheless, our efforts to rationalize the situation are described below.

A previous study on ^1H NMR spectroscopy of brain excised from rats following cranial irradiation showed decreased choline/methylene ratios in organic brain extracts, and increased Cho/NAA ratios in aqueous extracts (96). Therefore NAA and Cho were immediately excluded as internal concentration references. Another article, dealing with *in vivo* proton spectroscopy in the brains of children, showed a decreased area of the NAA peak following cranial radiation therapy, and similar decreases were seen in the brains of patients having undergone chemotherapy. Although radiotherapy seemed to have no effect on the creatine levels in brain in the above mentioned studies, a decrease in creatine has been associated with decreased NAA levels in other brain pathologies, such as following stroke (12). Consequently,

none of the metabolites visible in the ^{1}H NMR spectrum may provide a suitable internal concentration standard.

The only alternative remaining appears to be the use of the water resonance as an internal concentration standard. The exploration of water as a concentration standard was not an easy option to accept, and the first 6 of 10 volunteer sessions and 12 of 19 patient sessions reported here were carried out before a protocol for water standardization was established. In order to utilize water as a concentration standard, it is necessary to acquire two proton spectra from each region of brain studied. For the first spectrum acquired, water suppression techniques are employed to enable the metabolite peaks of Cho, Cr and NAA to be observed clearly. A second spectrum is then acquired from the same region of brain, but without water suppression. Section 2.3.2 of the Methods explains the pulse programs in more detail. The area under each of the metabolite peaks can then be directly compared to the area under the water peak. One possible difficulty with this strategy is the spatial variability of water retention. Water retention is often a consequence of tissue damage, and it may therefore cause the water content to vary across the brain. It may also vary considerably between patients, depending upon the severity of cerebral damage in the areas of interest in each individual patient. It is, however, not expected to vary much in the low dose regions. Normal baseline values were obtained from healthy volunteers, in whom little variation in water content was anticipated.

An indication of the variability of all possible peak combinations is given in Table 3.09, where a 10 - 20% standard deviation in metabolite peak area ratios was observed among healthy volunteers. Variations due to repeated spectral analysis of the same data file were much less than variations between separate spectra. For

example, multiple processing of the same raw data file resulted in peak area ratios with less than a 5% standard deviation (SD) from the mean value. The standard deviation, in the measurements of relative metabolite abundances among healthy brains, reported in this thesis, arises therefore primarily from biological variation rather than from a lack of processing reproducibility. With these standard deviations, no differences could be detected between the relative metabolite concentrations measured in different anatomical regions of healthy brain (Table 3.09). This consistency of metabolite peak areas among different regions of brain, is in agreement with previous NMR studies (32).

Metabolite Ratio	Region of Brain		
	Temporal	Occipital	All
NAA/Cho	2.29±.45	2.15±.35	2.24±.41
NAA/Cr	2.07±.42	2.15±.35	2.10±.39
Cr/Cho	1.13±.23	1.02±.24	1.09±.23
NAA/H_2O $(x10^{-2})$	.773±.08	.789	.776±.07
Cho/H_2O $(x10^{-2})$	.364±.05	.297	.351±.05
Cr/H_2O $(x10^{-2})$	.469±.04	.432	.461±.04

TABLE 3.09: MEAN ^1H METABOLITE RATIOS FROM BRAINS OF HEALTHY VOLUNTEERS

The metabolite ratios are given as the mean ± standard deviation. "Means" without standard deviations represent values from a single measurement. Raw data is listed in Appendix V.

Chemically determined concentrations of N-acetyl compounds in brain are quoted in the literature as 5-10 mM. Although N-acetyl aspartate comprises the majority of the acetyl compounds in brain, other N-acetyl moieties, such as N-acetlyglutamate and N-acetylaspartyl glutamate, contribute approximately 0.5 mM to the total N-acetyl pool (95). Values for the concentration of the creatine range between 8 and 10 mM in the literature. The concentration expected for choline depends upon its morphological environment. For example, choline is found in three states in cells, namely, free choline, phosphocholine and phosphatidylcholine. Phosphatidylcholine comprises approximately 90% of choline in the cell (87), although it is membrane-bound and is therefore not visible with the long SE times that we use in our NMR experiments. Biochemical analysis of the free choline fraction in brain yields concentrations of less than 50 μM, and is not in sufficient quantities to be detected by *in vivo* NMR. By the process of elimination, the water soluble phosphocholine pool appears to be the principle contributor to the choline signal observed in ^{1}H spectroscopy. Chemically derived concentrations of phosphocholine in brain could not be found in the literature. Nevertheless, *in vitro* NMR analysis of perchloric extracts of excised samples of brain provide a measure of the water soluble metabolite concentrations. NMR analysis of these extracts (91) is summarized in Table 3.10. Included in this table are the estimated concentrations of the metabolites that are freely mobile in the cell; and hence visible by NMR. By normalizing the concentration of choline observed *in vivo* to that observed *in vitro*, metabolite concentrations of NAA and Cr could be estimated from the relative metabolite ratios of several *in vivo* studies, namely, Frahm *et al* (32), Arnold *et al* (3) and Jenesen *et al* (58), as well as our own.

Metabolite	Concentration (mM) ± SD				
	in vitro	*in vivo*			
reference	(86)	this work	(32)	(3)	(58)
choline	1.1 ± .3	1.1	1.1	1.1	1.1
Cr + PCr	5.7 ± .6	1.5 ± .4	0.9	5.0	0.8
NAA	4.3 ± .7	2.6 ± .5	2.2	8.5	4.3

TABLE 3.10:
ESTIMATES OF BRAIN METABOLITE CONCENTRATIONS IN HEALTHY BRAIN DETERMINED BY NMR

The *in vitro* results presented in this table arises from a study by Petroff *et al* (91) utilizing perchloric acid extracts of human brain. The first set of *in vivo* previous clinical studies (32,3,58).

3.3.2 Patient Data

A total of 10 patients were entered into the proton spectroscopy study. Several of these patients had only low grade or pituitary tumors, which were treated with lower doses of radiation than patients having the more aggressive tumors. In spite of this, observable alterations in the ^{1}H NMR spectrum of brain were observed in the brains of several patients following radiotherapy (Figure 3.07). Notice, that in this particular case, even prior to RT, the spectrum from the ipsilateral hemisphere of the brain (a region that is anticipated to receive high doses of radiation) differs slightly from that of normal brain, in that the NAA peak is no longer as large, relative to the Cho and Cr peaks, as it is in the spectra from healthy brain. These observations are not repeated in the contralateral (low dose) hemisphere.

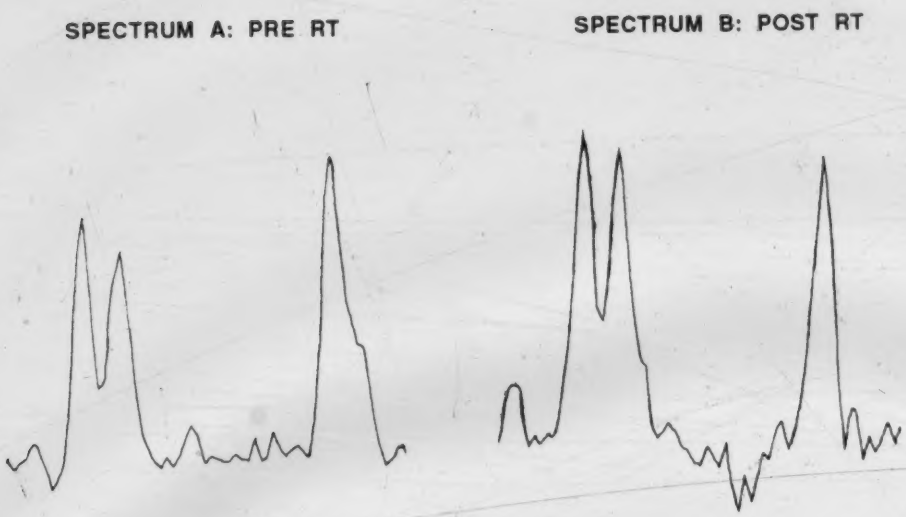

FIGURE 3.07: EXAMPLES OF ^1H SPECTRA OF BRAIN PRIOR TO AND FOLLOWING CRANIAL IRRADIATION

The spectrum on the left was acquired from brain tissue prior to RT, in a region that was expected to receive high doses of radiation. The spectrum on the right was acquired from the same brain (patient #22), immediately following radiotherapy.

Comparison of the concentrations of brain metabolites with respect to water suggest that decreases in NAA/H_2O are often accompanied by decreases in choline/water or creatine/water peak ratios also. For example, one patient displayed decreases, relative to water, in all the metabolite ratios. High levels of brain water might have been responsible for this effect. However, other patients displayed decreases in two of the metabolite/water ratios, but not in the third, suggesting that the observed decreases might be real, and not due to increased tissue water. The metabolite/H_2O levels are recorded in Table 3.11. Only a small number (n) of patients were analyzed using the water reference.

Unfortunately, there is no pre RT data with which we can compare the post RT data. However, immediately following radiotherapy, levels of NAA and Cr, relative to that of water, show a 50% decrease below normal levels in the high dose region of brain. Choline levels are still found within the limits of normal variation at this time, although they decrease slightly in the high dose region several weeks later. These results show that all three metabolite/water peak ratios from patient spectra display changes compared to corresponding ratios from healthy brains, thereby confirming that none of these metabolites is really suitable for use as a concentration reference. Nonetheless, because water standardization is not available for all data sets, and in order to analyze the majority of our data, relative metabolite concentrations have to be compared.

n	NMR session	region of brain	Cho	Cr	NAA
1	post RT	high dose	.00389	.00179	.00295
		low dose	.00357	.00399	.00754
2	2 month	high dose	.00229	.00324	.00492
		low dose	.00281	.00422	.00574
1	4 month	high dose	.00302	.00450	.00791
		low dose	.00436	.00450	.00816
2	8 month	high dose	.00173	.00407	.00395
		low dose	.00266	.00241	.00612
1	12 month	high dose	.00374	.00341	.00641
		low dose	.00321	.00424	.00744

TABLE 3.11: METABOLITE/WATER PEAK AREA RATIOS FROM ^1H SPECTRA OF THE CNS OF PATIENTS

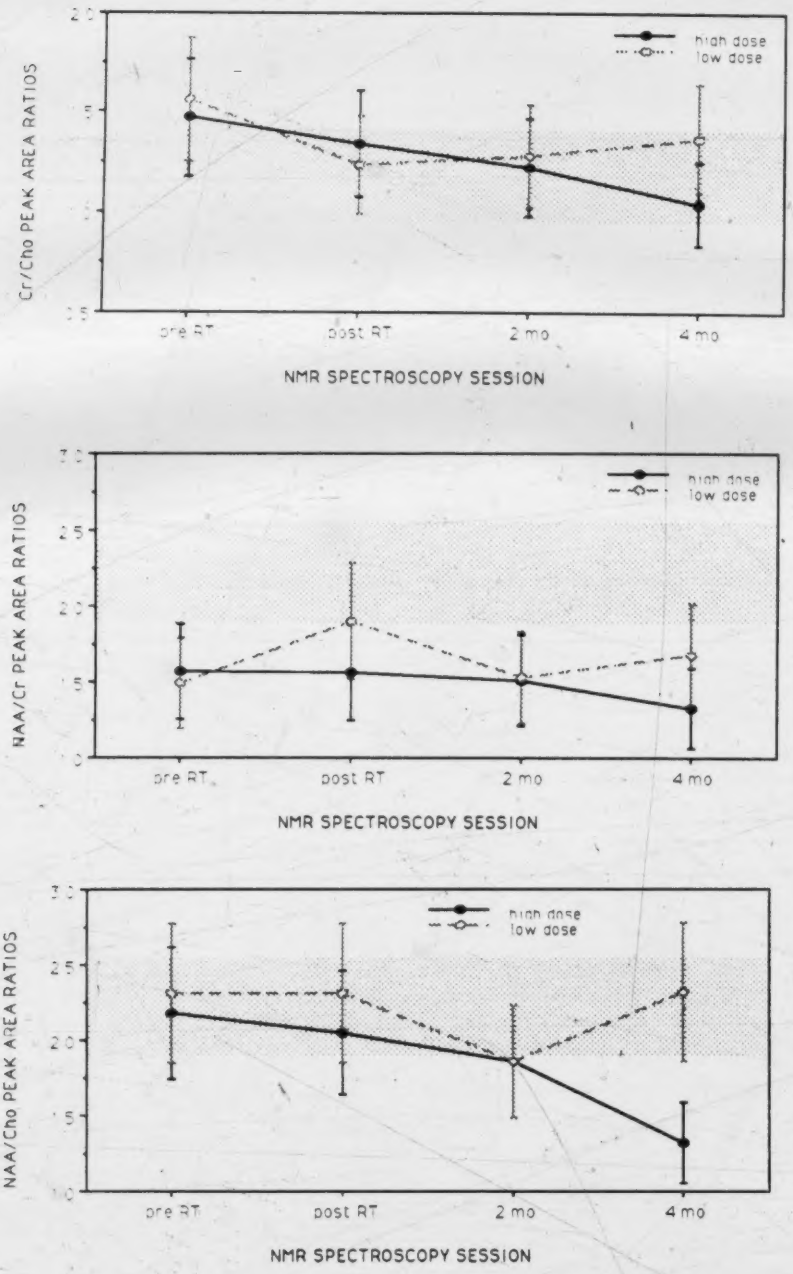

FIGURE 3.08: RELATIVE PEAK AREA RATIOS FROM ^1H SPECTRA OF THE CNS OF PATIENTS

We chose to study NAA/Cr, NAA/Cho and Cr/Cho metabolite ratios in order to compare all possible metabolite ratios. This data is plotted in Figures 3.08 a-c. The data points at 8 months post RT are the means of data from only two patients, while the 12 month point arises from a single patient. Therefore, these data points are not very reliable. Other data points represent means arising from data of 3 - 6 patients each.

Certain metabolite ratios in the CNS of patients, even prior to RT, differed from similar ratios from the brains of healthy volunteers. Specifically, NAA/Cr ratios were 78%, and Cr/Cho ratios were 124%, of the "normal" values established from the healthy volunteers. There was no noticeable difference in the NAA/Cho ratio between patients and healthy volunteers, and therefore it was assumed that the "abnormal" values observed in the previous two ratios were due mainly to higher creatine levels of the brain.

The source of the elevated creatine levels is not likely surgery, since many of the patients analyzed by proton spectroscopy underwent a needle biopsy rather than full surgery. Although the presence of tumor cells in the "normal" tissue surrounding the tumor may effect metabolite levels, brain tumors typically have elevated choline levels, therefore the observed increase in the Cr/Cho ratio cannot be explained by tumor effects. Some of the patients did not receive any medications, and therefore side effects of medications cannot explain the increased creatine levels either. Another possible explanation involves the age discrepancy between healthy volunteers (mean age = 26) and patients (mean age = 40). If we consider the skeletal muscle study done by Satrustegui *et al* (100), the age difference between our two sets of volunteers (healthy individuals and patients) would result in a 40% increase in the (Pi+PCr)/βATP ratio. Although it is difficult to determine exactly what metabolite is

changing, this increase potentially can explain the increased creatine levels that we observe in the brains of our patients.

Some patients exhibited a marked post-irradiation alteration in metabolite ratios, while other patients experienced little or no change. For example, patient #22 experienced a 60% decrease in Cr/Cho and NAA/Cho ratios immediately following RT, while patient #20 actually experienced a slight increase in the same ratios. Nonetheless, a statistical analysis was performed on metabolite peak area ratios between the high dose and low dose regions of brain. Following RT, the NAA/Cr ratio in the high dose region is significantly ($p<0.01$) lower than in the low dose region. This suggests that the higher the doses of radiation received by brain, the greater may be the potential for biochemical alterations in the CNS. There is no significant difference in Cr/Cho or NAA/Cho ratios between these two regions of brain.

Although not all patients experienced changes in relative metabolite ratios following RT, it is interesting to note that there is a relationship between patients who displayed changes in cerebral metabolites, especially NAA/Cho ratios, and the medication that the patients were receiving during radiotherapy. NAA/Cho ratios were significantly lower ($p<0.05$) in the high dose region of irradiated brain in patients receiving no Decadron than they were in the high dose regions of brain in patients who did take the medication. Overall Cr/Cho and NAA/Cr ratios did not display a statistically significant Decadron dependance, although a complete statistical analysis, that included temporal variations, could not be performed due to the shortage of data points. Figure 3.09, however, suggests that changes in the Cr/Cho ratio are also Decadron dependant; there is a sharp decrease in the Cr/Cho

immediately following RT in patients not taking Decadron, while patients who are on the drug display a lesser decrease.

FIGURE 3.09a

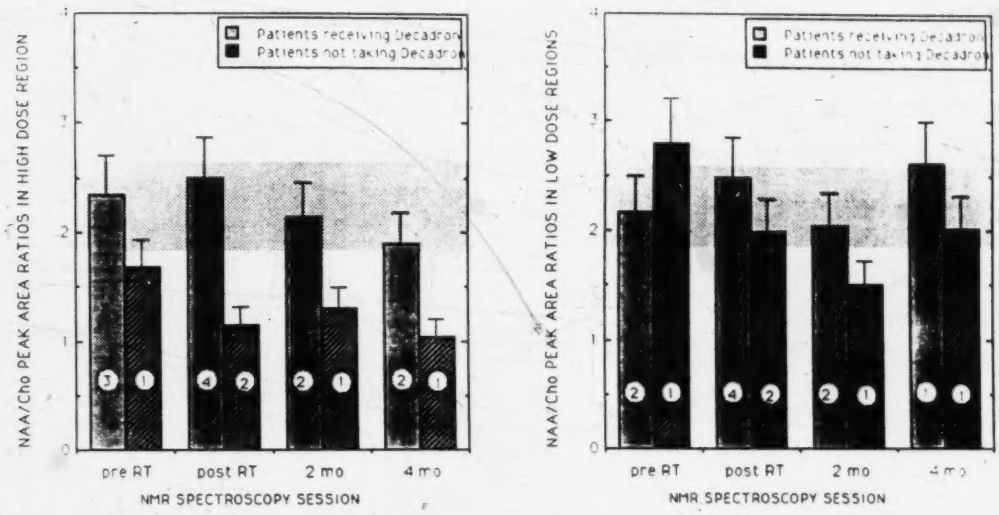

FIGURE 3.09b

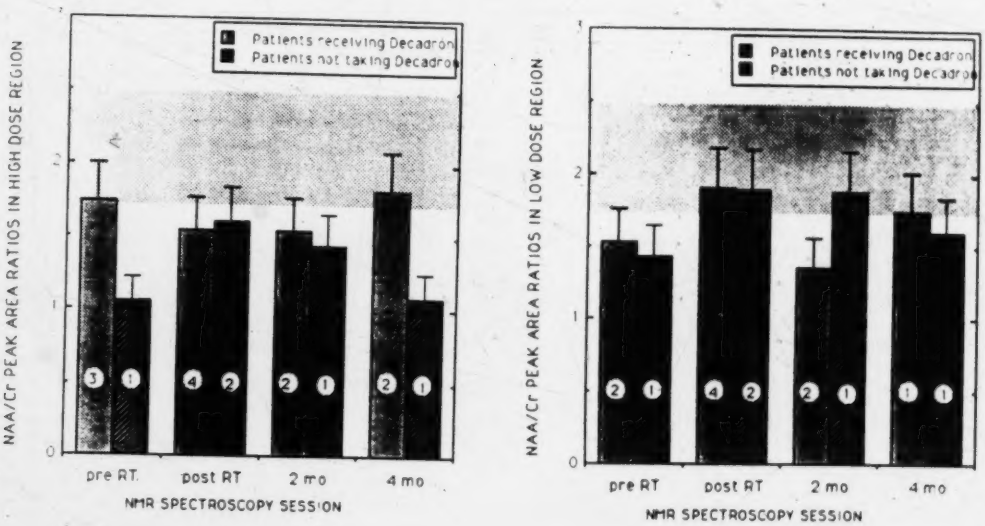

FIGURE 3.09c

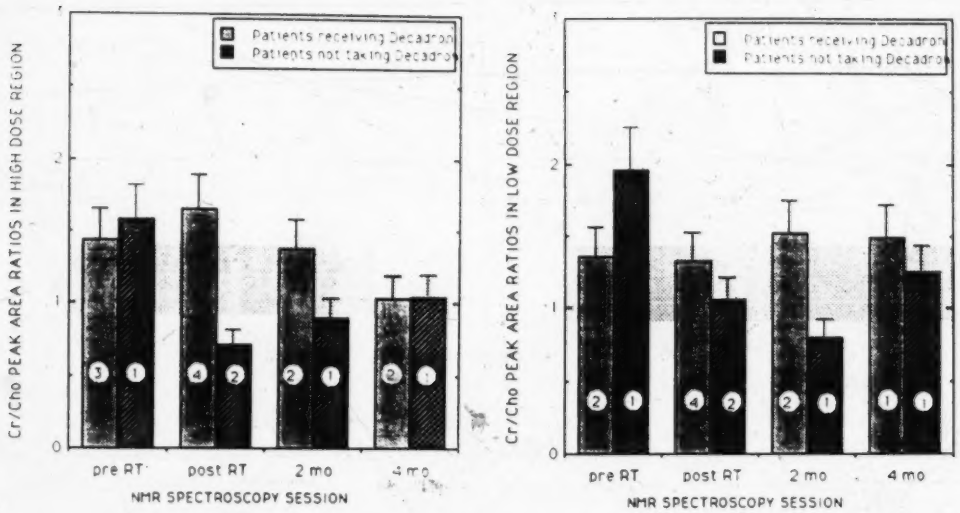

FIGURE 3.09: THE EFFECT OF DECADRON ON ^{1}H METABOLITE RATIOS FROM IRRADIATED BRAINS

Mean metabolite ratios from the high dose and low dose regions of patient brains are compared between patients who were taking Decadron during radiotherapy, and those who were not. Standard deviations are given as the expected measurement uncertainty (15%). The number of patients, contributing data to a value, are listed in the white circles. Horizontal shaded region on the graphs represents the limits of normal variation of metabolite peak areas as established by our healthy volunteers.

Decadron is the trade name for dexamethasone, a synthetic glucocorticoid drug. The drug exerts an anti-inflammatory effect on tissues, and is therefore often given to patients with brain tumors to decrease inflammation associated with the tumor, surgery or radiotherapy. The biochemical mechanism by which Decadron exerts an effect on brain metabolite levels, especially during radiotherapy, is not well understood due to the scarcity of literature on this topic. However, since it has been suggested that edematous tissue is more prone to radiation damage than healthy tissue (13), Decadron may indirectly increase the radioresistance of tissues by decreasing the excess fluid retention.

N-acetyl aspartate is only found in NMR detectable quantities in the neurons of the brain (101). Thus, alterations in the NAA content of brain are thought to reflect damage to the brain parenchyma. Previous ^{1}H spectroscopic studies have shown decreases in NAA levels in the brains of individuals with multiple sclerosis (3), and individuals who have recently experienced a stroke (6,12). Another study on terminal ischemia in rats showed marked decreases in the NAA peak relative to both creatine and choline (91).

The majority of choline, being a constituent of phosphatidylcholine found in membranous structures of the brain, relaxes quickly, and cannot be detected by the pulse sequence that we use in our NMR experiments. Therefore, the increase in the choline NMR signal that we see in brain following RT, likely reflects the increased mobility of choline from the lipid sources, which in turn may reflect breakdown of the plasma or intracellular membranes. This theory is supported by results from a previous study of aqueous brain extracts from rats that had been irradiated *in vivo* (96). In this study, it was reported that increased Cho/NAA peak ratios ($.72 \pm .21$), compared to the normal value ($.51 \pm .04$) occurred in brain following irradiation. In addition, analysis of organic extracts from the same brains suggested that decreases in phosphatidylcholine, phosphatidlyethanolamine and phosphatidylserine occur. The authors concluded that radiation induced damage to cells may cause the breakdown of membrane lipids, resulting in elevated levels of the water soluble phosphocholine. However, since the Cho levels in irradiated rat brain are compared to the size of the NAA peak, it is difficult to discriminate between changes in choline and changes in N-acetyl aspartate.

CHAPTER 4: CONCLUSIONS

The initial purpose of this study was to determine if nuclear magnetic resonance had the potential to detect radiation-induced damage in human brain following therapeutic doses of radiation. Although many of our results are preliminary, the conclusions that we have drawn from this study can form the basis of a more thorough investigation, which would require several years of data acquisition from the CNS of patients that have undergone therapeutic cranial irradiation.

Our imaging results revealed, in some of the glioblastoma patients, increases in the size or the transverse relaxation time of the post operative peritumoral lesions found in the brain. Increases in the size of the lesion following radiotherapy ranged from barely perceptible changes, to increases of 50% or more. In the case of the transverse relaxation times, increases were not even observed in some patients, while others experienced up to a two fold increase in T_2. Patients developing post operative poroencephalic cysts displayed the largest (two fold) increases in T_2 , possibly due to clearance of proteins from the fluid in the cystic region.

When initiating the phosphorus spectroscopy study, we had thought that changes in the energy metabolites (PCr, Pi and ATP) would be sensitive to radiation-induced damage to brain. However, we had not anticipated the large normal variation ($\pm$ 13-21%) found in metabolite/ATP peak area ratios among the brains of healthy volunteers. This large variation originates not only from biological variation, but also from processing reproducibility and measurement uncertainty. Future improvements in hardware and software may increase the precision of data processing and data

collection, which in turn might reduce the apparent normal variation in phosphorus metabolite peak area ratios in brain. Nonetheless, at our current level of precision, we were able to detect above normal (as established by our healthy volunteers) PDE/ATP and PCr/ATP ratios in spectra from the CNS of brain tumor patients. These elevated levels were evident prior to RT, and persisted throughout the course of our study. Age related changes in the levels of phosphate metabolites have been observed in human muscle (76,100). Similar age related changes may be responsible for observed differences between the PDE/ATP and PCr/ATP ratios in brain tissue of healthy volunteers and that of the patients, since the mean age of the patients is 11 years higher than the mean age of the volunteers. The four long term survivors of brain tumors, who each underwent therapy 4-7 years prior to their NMR session, also displayed the above "normal" PCr/ATP and PDE/ATP ratios. Again, these increased levels were thought to be due to the more advanced age of the long term survivors, compared to that of the healthy volunteers. The degree of uncertainty, caused by the age discrepancy between healthy volunteers and patients, would be removed by analyzing age-matched healthy volunteers.

Apart from the supposed age related increases, no other visible alterations in metabolite ratios were observed in the irradiated brains of patients. This suggests that radiation induced changes that may be occurring in the CNS, do not cause the metabolite peak area ratios to extend beyond the limits of normal variation. However, our proton spectroscopy results suggest that the levels of phosphomonoesters, specifically phosphocholine, may be altered by radiation induced damage. This finding leads us to wonder whether the concentrations of other ^{31}P metabolites might change following RT, but that these changes are too small to be detected by phosphorus spectroscopy at its present level of sensitivity.

The second set of patients observed, namely, that analyzed using proton spectroscopy, reveals several changes in the brain spectra, compared to those of healthy volunteers. First, below normal (mean decrease of 22%) NAA/Cr ratios and above normal (mean increase of 24%) Cr/Cho ratios were found in brains of patients, even prior to RT, in both the high dose and low dose regions. The NAA/Cho ratio, however, was normal. This suggests that these patients have higher creatine levels, than healthy volunteers. Second, the NAA/Cr levels following RT are significantly ($p<0.01$) lower in the high dose regions than the low dose regions, suggesting a decrease in the levels of NAA, or increase in the levels of creatine.

The increased creatine levels noted prior to RT may be associated with the mean age difference (14 years) between the patients and the healthy volunteers. Our ^{31}P results, which show a 12% increase in the PCr/ATP ratio of the patients, compared to the younger, healthy volunteers, supports the theory of increased creatine levels. Since phosphocreatine comprises only a portion (approximately 30%) of the total creatine pool, the total change in creatine might be greater than expected for the PCr. A skeletal muscle study, which estimates a 40% difference in the (Pi+PCr)/βATP ratio between humans with a 14 year age discrepancy, further supports our theory that creatine levels may increase with age. As mentioned earlier, it is important to study age-matched volunteers, in order to determine if the differences in the metabolite ratios are, in fact, due to the age difference.

The change in NAA/Cr ratio in the ipsilateral hemisphere of the brain may be due to Wallerian degeneration of nerves following brain surgery to remove the tumor. The NAA levels are lower than normal in several of the patients, even prior to radiotherapy. Furthermore, these decreased NAA levels are noted only in the hemisphere of the brain that has undergone surgery. Wallerian degeneration involves

death of the axon of the cell after it has been severed from the cell body, and since damage to normal brain tissue surrounding the tumor is unavoidable during surgery to debulk the tumor, a certain degree of Wallerian degeneration might be expected to occur. NAA levels often decrease further, relative to choline or creatine, following RT, but it is difficult to determine if these changes are due to the radiation, or just delayed effects of the surgery. In order to remove this degree of uncertainty, brain tumor patients having undergone needle biopsies, rather than full surgery, should be studied using proton NMR spectroscopy.

Proton spectroscopy results also show that patients receiving Decadron (+Dc) display substantially different metabolite levels following radiotherapy than patients who are not receiving Decadron (-Dc). Although overall NAA/Cho or Cr/Cho ratios do not alter significantly between high and low dose regions of brain, several changes are observed if -Dc patients are analyzed separately from +Dc patients. Specifically, below normal NAA/Cho ratios are found in the high dose region of brain in -Dc patients, but not in the low dose region of -Dc patients, or in either region of +Dc patients. In the -Dc patients, the NAA/Cho levels decrease following RT, and remain decreased until at least 4 months post RT. Also, it seems that Cr/Cho levels drop sharply in the -Dc patients immediately following RT, but slowly return to normal. The NAA/Cr levels in -Dc patients do not display any consistent changes compared to the levels in +Dc patients. Therefore, since only Cho/Cr and NAA/Cho ratios are effected, it would seem that Decadron somehow influences the levels of choline found in brain following radiotherapy.

From our observed results, we can postulate what might be happening in brain following RT. First, surgery causes damage to the neuroglia, including the neurons themselves. Decreased levels of NAA in the ipsilateral hemisphere of brain

result from the Wallerian degeneration of neurons that have been severed from cell bodies during surgery. Following radiotherapy, choline levels increase in both hemispheres of the brain. Damage to cell membranes, induced by radiation, causes water soluble phosphocholines to be released. Therefore, cell damage would precipitate decreased ratios of NAA/Cho and Cr/Cho, due to the increased choline levels. Although phosphocholine is a monoester, no noticeable change occurred in the phosphorus NMR spectrum, possibly due to the numerous other components found under the PME peak. As membrane damage stabilizes, and begins to repair itself, the concentration of Cho in the cell returns to normal. The concentration of NAA may also return to normal, albeit more slowly. Changes in the metabolite ratios, following radiotherapy, are more pronounced in patients who are not taking the drug, Decadron. Since the presence of edema may predispose tissue to radiation damage (13), the Decadron can potentially reduce the initial damage indirectly, by reducing the edema in the brain.

This hypothesis cannot be totally substantiated from our proton spectroscopy data, since single data points are not reliable. More data, particularly from 8 month and 12 month NMR sessions,are required to determine if cerebral metabolite levels return to normal during that period of time. Therefore, further experimentation is required before definite conclusions may be drawn. Although a long period of time is required for the collection of sufficient data to form a more complete study, our results provide a solid basis upon which further NMR studies, on irradiated brain, can be based.

REFERENCES

1 Andrews BT, PR Weinstein, M Keniry, B Pereira (1987) Sequential *in vivo* Measurement of Cerebral Intracellular Metabolites with ^{31}P MRS during Cerebral Ischemia and Reperfusion in Rats. *Neurosurgery* **21**, 699-707.

2 Arnold A, P Baily, RA Harvey, LL Hass, JS Laughlin (1954) Changes in the Central Nervous System following Irradiation with 23 MEv Xray *Radiology* **62**, 37-42.

3 Arnold DL, PM Matthews, G Francis, J Antel (1989) Proton MR Spectroscopy in the Evaluation of Multiple Sclerosis in Humans *in vivo*. Abstract. *Proceedings from the 8th SMRM, Amsterdam.* p 455.

4 Barnes P, WI McDonald, PS Tofts, G Johnson, DN Landon (1986) Magnetic Resonance Imaging of Experimental Oedema. *J. of Neurol. Neurosurg. Psychiatry* **49**, 1341-1347.

5 Bendall MR, RE Gordon (1983) Depth and Refocusing Pulses Designed for Multipulse NMR with Surface Coils. *J. Mag. Res.* **53**, 365-385.

6 Berkelbach JW, PR Luyten, PC van Rijen, CAF Tullen, JA den Hollander (1988) Cerebral Lactate Detected by Regional Proton MRS in a Patient with Cerebral Infarction. *Stroke* **19**, 1556-1560.

7 Birken DL, WH Oldendorf (1989) N-Acetyl-L-Aspartatic Acid: A Literature Review. *Neuroscience and Biobehavioral Reviews* **13**, 23-31.

8 Bookwalter JW, RG Selker, L Schiffer, M Randall, D Iannuzzi, M Kristofik (1986) Brain-Tumor Cell Kinetics Correlated with Survival. *J. Neurosurg.* **65**, 795-798.

9 Bottomly PA, TB Foster, RD Darrow (1984) Depth-Resolved Surface-Coil Spectroscopy for *in vivo* ^{1}H, ^{31}P and ^{31}C NMR. *J. Mag. Res.* **59**, 338-342.

10 Bottomly PA, CJ Hardy, RE Argsinger, G Allen-Moore (1987) A Review on ^{1}H Nuclear Magnetic Relaxation in Pathology. *Med. Phys.* **14**, 1-37.

11 Brock M, J Cervos-Navarro, B Holdorff (1984) Changes in Intracranial Pressure Associated with Delayed Cerebral Radionecrosis. *Surg. Neurol.* **22**, 8-16.

12 Bruhn H, J Frahm, ML Gyngell, KD Merboldt, W Hanicke, R Sauter (1989) Cerebral Metabolism in Man after Acute Stroke. *Mag. Res. in Med.* **9**, 126-131.

13 Burger PC, S Mahaley, L Dudka, FS Vogel (1979) The Morphologic Effects of Radiation Administered Therapeutically for Intracranial Gliomas *Cancer* **44**, 1256-1272.

14 Calderini G, G Toffano (1982) Phospholipid Methylation, ^{3}H-Diazepam and ^{3}H-GABA Binding in the Cerebellum of Aged Rats in: Giacobini E, G Filogamo, G Giacobini, A Vernadakis (eds) The Ageing Brain Raven Press, NY

15 Calvo W, JW Hopewell, HS Reinhold, TK Yeung (1988) Time and Dose Related Changes in the White Matter of the Rat Brain after Single Doses of Xrays. *Br. J. of Radiology* **61**, 1043-1052.

16 Caveness WF (1980) Experimental Observations: Delayed Necrosis in Normal Monkey Brain. in: Gilbert HA and AR Kagan (eds) Radiation Damage to the Central Nervous System. Raven Press, NY. pp1-39

17 Cerdan S, V Harihara Subramanian, M Hilberman, J Cone, J Egan, B Chance, JR Williamson (1986) 31P NMR Detection of Mobile Dog Brain Phospholipids. *Mag. Res. in Med.* **3**, 432-439.

18 Chapman JD, CJ Gillespie (1981) Radiation Induced Events and their Timescale in Mammalian Cells. in: Advances in radiation biology, volume 9, Academic press.

19 Chapman DJ (1980) Biophysical Models of Cell Inactivation by Radiation. in: Meyn RE, HR Withers eds. Radiation Biology in Cancer Cells Raven Press, NY.

20 Chapman JD, AP Reuvers, J Borsa, CL Greenstock (1973) Chemical Radioprotection and Radiosensitization of Mammalian Cells Growing *in vitro*. *Radiation Research* **56**, 291-306.

21 Choucair AK, VA Levin, PH Gutin, RL Davis, P Silver, M Edwards, CB Wilson (1986) Development of Multiple Lesions during Radiation Therapy and Chemotherapy in Patients with Gliomas. *J. Neurosurg.* **65**, 654-658.

22 Constine LS, A Konski, S Ekholm, S McDonald, P Rubin (1988) Adverse Effects of Brain Irradiation Correlated with MR and CT Imaging. *Int. J Radiation Oncology Biol. Phys.* **15**, 319-330.

23 Courville CB, RO Myers (1958) The Process of Demyelination in the Central Nervous System II. *Exp. Neurol.* **17**, 158-173.

24 Cowley AR (1983) Influence of Fibre Tracts on the CT Appearance of Cerebral Edema. *AJNR* **4**, 915-925.

25 Curran WJ, C Hecht-Leavitt, L Schut, RA Zimmerman, DF Nelson. (1987) Magnetic Resonance Imaging of Cranial Radiation Lesions. *Int. J. Radiation Oncology Biol. Phys.* **13**, 1093-1098.

26 Dooms GC, S Hecht, M Brant-Zawadski, Y Berthiaume, D Norman, TH Newton (1986) Brain Radiation Lesions: MR Imaging. *Radiology* **158**, 149-155.

27 Druckmann A (1929) Schlafsucht als Folge der Roentgenbestrahlung. *Strahlen-Therapie* **33**, 382-384.

28 Emoto SE, D Kintner, JM Feyzi, DD Gilboe (1988) Relating Cerebral Ischemia and Hypoxia to Insult Intensity *J. Neurochem* **50**, 1952-1958.

29 Fan T, RM Higashi, AN Lane, O Jardetzky (1986) Combined use of ^{1}H NMR and GS-MS for Metabolite Monitoring and *in vivo* ^{1}H-NMR Assignments. *Biochemica et Biophysica Acta* **882**, 154-167.

30 Frahm J, KD Merboldt, W Haenicke (1987) Localized Proton Spectyroscopy using Stimulated Echoes. *J. Mag. Res.* **72**, 502-508.

31 Frahm J, H Bruhn, ML Gyngell, KD Merboldt, W Hanicke, R Sauter (1989) Localized High-resolution Proton NMR Spectroscopy using Stimulated Echos. *Mag. Res. in Med.* **9**, 79-93.

32 Frahm J, H Bruhn, ML Gyngell, KD Merboldt, W Hanicke, R Sauter (1989) Localized Proton Spectroscopy in Different Regions of the Human Brain. *Mag. Res. in Med.* **11**, 47-63.

33 Freeman JE, PGB Johnston, JM Voke (9173) Somnolence after Prophylactic Cranial Irradiation in Children with Acute Lymphoblastic Leukemia. *Br. Med. Journal.* **4**, 523-525.

34 Fulton DF, Urtasun RC, Lester SG, Silverstein M, Wasserman T, Martz K (1990) A Phase I RTOG Study of IUdR and Radiotherapy in the Treatment of Malignant Brain Tumors. Abstract, *Proceedings from the 4th Canadian Neuro-Oncology Meeting, Winnipeg.*

35 Gadian DG (1982) Nuclear Magnetic Resonance and its Application to Living Systems. Oxford University Press, NY.

36 Galloway GJ, J Field, SE Rose, LJ Haseler, WM Brooks, IM Brereton, PJ Bore, S Crozier, DM Doddrel (1989) In vivo High Resolution Volume Selected Proton Spectroscopy and T_1 Measurements in the Dog Brain. *Mag. Res. in Med.* **9**, 288-295.

37 Gey KF (1956) The Concentration of Glucose in Rat Tissues. *J. Biochem.* **64**, 145-150.

38 Gilbert KA, RA Kagan (eds) Radiation Damage to the Central Nervous System. Raven Press NY. (1980)

39 Giri PG, Kimler BF, Giri UP, Cox GG, Reddy EK (1985) Comparison of Single, Fractionated and Hyperfractionated Irradiation on the Developement of Normal Tissue Damage in Rat Lung. *Int. J. Radiation Oncology Biol. Phys.* **11**, 527-534.

40 Goldstein FB (1976) Amidohydrolases in Brain. *J Neurochem* **26**, 45-49.

41 Gorensten DG (1984) Phosphorous 31 NMR. Academic Press, NY.

42 Groothius DR, NA Vick (1980) Radionecrosis of the Central Nervous System in: Gilbert KA and RA Kagan (eds) Radiation Damage to the Central Nervous System. Raven Press, NY.129-143.

43 Grossman RI, CM Leavitt, SM Evans, RE Lenkinski, GA Holland, TJ Van Winkle, JT McGrath, WJ Curran, A Shetty, PM Joseph (1988) Experimental Radiation Injury. *Radiology.* **169**, 305-309.

44 Gwan Go K, TH Edzes (1975) Water in Brain Edema. *Arch. Neurol.* **32**, 462-465.

45 Haase A, C Malloy, GK Radda (1983) Spatial Localization of High Resolution ^{31}P Spectra with a Surface Coil. *J. Mag. Res.* **55**, 164-169.

46 Hall EJ (1973) Radiobiology for the Radiologist. Harper, NY.

47 Hecht-Leavitt C, RI Grossman, WJ Curran, JT McGrath, DN Biery, PM Joseph, DF Nelson (1987) MR of Brain Radiation Injury. *AJNR* **8**, 427-430.

48 Heindel W, J Bunke, W Steinbrich, G Friedman (1987) Human Brain Tumors. Abstract. *Proceeding from the 6th SMRM, New York.* p 153.

49 Henkelman RM, MJ Bronskill (1987) Artifacts in Magnetic Resonance Imaging in: Reviews of Magnetic Resonance in Medicine, volume 2. Pergammon press, Toronto. 1-126.

50 Hilberman M, V Harihara Subramanian, J Haselgrove, JB Cone, JW Egan, L Gyulai, B Chance (1984) *In vivo* Time Resolved Brain Phosphorus Nuclear Magnetic Resonance. *J. Cereb. Blood Flow Met.* **4**, 334-342.

51 Hilsted J, KE Jensen, C Thomsen, S Larsen, O Henricksen (1988) Maintenance of High Energy Brain Phosphorus Compounds during Insulin-induced Hypoglycemia in Men. *Diabetes* **37**, 760-762.

52 Hoffman WF, VA Levine, CB Wilson (1979) Evaluation of Malignant Glioma Patients During the Postirradiation Period. *J. Neurosurg.* **50**, 624-628.

53 Hope PL, EB Cady, A Chu, DT Delpy, RM Gardiner, EOR Reynolds (1987) Brain Metabolism and Intracellular pH During Ischemia and Hypoxia *J. Neurochem* **49**, 75-82.

54 Hopewell JW, JB Cavanagh (1972) Effects of X-Irradiation on the Mitotic Activity of the Subependymal Plate of Rats. *Br. J. of Radiology* **45**, 461-465.

55 Hubbard BM, JW Hopewell (1979) Changes in the Neuroglial Cell Populations of the Rat Spinal Cord after Local X-Irradiation. *Br. J. Radiology* . **52**, 816-821.

56 Hubesch B, D Sappey-Marinier, K Roth, DJ Meyerhoff, GB Matson, MW Weiner (1990) ^{31}P NMR Spectroscopy of Normal Brain and Brain Tumors. *Radiology*, in press.

57 Hyman RA, MF Loring, AL Liebeskind, JB Naidich, HL Stein (1978) CT Evaluation of Therapeutically Induced Changes in Primary and Secondary Brain Tumors. *Neuroradiology* **14**, 213-218.

58 Jenesen JAL, PR Luyten LC Meiners, PG Barth, FJ van Sprang, M Duran (1989) *In vivo* ^{1}H MRS in the Study of Basal Ganglia Pathology Associated with Inborn Errors of Metabolism. Abstract, *Proceedings from the 8th SMRM, Amsterdam.* p 373.

59 Kagan EH, RH Brownsen, DB Suter (1961) Radiation Caused Cytochemical Changes in Neurons. *Arch. Pathol.* **74**, 195-203.

60 Kingsley DPE, BE Kendall (1981) Review: CT of the Adverse Effects of Therapeutic Radiation on the CNS. *AJNR* **2**, 453-460.

61 Kirschner DA, VS Sapirstein (1982) Triethyl Tin Induced Myelin Oedema *J. Neurocytol.* **11**, 559-569.

62 Komatsumoto S, S Nioka, JH Greenberg, K Yoshizaki, VH Subramanian, B Chance, M Reivich (1987). Cerebral Energy Metabolism Measured *in vivo* by 31-P NMR in Middle Cerebral Artery Occlusion in the Cat. *J Cereb Blood Flow Met.* **7**, 557-562.

63 Koutcher JA, P Okunieff, L Neuringer, H Suit, T Brady (1987) Size Dependant Changes in Tumor Phosphate Metabolism after Radiation Therapy as Detected by ^{31}P Spectroscopy. *Int. J. Radiation Oncolgy Biol. Phys.* **13**, 1851-1855.

64 Kwee IL, T Nakada (1988) Phospholipid Profile of the Human Brain: ^{31}P NMR Spectroscopic Study. *Mag Res. in Med.* **6**, 296-299.

65 Lampert PW, MI Tom, WD Rider (1959) Delayed Effects of Radiation on the Human Central Nervous System: Early and Late Delayed Reactions. *Neurology* **14**, 912-917.

66 Luyten PR, JH Marien, B Sijtsma, JA den Hollander (1986) Solvent-Suppressed Spatially Resolved Spectroscopy. *J. Mag. Res.* **67**, 148-155.

67 Luyten PR, G Bruntink, A Heerschap, FM Sloff, JI van der Heijden, JA den Hollander (1988) Spectral Resolution: The Prime Dimension of Human ^{31}P Spectroscopy. Abstract , *Proceedings from the 7th SMRM, San Francisco.* p 708.

68 Malkin M, E Arbit, L Andersen, M Rosenblum, D Fass, J Galchich, S Leibel (1990). Treatment of Malignant Gliomas bt Stereotaxic Implantation of Removable, High-Activity Iodine-125 Sources. Abstract, *Proceedings from the 4th Canadian Neuro-Oncology Meeting, Winnipeg.*

69 Mansfield P, PG Morris (1982) NMR Imaging in Biomedicine: Advances in Magnetic Resonance. Academic Press, NY.

70 Martins AN, JS Johnston, JM Henry, TJ Stoffel, G Di Chiro (1977) Delayed Radiation Necrosis of the Brain. *J. Neurosurg* **47**, 336-345.

71 Masterson ME, R McGary, K Schmitt, JA Koutcher (1989) Accuracy and Reproducability of Image Derrived Relaxation Times on a 1.5 T Magnetic Resonance Scanner. *Med. Phys.* **16**, 225-233.

72 Matsumura H, ER Ross (1979) Delayed Cerebral Radionecrosis Following Treatment of Carcinoma of the Scalp. *Surg. Neurol.* **12**, 193-204.

73 McIlwain H, HS Bachelard (1985) Biochemistry and the Central Nervous System Churchill Livingstone, NY.

74 McMahon T, S Vahora (1986) Radiation Damage to the Brain: Neuropsychiatric Aspects. *General Hospital Psychiatry* **8**, 437-441.

75 Mikhael MA (1980) Dosimetric Considerations in the Diagnosis of Radiation Necrosis of the Brain. in: Gilbert HA, AR Kagan (eds) Radiation Damage to the Central Nervous System. Raven Press, NY

76 Moeller P, J Bergstrom, P Furst, K Hellstrom (1980) Effects of Ageing on Energy-Rich Phosphagens in Human Skeletal Muscles. *Clin. Sci.* **58**, 553-555.

77 Mueller P, B Wilson (1990) Photodynamic Therapy of Brain Tumors. Abstract, *Proceedings from the 4th Canadian Neuro-Oncology Meeting, Winnipeg.*

78 Mutsani M (1987) Radiation Therapy of Malignant Gliomas. Abstract. *Gan. To. Kagaku Ryoho.* **14**, 3219-3226

79 Naritomi H, M Sasaki, M Kanashiro, M Kitani, T Sawada (1988). Flow Thresholds for Cerebral Energy Disturbance. *J Cereb Blood Flow Metabolism* **8**, 16-23.

80 Naruse S, Y Horikawa, C Tanaka, K Hirakawa, H Nishikawa, K Yoshizaki (1982) Proton Nuclear Magnetic Resonance Studies on Brain Edema. *J. Neurosurg.* **56**, 747-752.

81 Nioka S, B Chance, M Hilberman, HV Subramanian, JS Leigh, RL Veech, RE Forster (1987) Relationship between Intracellular pH and Energy Metabolism in Dog Brain as Measured by ^{31}P NMR. *J of Applied Physiol.* **62**, 2094-2102.

82 Oberhaensli RD, PJ Bore, RP Rampling, D Hilton-Jones, LJ Hands, GK Radda (1986) Biochemical Investigations of Human Brain Tumors *in vivo* with ^{31}P Magnetic Resonance Spectroscopy. *Lancet* **1**, 8-11.

83 Okada S (1970) Radiation Biochemistry: the Nervous System. Chapt 7. Academic press, NY.

84 Ordridge RJ, A Connelly, JAB Lohman (1986) Image-Selected *in vivo* Spectroscopy (ISIS). *J. Mag. Res* **66**, 283-294.

85 Packer RJ, RA Zimmerman, LT Bilaniuk (1986) Magnetic Resonance Imaging in the Evaluation of Treatment Related Central Nervous System Damage. *Cancer* **58**, 635-640.

86 Peeling J, GR Sutherland, J.Girvin (1989) ^{1}H NMR Analysis of Metabolite Levels in Human Epileptic Brain Tissue and Brain Tumors. Abstract, *Proceedings from the 8th SMRM, Amsterdam.* p 296.

87 Pelech SL, DE Vance (1984) Regulation of Phosphatidylcholine Biosynthesis. *Biochimica et Biophysica Acta* **779**, 217-251.

88 Pettegrew JW, SL Klopp, J Dadok, NJ Minshew, T Glonek, MM Cohen (1986) Chemical Characterization of a Prominent Phosphomonoester Resonance from Mammalian Brain. *J. Mag. Res.* **67**, 443-450.

89 Pettegrew JW, SJ Klopp, NJ Minshew, T Glonek, JM Felisik, JP Tow, MM Cohen (1987) ^{31}P Nuclear Magnetic Resonance Studies of Phosphoglyceride Metabolism in Developing and Degenerating Brain. *J. Neuropathol. Exp. Neurol.* **46**, 419-430.

90 Petroff OAC, JW Prichard, KL Behar, JR Alger, JA den Hollander, RG Schulman (1985). Cerabral Intracellular pH by 31-P Nuclear Magnetic Resonance Spectroscopy. *Neurology* **35**, 781-788.

91 Petroff OAC, T Ogino, JR Alger (1988) High Resolution Proton Magnetic Resonance Spectoscopy of Rabbit Brain. *J. Neurochem.* **51**, 163-171.

92 Prichard JW, JR Alger, KL Behar, OAC Petroff, RG Shulman (1983) Cerebral Metabolic Studies *in vivo* by 31-P NMR. *Proc Natl Acad Sci USA*. **80**, 2748-2751.

93 Ra JB, SK Hilal, ZH Cho (1986) A Method for *in vivo* Imaging of the Short T_2 Component of Sodium-23. *Mag. Res. in Medicine* **3**, 296-302.

94 Rapin JR (1986) The Experimental Basis of Therapeutics in Ageing. *Gerontology* **32** (suppl. 1) 33-36.

95 Reichelt KL, F Fonnum (1969) Subcellular Localization of N-Acetyl-Aspartyl-Glutamate, N-Acetyl Glutamate and Glutathione in Brain. *J. Neurochem.* **16**, 1409-1416.

96 Richards T, TF Budinger (1988) NMR Imaging and Spectroscopy of the Mammalian Central Nervous System after Heavy Ion Radiation. *Rad. Res.* **113**, 79-101.

97 Rider WD (1963) Radition Damage to the Brain: a New Syndrome. *J Can. Assoc. Radiolology* **14**, 67-69.

98 Roberts JKM, N Wade-Jardetsky (1981) Intracellular pH Measurements by ^{31}P NMR. *Biochemistry* **20**, 3389-3394.

99 Rubin P, JN Whitaker, TL Ceckler, D nelson, PK Gregory, RB Baggs, LS Constine, PK Herman. Myelin Basic Protein and Magnetic Resonance Imaging for Diagnostic Radiation Myelopathy. *Int. J. Radiation Oncology Biol. Phys.* **15**, 1371-1381.

100 Satrustegui J, H Berkowitz, B Boden, E Donlen, A McLuaghlin, J Maris, R Warnell, B Chance (1988) An *in vivo* Phosphorus NMR Study of Variations with Age in the Phosphodiester Content in Human Muscle. *Mechanisms of Aging and Developement* **42** 105-114.

101 Schwarcz R, R Zaczek, JT Coyle (1978) Microinjection of Kainic Acid into the Rat Hippocampus. *Eur. J. Physiol.* **50**, 209-220.

102 Sheline GE (1980) Irradiation Injury of the Human Brain. in: Gilbert KA and RA Kagan (eds) Radiation Damage to the Nervous System. Raven press NY.

103 Sheline GE, WM Wara, V Smith (1980) Therapeutic Irradiation and Brain Injury. *Int. J. Radiation Oncology Biol. Phys.* **6**, 1215-1228

104 Shoubridge EA, DL Arnold, JF Emrich, J Villemure, W Feindel (1988) Phosphorus MR Spectroscopy and Characterization of Astrocytomas, Meningiomas and Pituitary Adenomas. Abstract, *Proceedings from the 7th SMRM , San Francisco.* p 616.

105 Smith MA, D Porter, M Lowry, VT Ayton, MA Richards, CJ Twelves, P Garlick, MN Maisey (1988) Precision and Normal Variations of Volume Selected *in vivo* Spectroscopy. Abstract. *Proceedings from the 7th SMRM , San Francisco.* p 343.

106 Smith ME, JA Benjamins (1984) Model Systems for Study of Perturbations of Myelin Metabolism. in: P Morell (ed) Myelin. Plenum Press, NY

107 Behar KL, DL Rothman, SM Fitzpatrick, HP Hetherington, RG Shulman (1987) Combined ^{1}H and ^{31}P NMR Studies of Rat Brain *in vivo. Annals NY Academy of Sciences.* , 81-88.

108 Taylor DJ, M Crowe PJ Bore, P Styles, DL Arnold, GK Radda (1984) Examination of the Energetics of Ageing Skeletal Muscle using Nuclear Magnetic Resonance. *Gerontology* **30**, 2-7.

109 Thomas MA, J Kurhanewicz, P Jajodia, G Karczmar, B Hubesch, GB Matson TL James, P Narayan, MW Weiner (1989) ^{31}P NMR Spectroscopy of Human Prostate *in vivo.* Abstract, *Proceedings from the 8th SMRM, Amsterdam.* p 297

110 Tiller-Borcich JK, JR Fike, TL Phillips, RL Davis (1987) Pathology of Delayed Radiation Brain Damage. *Radiation Research* **110**, 161-172.

111 Tsuruda JS, KE Kortman, WG Bradley, DC Wheeler, WV Dalsem, TP Bradley. (1987) Radiation Effects on Cerebral White Matter. *AJN* **149**, 165-171.

112 Van der Kogel AJ (1980) Mechanisms of Late Radiation Injury in the Spinal Cord in: Meyn RE, HR Withers (eds) Radiation Biology in Cancer Research Raven Press, NY. 461-471.

113 Van der Kogel AJ, HA Sissingh, J Zoetlelief (1982) Effect of Xrays and Neutrons on Rat Spinal Cord. *Int. J. Radiation Oncology Biol. Phys.* **8**, 2095-2097.

114 Van der Kogel AJ (1986) Radiation Induced Damage in the Central Nervous System *Br. J. of Cancer* **53**, supp VII, 207-217.

115 Van der Kogel AJ (1977) Radiation Tolerance to Rat Spinal Cord. *Radiology* **122**, 505- 509.

116 Van der Schuern E, W Landuyt, KK Ang, AJ Van der Kogel (1988) From 2 Gy to 1 Gy per Fraction: Sparing Effect in Rat Spinal Cord. *Int. J. Radiation Oncology Biol. Phys.* **14**, 297-300.

117 Vink R, MK McIntosh, MW Weiner, AI Faden (1987) Effects of Traumatic Brain Injury on Cerebral High-Energy Phosphates and pH. *J Cereb. Blood Flow Metab.* **7**, 563-571.

118 Wheeler KT, RE Weinstein (1979) Accumulation of Neuronal DNA Damage as an Early Covariate or Determinant of Death after Whole Brain Irradiation. *Radiation Research* **80**, 343-347.

119 Yang X, JL Darling, TJ McMillan, JH Peacock, GG Steel. (1989) The Cellular Radiobiology of Human Malignant Glioma. Abstract, *Proceedings of the 15th LH Gray Conference, Canterbury.* p 8.

120 Johnson G, I Ormerod, D Barnes, PS Tofts, D Phil, D MacManus (1987) Accuracy and Precision in the Measurement of Relaxation Times from Nuclear Magnetic Resonance Images. *Br. J. Radiology*, **60**, 143-153.

121 Bruhn H, J Frahm, ML Gyngell, KD Merboldt, W Hanicke, R Sauter, C Hamburger (1989) Noninvasive Differentiation of Tumors with Use of Localized H-1 MR Spectroscopy *in vivo*. *Radiology*, **172**, 541-548.

APPENDIX I:
COMPUTER PROGRAM TO AID IN THE DETERMINATION OF THE SCALING FACTOR OF T_2 CALCULATED IMAGES ON THE PHILIPS GYROSCAN

```
C       Program SCALE.FOR
C
C       Written by Ravi Menon
C       last  edited  20/01/88
C
C
                INTEGER*2 SCALE1,SCALE2,SCALE(256)
                INTEGER IBLOCK,LINE,PIXEL
                CHARACTER*60 FNAMEOUT
C
100             FORMAT(A)
102             FORMAT('&INPUT DATA FILE')
103             FORMAT(I10,I10,I10,I10)
C
                WRITE  (6,102)
                READ(5,100) FNAMEOUT
C
      OPEN(UNIT=1, FILE=FNAMEOUT, STATUS='NEW', FORM='UNFORMATTED',
     + RECORDTYPE='FIXED', RECL=128)
          DO 500 IBLOCK=1,9
            DO 200 LINE=1.128
              DO 120 PIXEL=1,256
120             SCALE(PIXEL)=SCALE1
                WRITE(1)  (SCALE(I),I=1,256,1)
                WRITE(6,103) SCALE1,IBLOCK,LINE,PIXEL
200             CONTINUE
C
                DO 400 LINE=129,256
                  DO 300 PIXEL=1,256
300                 SCALE(PIXEL)=SCALE2
                      WRITE(1) (SCALE(I),I=1,256,1)
400                 CONTINUE
                     WRITE(6,103) SCALE2,IBLOCK,LINE,PIXEL
500             CONTINUE
                END
```

APPENDIX II:
MEDICATIONS RECEIVED BY THE BRAIN TUMOR PATIENTS

	NMR SESSION					
patient	pre RT	post RT	2 month	4 month	8 month	12 month
1	Dc Dp	Dc Dp	Dp	Dp	Dp	Dc Z
2	Dc Dl	Dc Dl	Dl	Dl	--------	--------
3	Dc Dl	Dc Dl	Dc Dl	Dl	Dl	--------
4	Dc Dl Z	Dc Dl Mx Z	Dc Dl Z	Dl Z	Dl	Dl
5	none	Dc Tt	Tt	Tt	Dc	Dc
6	Sl Tl	Dl	Dl	Dl Tl	--------	--------
7	Dl	Tl	Tl	Tl	Tl	Tl
8	Dc Dl Z	Dc Dl Z	none	none	none	none
9	Dc Dl	Dc Z	Dc Z	Dc Z	--------	--------
10	Dc Dl Tt	Dc Dl Z	Dc Dl Z	Dc Dl Z	--------	--------
11	Dc,Z	Dc,Z	--------	--------	--------	--------
12	Dc Tl Tt	Dc Tl Tt	Dc Tl Tt	--------	--------	--------
13	none	none	Dc	--------	--------	--------
14	Dc Dl	Dc Dl	Dc Dl	Dc Dl	Dl	Dl
15	Ct	--------	--------	Ct	Ct	
16	Dl	Dl	Dl	Dl	Dl	
17	none	none	--------	--------	--------	--------
18	Dc Tl	Dc Tl	--------	Tl		
19	Ct Pr	Ct Pr	Ct Pr			
20	Dc Tl	Dc Tl	Dc Dl Tl			
21	Dc Dl Tt	Dc Dl	Dl			
22	none	none				
23	Dc Dl Z	Dc Dl Z				

The medications listed are as follows:

Ct = cortisone, Dc = decadron (anti inflammatory steroids)

Dl = dilantin, Tl = tegretol, Dp = depakene (anticonvulsants)

Mx = maxeran, Tt = tagamet, Z = zantac (stomach settlers)

Pr = parledol (growth hormone inhibitor)

APPENDIX III:
MEDICAL INFORMATION ABOUT THE BRAIN TUMOR PATIENTS

patient	Age of patient	Tumor Type	Total Dose/ Treatment	Recurrence Date	Other Information
1	29	GB III	8000/HYP	10 mo post	
2	54	GB III	6000/IUDR	6 mo post	
3	36	GB IV	8000/HYP	8 mo post	
4	39	GB III	6000/IUDR	5 mo post	
5	30	GB III	8000/HYP	10 mo post	
6	35	AST II	5500 /CONV	8 mo post	
7	36	GB III	6000/IUDR	none	
8	48	GB IV	6000/IUDR	none	
9	22	GB IV	6000/IUDR	9 mo post	2nd operation 8 mo post RT
10	37	GB IV	6000/IUDR	7 mo post	
11	29	GB IV	8000/HYP	5 mo post	2nd operation 6 mo post RT
12	51	GB III	8000/HYP	during RT	Tumor did not respond to RT
13	25	STM III	8000/HYP	4 mo post	Surgery = shunt insertion
14	27	GB IV	8000/HYP	11 mo post	
15	39	PIT	5000 /CONV	1 mo post	
16	43	OLG II	5000 /CONV	none	
17	55	AST II	5000 /CONV	none	Surgery = needle biopsy
18	32	OLG II	5500 /CONV	none	
19	39	PIT	4500 /CONV	none	RT began 7 mo post surgery
20	55	GB IV	6000/IUDR	none	Surgery = needle biopsy
21	24	AST II	5000 /CONV	none	
22	55	PIT	5000 /CONV	none	
23	34	GB III	6000/IUDR	none	

The tumors listed are as follows:
GB = glioblastoma multiforme, AST = astrocytoma, PIT = pituitary adenoma, STM = brainstem astrocytoma, OLG = oligodendroglioma.
The numbers listed after the symbols refer to the grade of the tumor.
Symbols describing radiation treatments include:
HYP = hyperfractionation, IUDR = iododeoxyuridine, CONV = conventional
All patients underwent full surgery for subtotal removal of their tumor, unless otherwise stated.
The age of the patient refers to the age at the time of radiotherapy
All patients began RT 2-4 weeks post surgery, unmess otherwise stated.

APPENDIX IVa:
PHOSPHORUS NMR DATA FROM THE CNS OF HEALTHY VOLUNTEERS:
NORMAL VARIATIONS IN pH AND METABOLITE PEAK AREA RATIOS

Volunteer	region of brain	PME / ATP	Pi / ATP	PDE / ATP	PCr / ATP	pH
B Mc	L.Temporal	.346	.443	1.16	.788	7.15
I H	L.Temporal	.377	.466	1.28	.744	7.04
P B	L.Temporal	.407	.576	1.26	.822	7.14
P B	R.Temporal	.401	.651	1.18	.762	7.08
K D	L.Temporal	.334	.530	1.12	.864	7.12
S R	R.Temporal	.262	.411	.930	.628	7.11
S R	L.Temporal	.271	.285	.989	.515	7.21
K D	R.Temporal	.261	.385	.703	.729	7.14
K D	L.Temporal	.250	.387	.713	.693	7.18
K D	R.Temporal	.215	.440	.709	.782	7.12
S R	R.Temporal	.252	.412	.925	.744	7.08
S R	L.Temporal	.337	.359	1.08	.540	7.09
S R	R.Temporal	.290	.312	.988	.672	7.12
S R	L.Temporal	.289	.404	.998	.725	7.10
S R	R.Temporal	.279	.520	1.03	.794	7.18
S R	L.Temporal	.236	.393	.855	.659	7.16
K D	R.Frontal	.291	.455	.872	.723	7.08
K D	L.Occipital	.217	.439	1.00	.507	7.21
K D	L.Frontal	.363	.640	1.10	.669	7.14
K D	R.Occipital	.350	.430	1.10	.624	7.18
P S	L.Temporal	.396	.418	1.42	.736	7.06
M L	L.Temporal	.314	.521	1.23	.657	7.11
M L	R.Temporal	.344	.424	1.22	.849	7.05
L T	L.Temporal	.299	.365	1.23	.765	7.14
S R	R.Frontal	.420	.522	1.35	.747	7.13
S R	L.Frontal	.367	.336	1.19	.608	7.06
K D	L.Temporal	.277	.368	1.05	.670	7.12
K D	R.Temporal	.330	.360	1.13	.742	7.08

The various volunteers are identified by their initials. The regions of brain listed indicate the areas of the cerebral hemispheres from which the NMR data was obtained. R = right hemisphere, L = left hemisphere. A volume of approximately 25 cm^2 was interrogated for each spectrum. Table 3.00 summarizes the raw data listed above.

APPENDIX IVb:
pH VALUES FROM BRAIN RECIEVING HIGH RADIATION DOSES

	NMR Spectroscopy Sesson					
patient number	Pre RT	Post RT	2 month	4 month	8 month	1 year
1	7.10	7.15	-----	-----	-----	-----
2	7.14	7.08	7.07	-----	-----	-----
3	7.18	-----	7.08	-----	-----	-----
4	7.11	7.14	7.18	7.12	7.11	7.13
5	7.23	7.14	7.14	7.20	7.17	7.15
6	7.13	7.10	7.04	-----	-----	-----
7	7.11	-----	7.15	7.09	-----	7.17
8	7.25	7.15	7.18	7.18	7.15	7.09
9	7.21	7.12	7.15	7.15	-----	-----
10	7.11	7.07	7.07	7.06	-----	-----
11	7.21	7.23	7.23	-----	7.08	7.21
12	7.11	7.14	7.12	-----	-----	-----
13	-----	-----	7.11	7.07	7.18	-----

APPENDIX IVc:
pH VALUES FROM BRAIN RECIEVING LOW RADIATION DOSES

patient number	NMR Spectroscopy Session					
	Pre RT	Post RT	2 month	4 month	8 month	1 year
1	7.06	7.13	-----	-----	-----	-----
2	7.05	7.07	7.09	-----	-----	-----
3	7.04	-----	7.12	-----	-----	-----
4	7.09	7.12	7.09	7.08	7.08	?
5	7.08	7.08	7.07	7.09	7.10	7.14
6	7.08	7.09	7.06	-----	-----	-----
7	7.08	-----	-----	7.07	-----	7.11
8	7.14	7.11	7.14	7.09	7.11	-----
9	7.14	7.16	7.14	-----	-----	-----
10	7.08	7.08	7.13	7.12	-----	-----
11	-----	-----	-----	-----	7.15	7.09
12	7.13	7.17	-----	-----	-----	-----
13	-----	-----	-----	-----	7.09	-----

APPENDIX IVd: PHOSPHORUS NMR DATA FROM IRRADIATED BRAINS

NMR peaks	region of brain	NMR spectroscopy session					
		Pre RT	Post RT	2 mo post	4 mo post	8 mo post	12 mo post
PME / ATP	high dose	.324 ±.06	.301 ±.06	.319 ±.09	.293 ±.05	.311 ±.07	.313 ±.05
	low dose	.301 ±.05	.291 ±.06	.327 ±.07	.354 ±.05	.314 ±.04	.336 ±.03
Pi / ATP	high dose	.445 ±.13	.488 ±.13	.446 ±.10	.486 ±07	.392 ±.06	.470 ±.03
	low dose	.484 ±.08	.439 ±.08	.404 ±.08	.466 ±.07	.466 ±.07	.413 ±.05
PDE / ATP	high dose	1.17 ±.06	1.07 ±.15	1.03 ±.22	1.13 ±.10	1.18 ±.10	1.14 ±.03
	low dose	1.17 ±.22	1.08 ±.23	1.09 ±.21	1.13 ±.18	1.17±.10	1.09 ±.13
PCr / ATP	high dose	.779 ±.08	.760 ±.21	.798 ±.09	.793 ±.18	.732 ±.05	.808 ±.06
	low dose	.818 ±.07	.738 ±.18	.804 ±.06	.739 ±.17	.775 ±.03	.760 ±.07
pH	high dose	7.16 ±.05	7.13 ±.04	7.13 ±.06	7.12 ±.05	7.14 ±.04	7.15 ±.05
	low dose	7.09 ±.03	7.11 ±.04	7.11 ±.03	7.09 ±.02	7.11 ±.03	7.10 ±.04

Data are listed as mean values ± standard deviations. High dose regions of brain were exposed to 50-100% of the total radiotherapy dose, while low dose regions received less than 50% of the total dose. In most cases, these two regions corresponded to anatomically similar areas on opposite cerebral hemispheres. Data from this table are graphed in Figure 3.02.

APPENDIX Va:
PROTON NMR DATA FROM THE CNS OF HEALTHY VOLUNTEERS: NORMAL VARIATIONS IN METABOLITE PEAK AREA RATIOS

Volunteer	region of brain	NAA / Cho	NAA / Cr	Cr / Cho	NAA / H_2O	Cho / H_2O	Cr / H_2O
KD	R.Occipital	2.23	1.81	1.23			
PC	L.Temporal	2.13	2.03	1.06			
PC	R.Occiptal	2.07	2.64	0.78			
SP	R.Temporal	2.27	2.53	0.90			
SP	L.Temporal	1.73	1.98	0.87			
BD	R.Temporal	2.18	1.77	1.24	.885*	.405*	.501*
BD	L.Temporal	2.79	2.55	1.09			
RM	L.Occipital	2.57	2.50	1.03			
RM	R.Temporal	2.63	1.71	1.54	.776*	.295*	.453*
DW	L.Occipital	1.76	1.79	0.98			
DW	R.Occipital	1.83	2.32	0.79			
DS	L.Temporal	2.29	2.51	0.91			
SL	R.Occipital	2.64	1.82	1.45	.789*	.297*	.432*
SL	R.Temporal	1.93	1.69	1.15	.697*	.360*	.413*
FF	L.Temporal	1.82	1.85	0.98			
OK	L.Temporal	1.85	1.44	1.29	.732*	.396*	.509*
FS	R.Temporal	2.82	2.74	1.03			
GS	R.Occipital	1.95	2.14	0.91			
MH	R.Temporal	3.13	2.05	1.52			

The various volunteers are identified by their initials. Regions of brain listed indicate the areas of the cerebral hemispheres from which the NMR data was obtained. R = right hemisphere, L = left hemisphere. The values marked with an asterisk (*) are multiplied by 10^{-2}. Mean values ± SD can be found in Table 3.09.

APPENDIX Vb:
Cr/Cho PEAK AREA RATIOS FROM THE CNS OF PATIENTS

patient	region of brain	Pre RT	Post RT	2 mo	4 mo	8 mo	12 mo
14	high dose	-----	-----	-----	-----	-----	**.911**
	low dose (Dc)	-----	-----	-----	-----	-----	**1.32**
15	high dose	-----	-----	-----	1.35	**2.83**	
	low dose	-----	-----	-----	1.25	**1.14**	
16	high dose	-----	-----	-----	.733	**1.95**	
	low dose	-----	-----	-----	-----	**.730**	
17	high dose	-----	.959	-----	-----		
	low dose	-----	.985	-----	-----		
18	high dose	-----	1.70	-----	**1.03**		
	low dose (Dc)	-----	1.07	-----	**1.49**		
19	high dose	-----	-----	.898			
	low dose	-----	-----	.798			
20	high dose	2.06	2.08	**1.09**			
	low dose (Dc)	1.50	1.29	**1.65**			
21	high dose	.922	1.11	**1.67**			
	low dose (Dc)	-----	1.31	**1.38**			
22	high dose	1.58	**.470**				
	low dose	1.96	**1.12**				
23	high dose	1.33	1.72				
	low dose (Dc)	1.21	1.59				

The values listed in the shaded areas are complemented by data using water as the reference peak. Water standards data can be found in Table 3.12. A (Dc) symbol indicates that the patient was receiving Decadron during their radiation treatment. Figure 3.08 graphs the data tabulated above.

APPENDIX Vc:
NAA/Cho PEAK AREA RATIOS FROM THE CNS OF PATIENTS

patient	region of brain	Pre RT	Post RT	2 mo	4 mo	8 mo	12 mo
14	high dose	-----	-----	-----	-----	-----	**1.71**
	low dose (Dc)	-----	-----	-----	-----	-----	**2.41**
15	high dose	-----	-----	-----	1.06	**1.44**	
	low dose	-----	-----	-----	2.01	**2.92**	
16	high dose	-----	-----	-----	1.02	**3.02**	
	low dose	-----	-----	-----	-----	**1.85**	
17	high dose	-----	1.52	-----	-----		
	low dose	-----	1.86	-----	-----		
18	high dose	-----	1.96	-----	**1.89**		
	low dose (Dc)	-----	2.28	-----	**2.62**		
19	high dose	-----	-----	1.30			
	low dose	-----	-----	1.50			
20	high dose	2.42	2.91	**1.81**			
	low dose (Dc)	2.31	2.36	**1.90**			
21	high dose	1.75	2.06	**2.47**			
	low dose (Dc)	-----	2.39	**2.17**			
22	high dose	1.68	**0.76**				
	low dose	2.80	**2.11**				
23	high dose	2.87	3.06				
	low dose (Dc)	1.82	2.88				

The values listed in the shaded areas are complemented by data using water as the reference peak. Water standards data can be found in Table 3.12. A (Dc) symbol indicates that the patient was receiving Decadron during their radiation treatment. Figure 3.08 graphs the data tabulated above.

APPENDIX Vd:
NAA/Cr PEAK AREA RATIOS FROM THE CNS OF PATIENTS

patient	region of brain	Pre RT	Post RT	2 mo	4 mo	8 mo	12 mo
14	high dose	-----	-----	-----	-----	-----	**1.88**
	low dose (Dc)	-----	-----	-----	-----	-----	**1.83**
15	high dose	-----	-----	-----	0.78	**0.51**	
	low dose	-----	-----	-----	1.60	**2.56**	
16	high dose	-----	-----	-----	1.40	**1.55**	
	low dose	-----	-----	-----	-----	**2.55**	
17	high dose	-----	1.59	-----	-----		
	low dose	-----	1.88	-----	-----		
18	high dose	-----	1.14	-----	**1.82**		
	low dose (Dc)	-----	2.14	-----	**1.75**		
19	high dose	-----	-----	1.44			
	low dose	-----	-----	1.88			
20	high dose	1.17	1.40	**1.60**			
	low dose (Dc)	1.54	1.82	**1.15**			
21	high dose	1.90	1.85	**1.48**			
	low dose (Dc)	-----	1.83	**1.57**			
22	high dose	1.06	**1.61**				
	low dose	1.43	**1.89**				
23	high dose	2.16	1.78				
	low dose (Dc)	1.51	1.81				

The values listed in the shaded areas are complemented by data using water as the reference peak. Water standards data can be found in Table 3.12. A (Dc) symbol indicates that the patient was receiving Decadron during their radiation treatment. Figure 3.08 graphs the data tabulated above.